SECTION II. TASK 2. SUBMODEL DEVELOPMENT AND EVALUATION

Objectives

The objectives of this task are to develop or adapt advanced physics and chemistry submodels for the reactions of coal in an entrained-bed and a fixed-bed reactor and to validate the submodels by comparison with laboratory scale experiments.

Task Outline

The development of advanced submodels for the entrained-bed and fixed-bed reactor models will be organized into the following categories: a) Coal Chemistry (including coal pyrolysis chemistry, char formation, particle mass transfer, particle thermal properties, and particle physical behavior); b) Char Reaction Chemistry at high pressure; c) Secondary Reactions of Pyrolysis Products (including gas-phase cracking, soot formation, ignition, char burnout, sulfur capture, and tar/gas reactions); d) Ash Physics and Chemistry (including mineral characterization, evolution of volatile, molten and dry particle components, and ash fusion behavior); e) Large Coal Particle Effects (including temperature, composition, and pressure gradients and secondary reactions within the particle, and the physical affects of melting, agglomeration, bubble formation and bubble transport; f) Large Char Particle Effects (including oxidation); g) SO_x-NO_x Submodel Development (including the evolution and oxidation of sulfur and nitrogen species); and h) SO_x and NO_x Model Evaluation.

II.A. SUBTASK 2.a. - COAL TO CHAR CHEMISTRY SUBMODEL DEVELOPMENT AND EVALUATION

Senior Investigator - David G. Hamblen
Advanced Fuel Research, Inc.
87 Church Street, East Hartford, CT 06108
(203) 528-9806

Objective

The objective of this subtask is to develop and evaluate, by comparison with laboratory experiments, an integrated and compatible submodel to describe the organic chemistry and physical changes occurring during the transformation from coal to char in coal conversion processes. Many of the data and some computer codes for this submodel are available, so it is expected that a complete integrated code will be developed during Phase I. Improvements in accuracy and efficiency will be pursued during Phase II.

Accomplishments

Characterization by FT-IR, TGA and pyrolysis experiments were carried out on most of the Argonne coal samples, both in bulk and in the glass ampoules. A Rosebud subbituminous coal was also characterized. A study was initiated on the effects of minerals on reactivity by demineralization of the samples using acid treatments. Samples in which alkali metals were removed by ion-exchange methods also being investigated. Work was done on mass transfer effects in consultation with E.M. Suuberg. The literature search on transport properties during pyrolysis was completed and presented inthe Second Quarterly Report. To model pyrolysis data for low heating rate experiments, the internal mass transfer resistance to tar escape must be included. A simple model of tar transport was developed and successfully tested. The FG and DVC models are being modified so that the chemistry of the bridge breaking and crosslinking in the DVC model is completely consistent with the chemistry of gas formation in the FG model. The combined FG/DVC model has been installed on a Sun workstation and programming has been initiated to graphically present the output data. Work was initiated on computing the optical properties of particles during the coal to char transformations.

Coal Characterization

Characterization of the coal samples for this program was performed by quantitative FT-IR analysis, pyrolysis, and char reactivity. Analyses were run on ampoules of Argonne samples 1-7 and 9, listed in Tables II.A-1 and II.A-2. Also six jars containing bulk samples of coal were received from the Argonne National Laboratory for coals 1,2,4-7. Due to the broad particle distribution, each jar was well mixed and a small representative sample was removed, handground and sieved to obtain the 200 x 325 mesh fractions. Additional samples of these six coals were obtained from BYU after grinding. For Rosebud subbituminous coal, samples have been obtained from METC. Bulk samples of the Beulah lignite were obtained from UNDERC. Bulk samples of Illinois #6 have been ordered from the Illinois State Geological Survey. Measurements have been made on raw coals and coals demineralized in HCl and HF.

Quantitative FT-IR Analysis

The coal samples were subjected to FT-IR analysis using approximately 1 mg of dry ground sample in approximately 300 mg of alkali halide. To obtain optical properties for the coals, CsI pellets were prepared in addition to the KBr pellets. Figures II.A-1a and 1b - II.A-9a and 9b show the dry uncorrected KBr and CsI pellet spectra for the nine coals. Seven of the spectra are for bulk samples and two are for ampoule samples. In general, the bulk and ampoule samples are quite similar as shown in Figs. II.A-10 to II.A-16. The exception is the Upper Knawha which has a much higher mineral concentration in the bulk sample.

To obtain quantitative functional group and mineral matter data, a spectral synthesis routine was applied to the dry mineral matter and baseline corrected spectra (see Figs. II.A-1c -II.A-9c). The organic functional group data are shown in Tables II.A-3 and II.A-4 for bulk and ampoule samples, respectively. Tables II.A-5 and II.A-6 list the mineral matter data for the bulk and ampoule samples, respectively. The two sets of samples are similar except for the Upper Freeport and Pittsburgh No. 8 where the bulk samples are poorer in hydrogen and the Upper Knawha in which the bulk sample has a higher clay and quartz content.

Pyrolysis in Thermogravimetric Analyzer (TGA)

Pyrolysis experiments on the ampoule and bulk samples were performed using the TGA. With a N_2 flow of 400 cc/min and a N_2 purge flow of 40 cc/min, the coal particle temperatures reached 900°C with heating rates of 30°C/min. Plots of the TGA pyrolysis runs are shown in Figs. II.A-17 - II.A-21. The bulk samples and ampoules are similar except for some differences in moisture and mineral content

Table II.A.1.

AFR/BYU Program Coal Samples

Coal Name	Rank	Mine/Location	Source
1. Upper Freeport	Medium Volatile Bituminous	Pennsylvania	ANL
2. Wyodak	Subbituminous	Wyoming	ANL
3. Illinois #6	High Volatile Bituminous	Macoupin, Illinois	ANL
4. Pittsburgh #8	High Volatile Bituminous	Washington, Penn.	ANL
5. Pocahontas #3	Low Volatile Bituminous	Virginia	ANL
6. Utah Blind Canyon	High Volatile Bituminous	Utah	ANL
7. Upper Knawha	Medium Volatile Bituminous	Eastern, WV	ANL
9. Zap	Lignite	Mercer, N. Dakota	UND
10. Rosebud	Subbituminous	Montana	METC

TABLE II.A-2

ELEMENTAL COMPOSITION (MAF)

COAL NAME	C	H	O	S*	ASH*
1. Upper Freeport (UF)	87	5.5	4	2.8	13
2. Wyodak (WY)	74	5.1	19	0.5	8
3. Illinois #6 (Ill. #6)	77	5.7	10	5.4	16
4. Pittsburgh #8 (Pitt #8)	83	5.8	8	1.6	9
5. Pocahontas #3 (Poc #3)	91	4.7	3	0.9	5
6. Utah Blind Canyon (UT)	79	6.0	13	0.5	5
7. Upper Knawha (WV)	81	5.5	11	0.6	20
9. North Dakota (Zap)	73	5.3	21	0.8	6
10. Rosebud	72.1	4.7	20.3	1.2	10

* Dry Basis

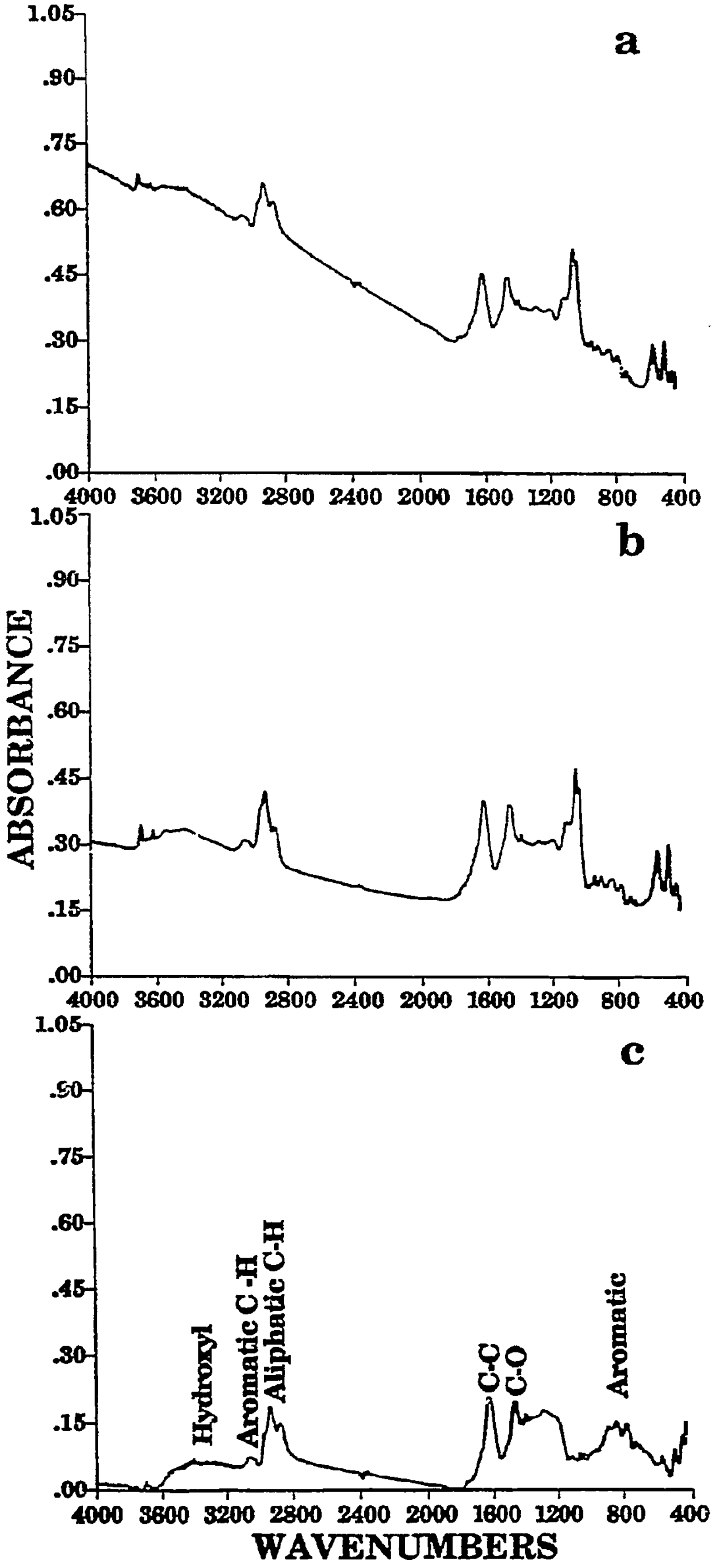

Figure II.A-1. FT-IR Spectra of Bulk Upper Freeport Bituminous Coal. a) KBr, b) CSI, and c) KBr Pellet, Mineral Matter Corrected.

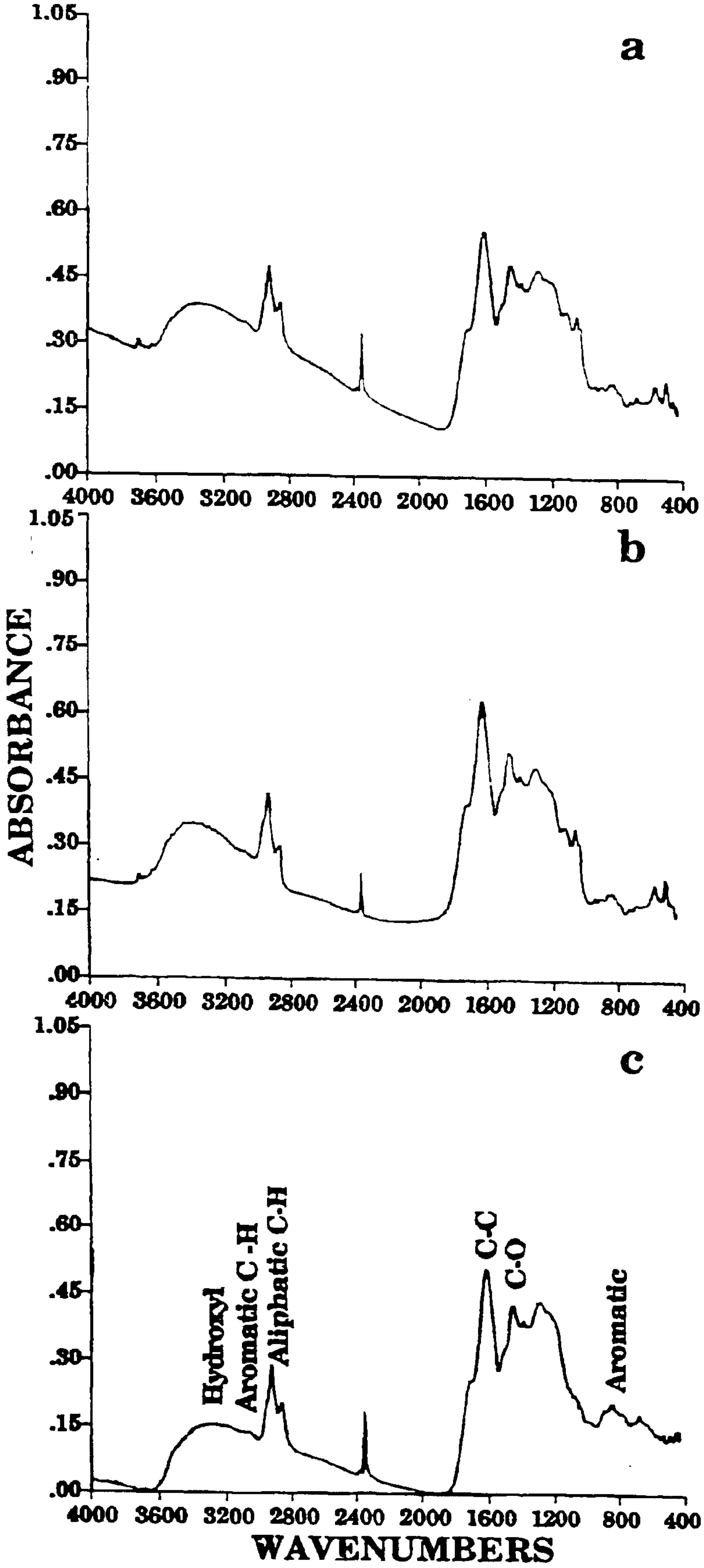

Figure II.A-2. FT-IR Spectra of Bulk Wyodak Subbituminous Coal. a) KBr, b) CSI, and c) KBr Pellet, Mineral Matter Corrected.

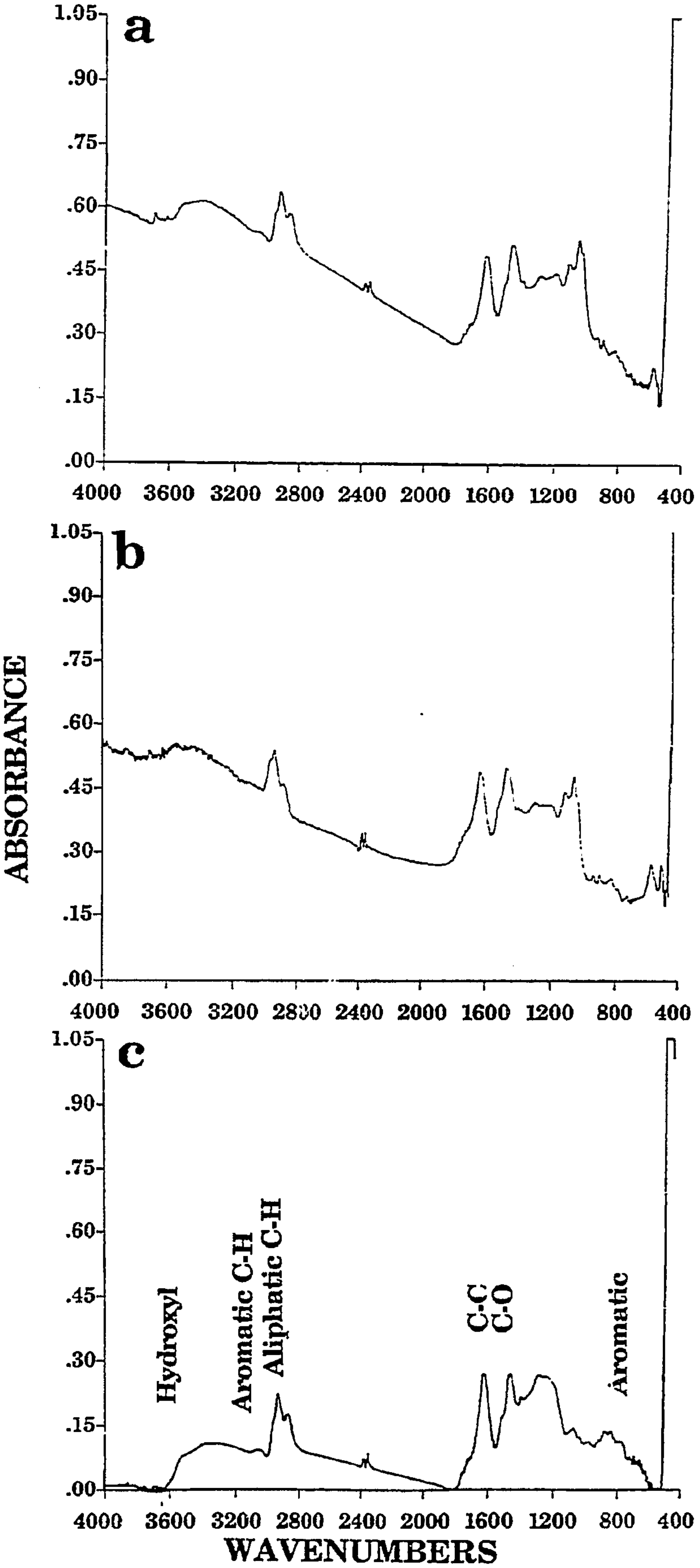

Figure II.A-3. FT-IR Spectra of Bulk Illinois #6 Bituminous Coal. a) KBr, b) CSI, and c) KBr Pellet, Mineral Matter Corrected.

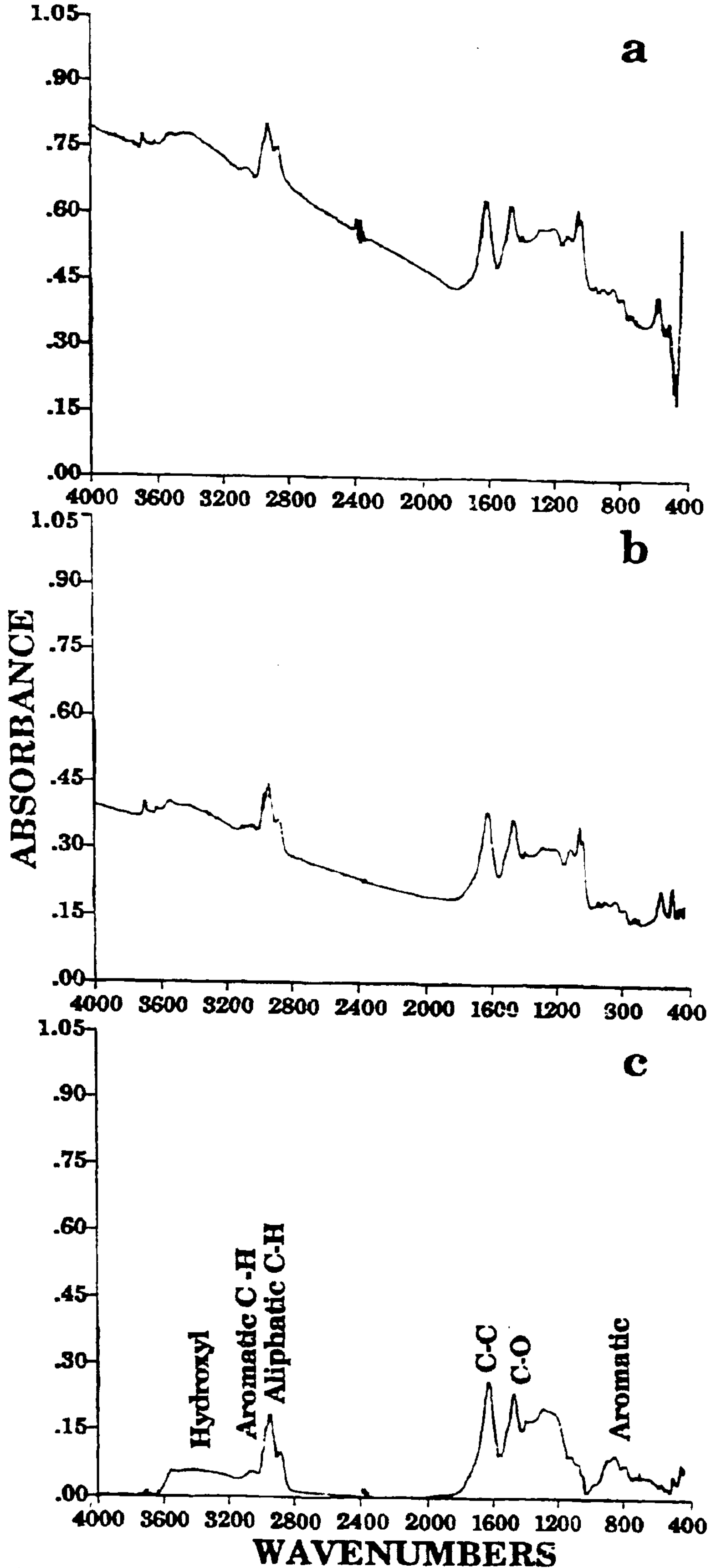

Figure II.A-4. FT-IR Spectra of Bulk Pittsburgh Seam Bituminous Coal. a) KBr, b) CSI, and c) KBr Pellet, Mineral Matter Corrected.

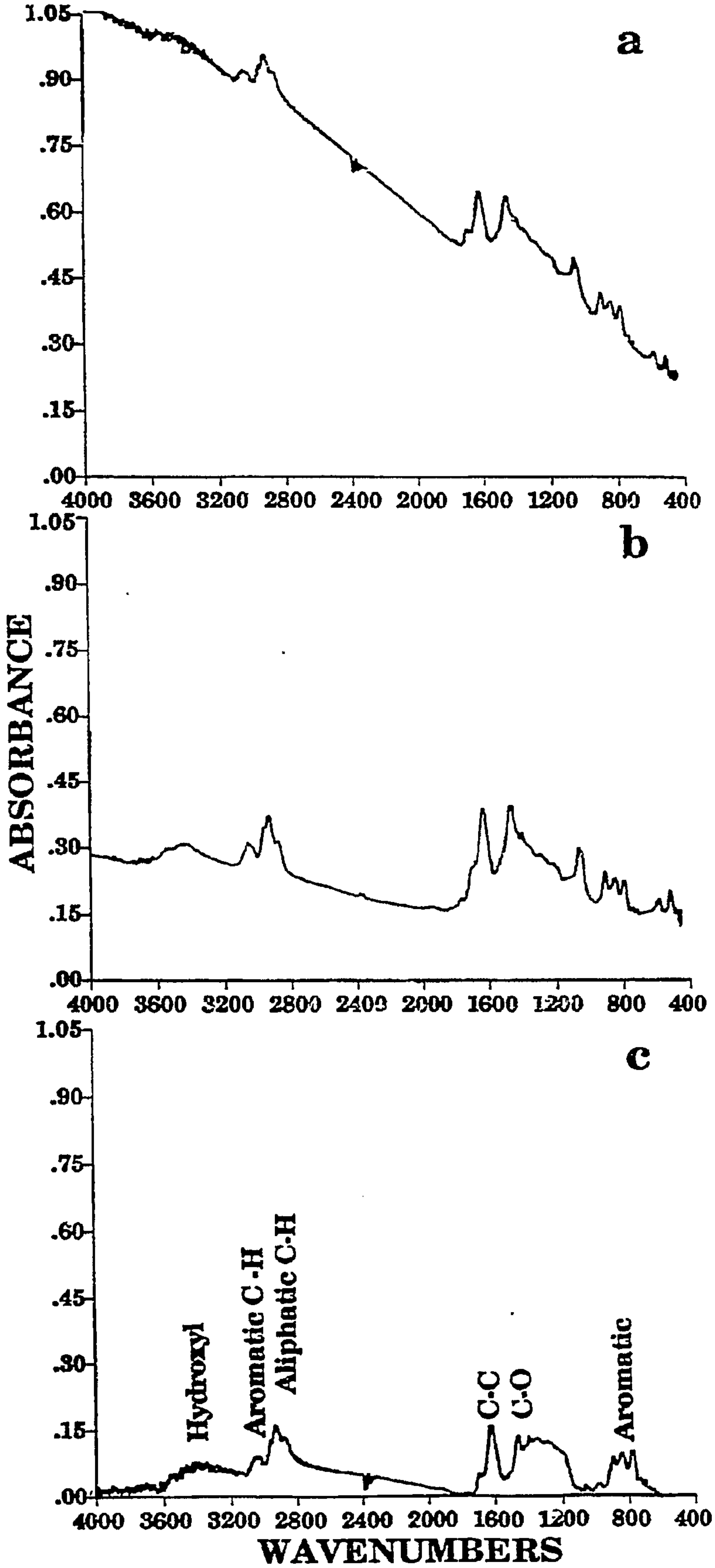

Figure II.A-5. FT-IR Spectra of Bulk Pocahontas Bituminous Coal. a) KBr, b) CSI, and c) KBr Pellet, Mineral Matter Corrected.

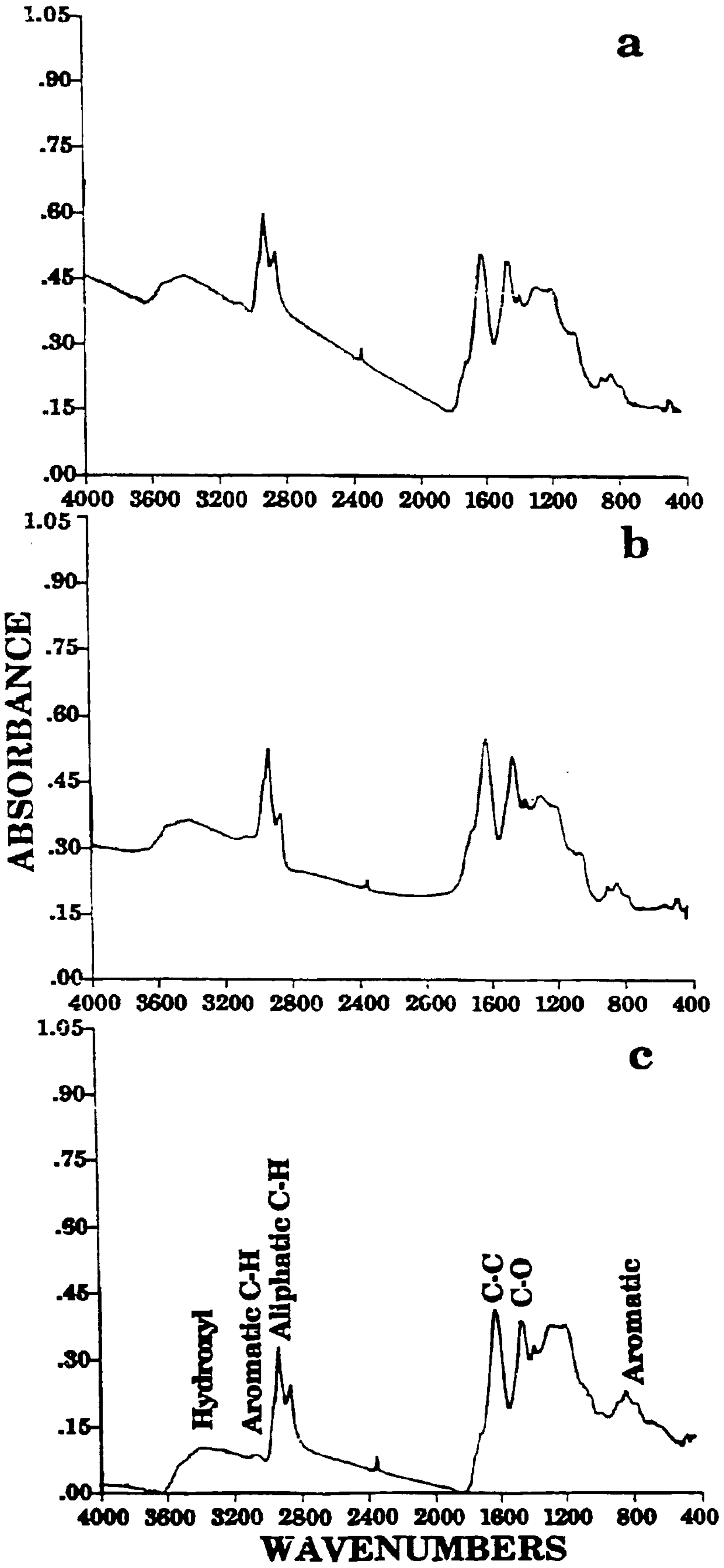

Figure II.A-6. FT-IR Spectra of Bulk Blind Canyon Bituminous Coal. a) KBr, b) CSI, and c) KBr Pellet, Mineral Matter Corrected.

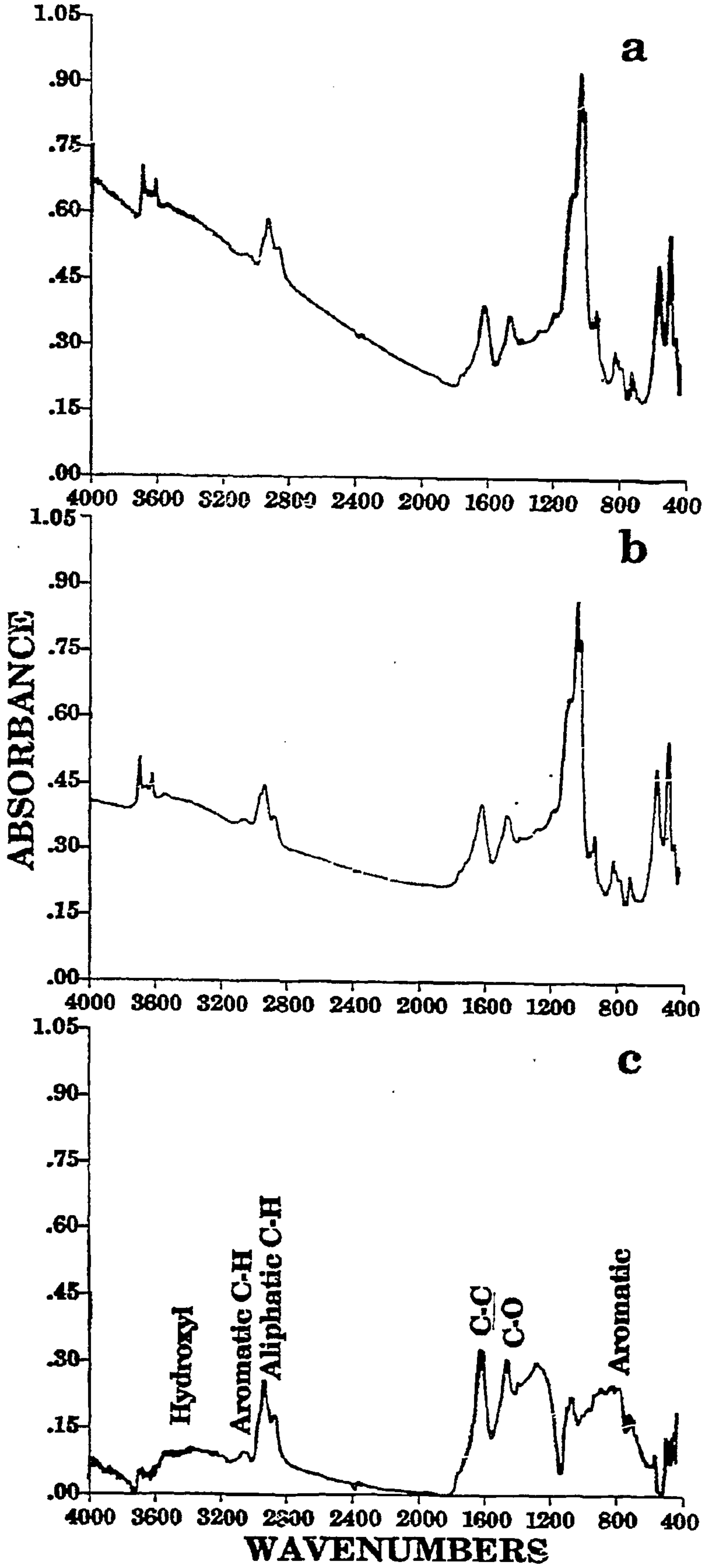

Figure II.A-7. FT-IR Spectra of Bulk Upper Knawha Bituminous Coal. a) KBr, b) CSI, and c) KBr Pellet. Mineral Matter Corrected.

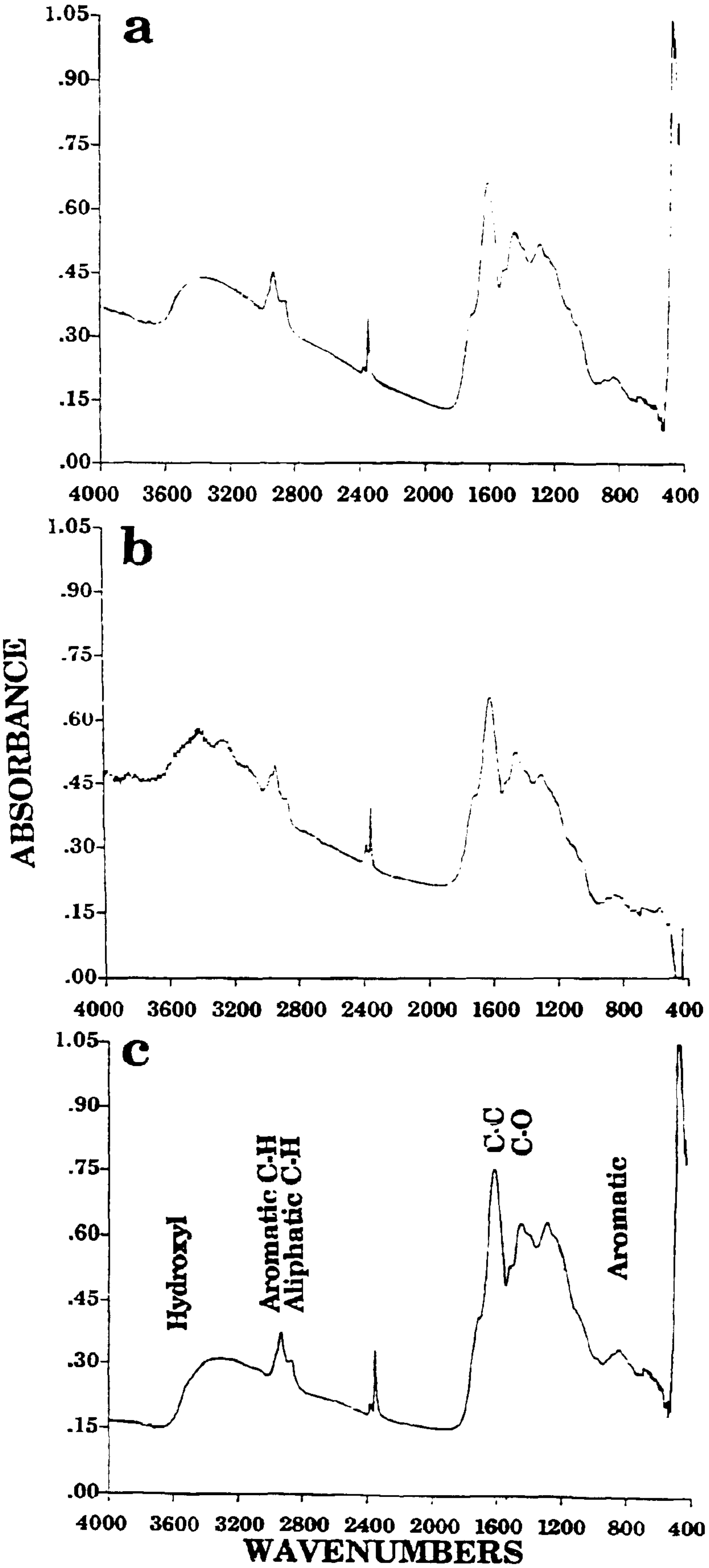

Figure II.A-8. FT-IR Spectra of Bulk Zap North Dakota Lignite. a) KBr, b) CSI, and c) KBr Pellet, Mineral Matter Corrected.

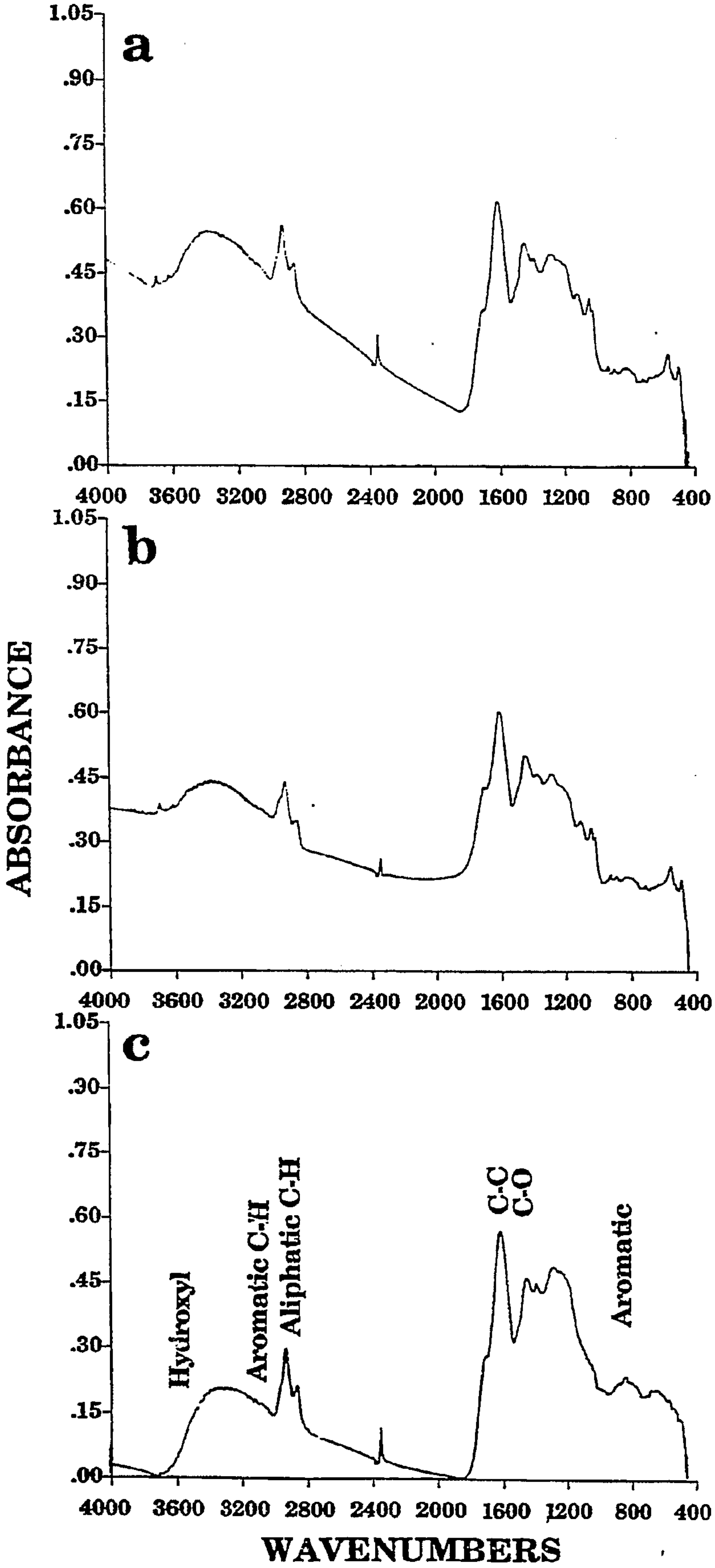

Figure II.A-9. FT-IR Spectra of Bulk Montana Rosebud Subbtuminous Coal. a) KBr, b) CSI, and c) KBr Pellet, Mineral Matter Corrected.

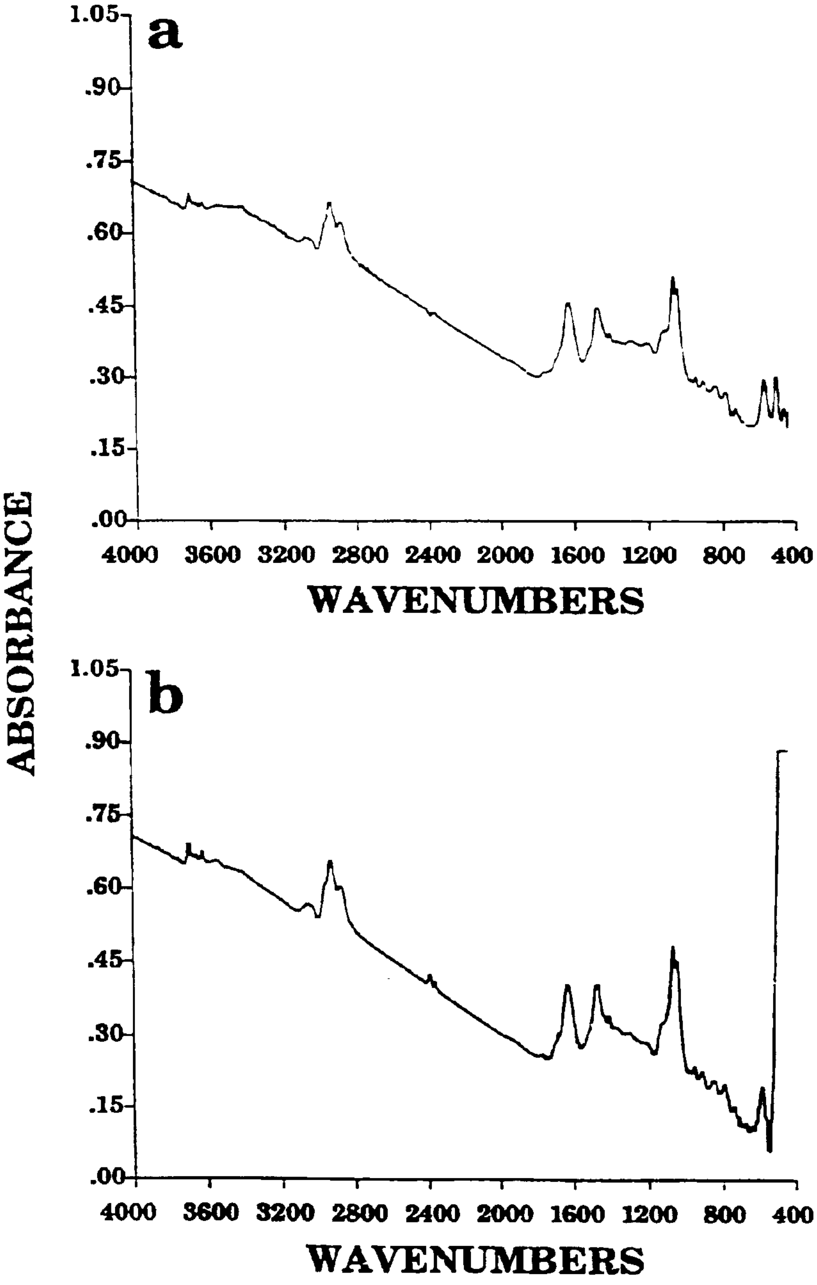

Figure II.A-10. Dry Uncorrected FT-IR Spectra of Upper Freeport Bituminous Coal. a) Bulk Sample and b) Ampoule Sample.

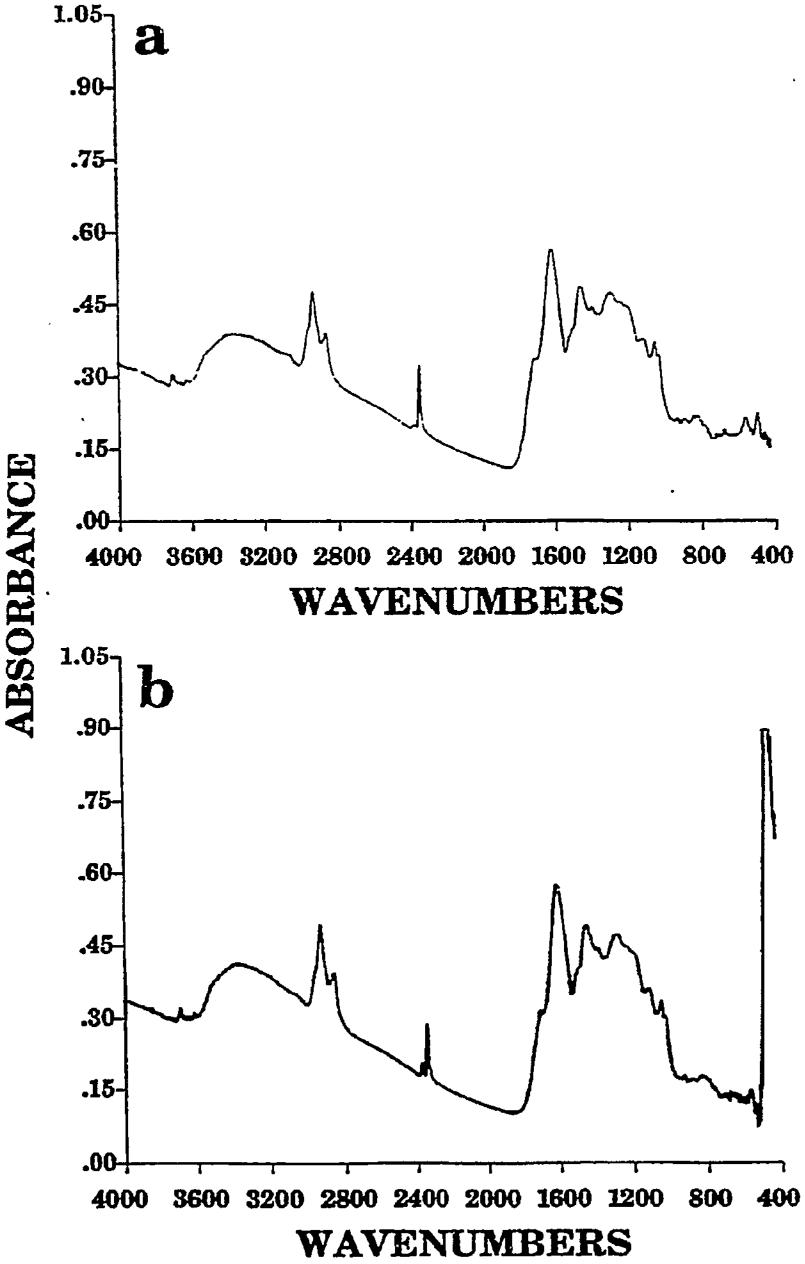

Figure II.A-11. Dry Uncorrected FT-IR Spectra of Wyodak Subbituminous Coal. a) Bulk Sample and b) Ampoule Sample.

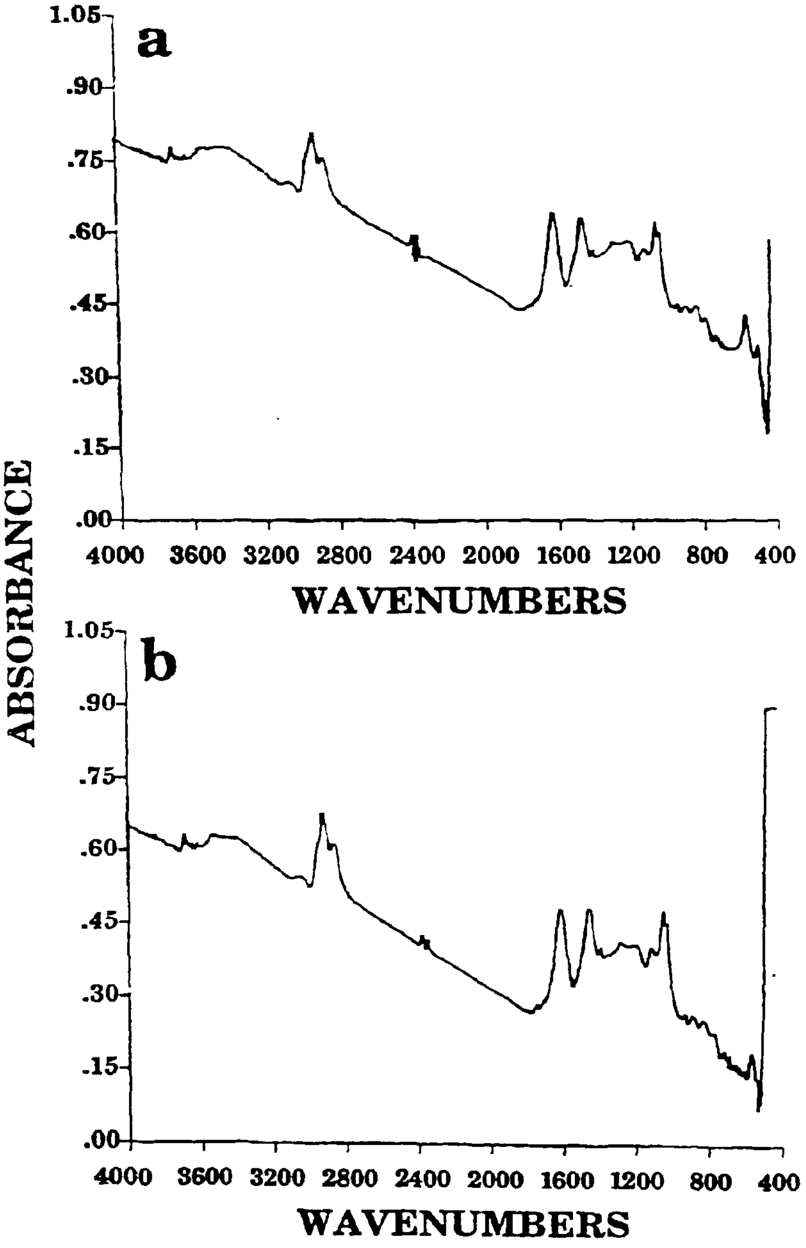

Figure II.A-12. Dry Uncorrected FT-IR Spectra of Pittsburgh Seam #8 Bituminous Coal. a) Bulk Sample and b) Ampoule Sample.

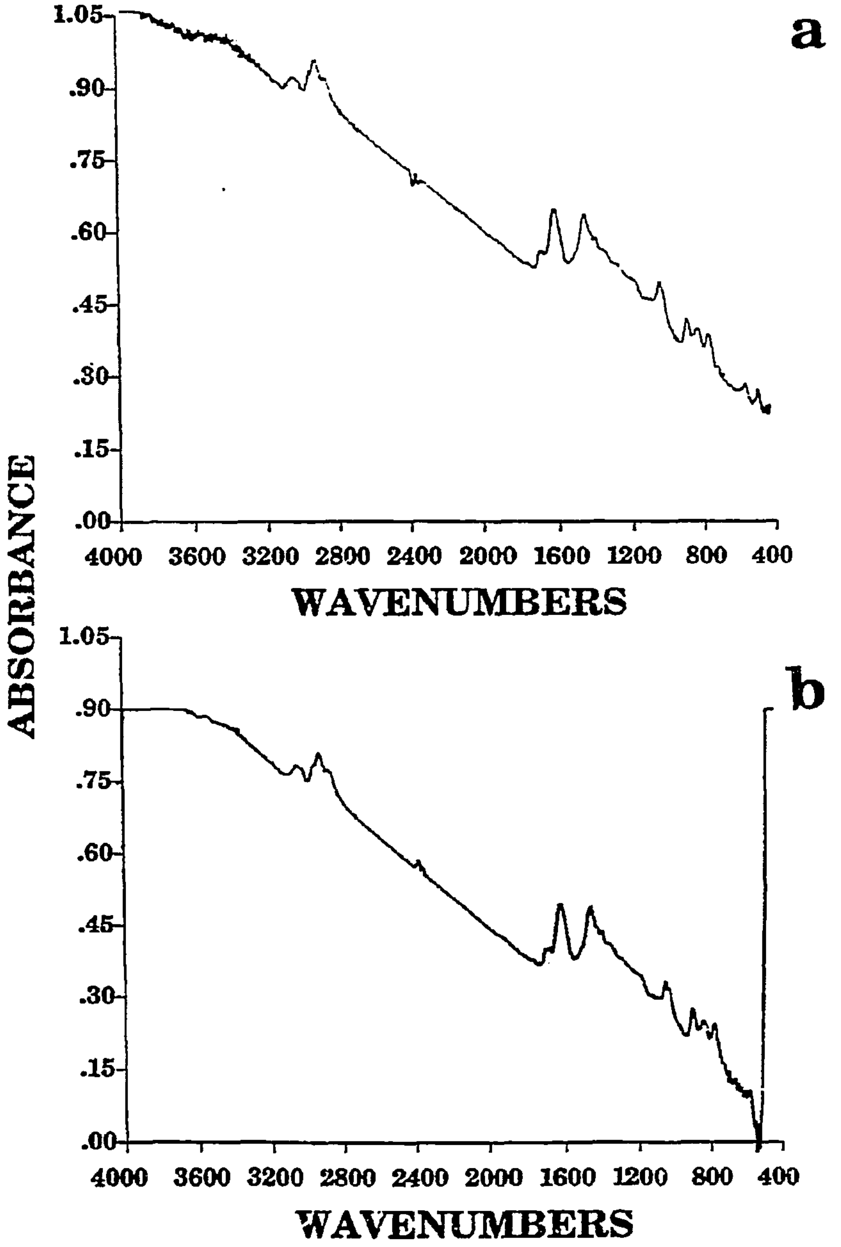

Figure II.A-13 Dry Uncorrected FT-IR Spectra of Pocahontas #3 Bituminous Coal. a) Bulk Sample and b) Ampoule Sample.

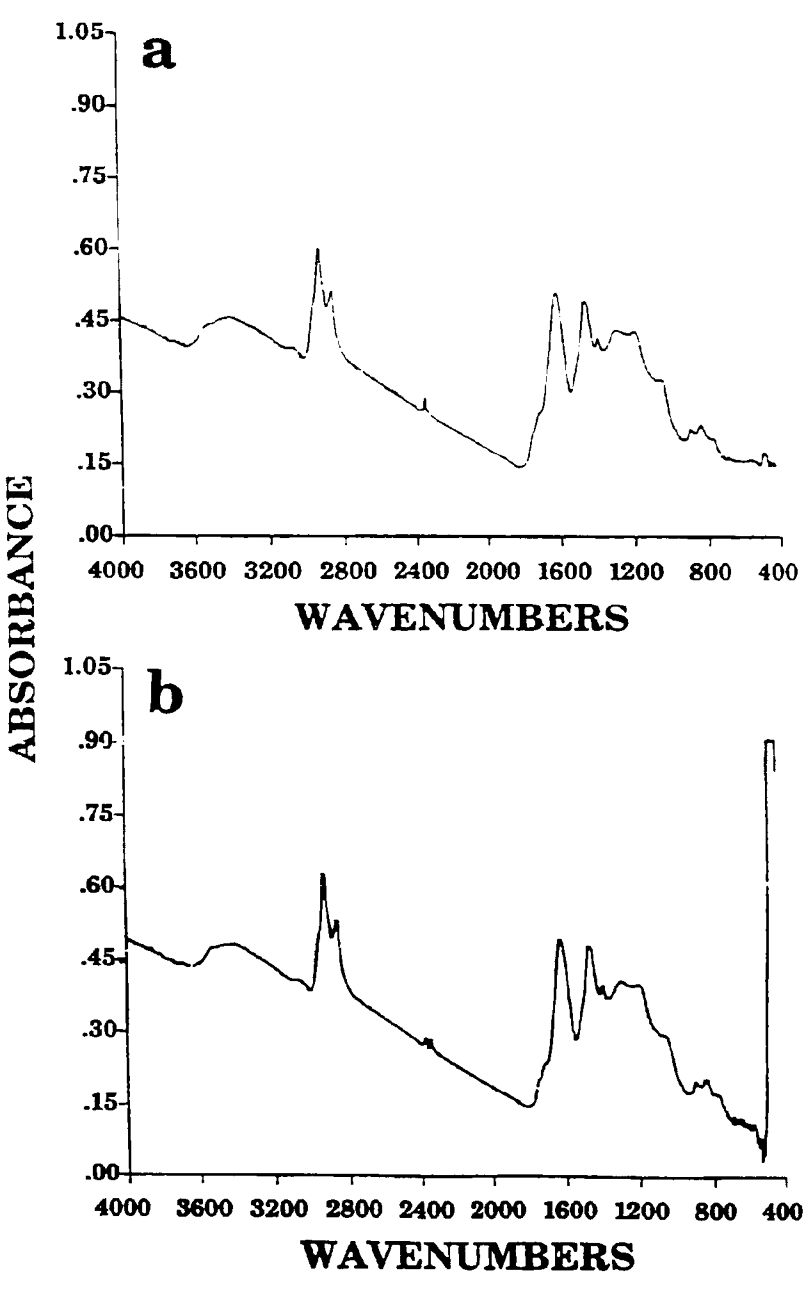

Figure II.A-14. Dry Uncorrected FT-IR Spectra of Utah Blind Canyon Bituminous Coal. a) Bulk Sample and b) Ampoule Sample.

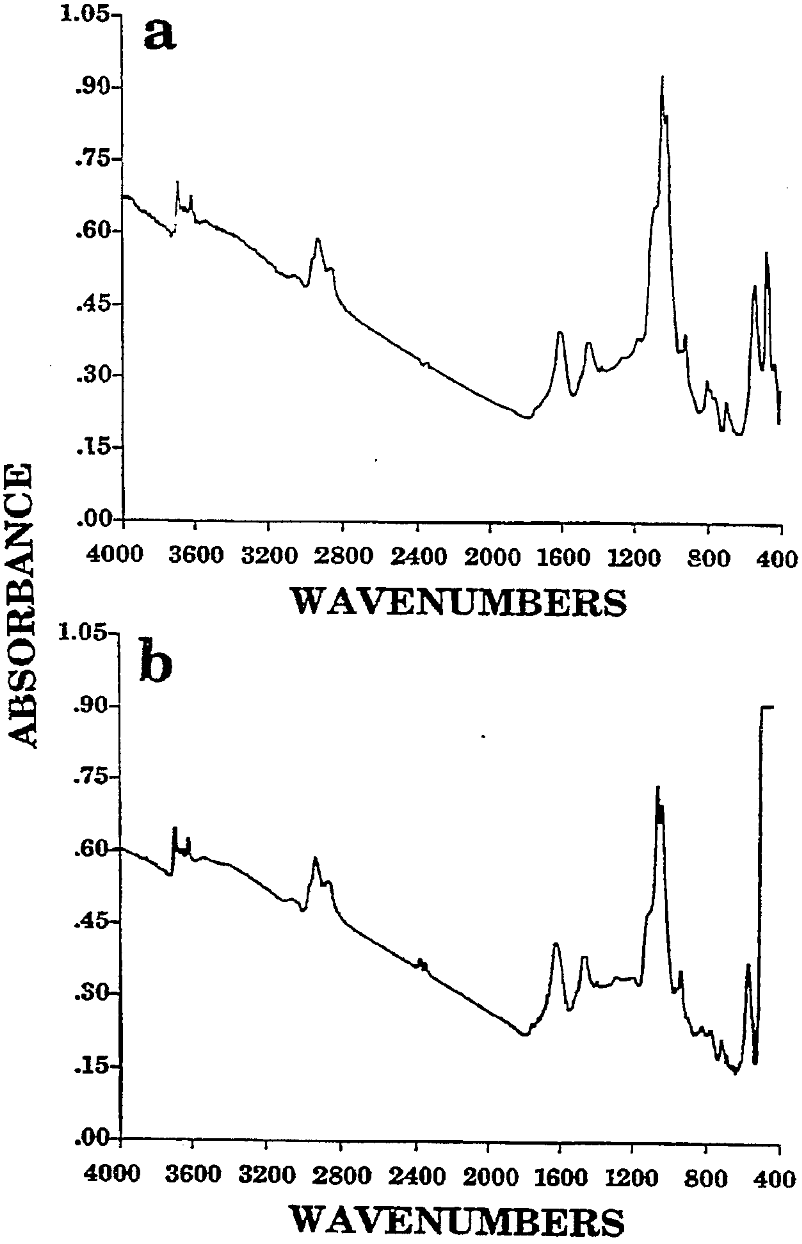

Figure II.A-15. Dry Uncorrected FT-IR Spectra of Upper Knawha Bituminous Coal. a) Bulk Sample and b) Ampoule Sample.

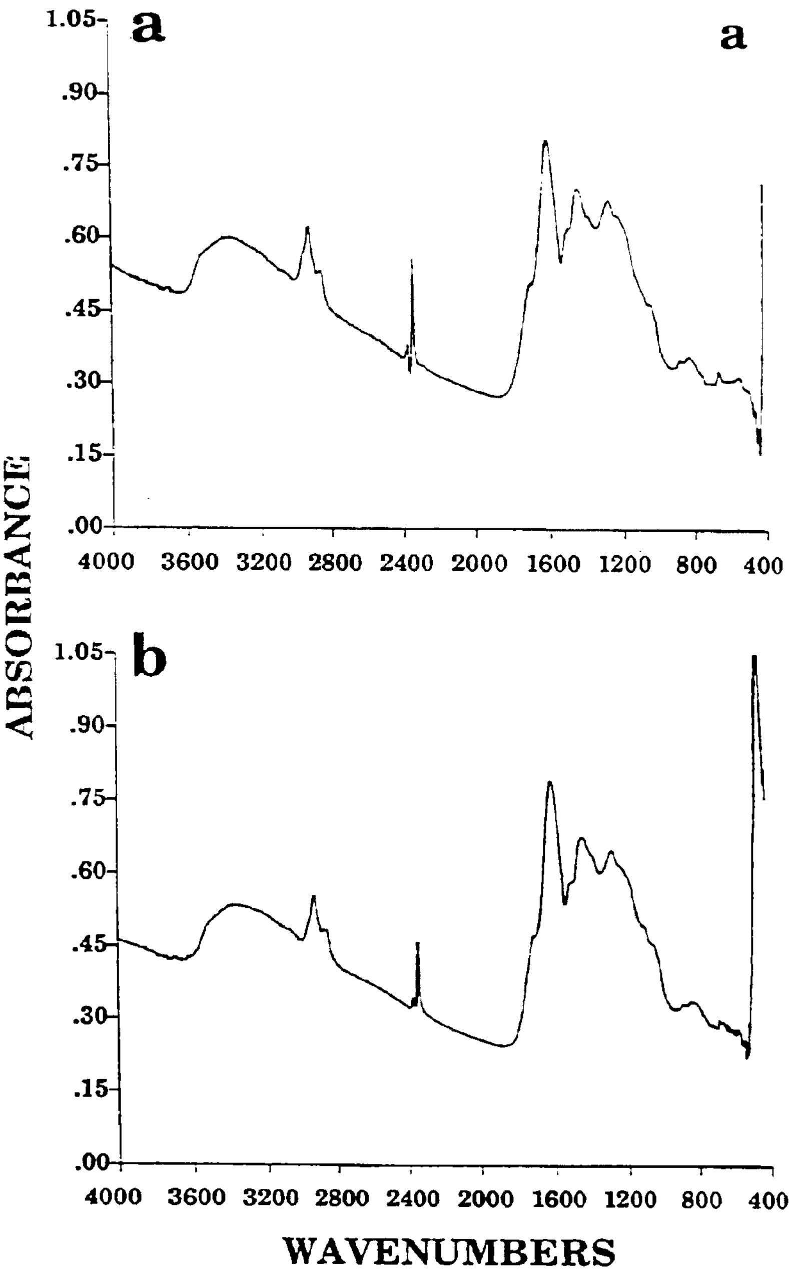

Figure II.A-16. Dry Uncorrected FT-IR Spectra of Beulah Zap Lignite. a) Bulk Sample and b) Ampoule Sample.

Table II.A-3

Data on Bulk Coals (weight Percent dmmf)*

	Hydrogen					Aromatic Hydrogen			Carbon	Carbonyl	Oxygen	
Sample	H_{al}	H_{oh}	H_{ar}	H_{total}	H_{ar}/H_{total}	1 Adj	2 Adj	3 or More	C_{al}	Units (Abs. x cm^{-1})	O_{oh}	O_{ether}
UF	2.84	0.14	1.59	4.57	0.35	0.50	0.59	0.50	18.93	1.69	2.23	1.11
WY	3.10	0.34	1.74	5.18	0.34	0.54	0.78	0.42	20.67	26.65	5.50	4.53
PITT#8	3.02	0.11	1.57	4.70	0.33	0.54	0.63	0.40	20.13	8.38	1.75	1.44
POC#3	1.96	0.13	2.19	4.28	0.51	0.68	0.75	0.76	13.06	1.09	2.06	0.40
UT	4.65	0.20	1.96	6.81	0.29	0.52	0.89	0.55	31.00	11.17	3.25	4.00
WV	3.77	0.19	1.59	5.55	0.29	---	---	---	25.13	7.35	3.09	2.48
ZAP	2.31	0.33	1.66	4.30	0.39	0.50	0.69	0.46	15.40	25.59	5.25	5.5
ROSEBUD	2.79	0.45	1.62	4.86	0.33	0.48	0.71	0.43	18.60	26.64	7.22	6.31

* Except Carbonyl: Relative Peak Area

Table II.A-4

Data on Ampoule Samples (weight Percent dmmf)*

	Hydrogen				Aromatic Hydrogen				Carbon	Carbonyl	Oxygen	
Sample	H_{al}	H_{oh}	H_{ar}	H_{total}	H_{ar}/H_{total}	1 Adj	2 Adj	3 or More	C_{al}	Units (Abs. x cm^{-1})	O_{oh}	O_{ether}
UF	3.43	0.11	2.08	5.62	0.37	0.66	0.71	0.71	22.87	0.63	1.75	0.75
WY	3.03	0.33	1.73	5.09	0.34	0.52	0.78	0.43	20.20	23.86	5.25	5.0
ILL#6	3.41	0.23	2.07	5.71	0.36	0.69	0.78	0.60	22.73	4.48	3.75	2.25
PITT#8	3.60	0.16	2.07	5.83	0.36	0.67	0.80	0.60	24.00	0.86	2.5	1.88
POC#3	1.97	0.06	2.19	4.22	0.52	0.60	0.73	0.86	13.93	1.92	1.0	1.25
UT	4.79	0.16	1.90	6.85	0.28	0.51	0.80	0.58	31.93	8.70	2.5	4.0
WV	3.48	0.23	2.12	5.83	0.36	0.67	0.67	0.79	23.20	3.59	3.75	1.75
ZAP	2.02	0.34	1.58	3.94	0.40	0.46	0.74	0.37	13.47	24.67	5.5	5.0

* Except Carbonyl: Relative Peak Area

Table II.A-5

Data on Bulk Coals (dry weight percent)

Minerals

Sample	Mixed Clay	Quartz	Calcite	Kaolin	Total
UF	9.06	0.86	1.98	2.63	14.53
WY	3.52	1.34	0.59	2.00	7.45
PITT#8	5.65	0.64	1.49	2.90	10.68
POC#3	4.91	0.53	3.88	0.45	9.76
UT	3.31	0.48	2.23	0.24	6.26
WV	21.40	4.79	1.08	8.44	35.71
ZAP	2.48	0.69	0.93	0.79	4.88
ROSEBUD	3.42	1.00	1.92	2.51	8.86

Table II.A-6

Data on Ampoule Samples (dry weight percent)

Minerals

Sample	Mixed Clay	Quartz	Calcite	Kaolin	Total
UF	10.40	0.93	2.97	3.60	17.90
WY	2.57	0.76	1.04	2.11	6.48
ILL#6	8.50	2.26	3.98	2.29	17.02
PITT#8	7.74	1.00	2.01	2.72	13.47
POC#3	4.28	0	4.83	0.99	10.11
UT	2.90	0.12	2.40	0.17	5.59
WV	15.50	1.24	1.46	7.74	25.95
ZAP	2.36	0.73	1.38	0.71	5.18

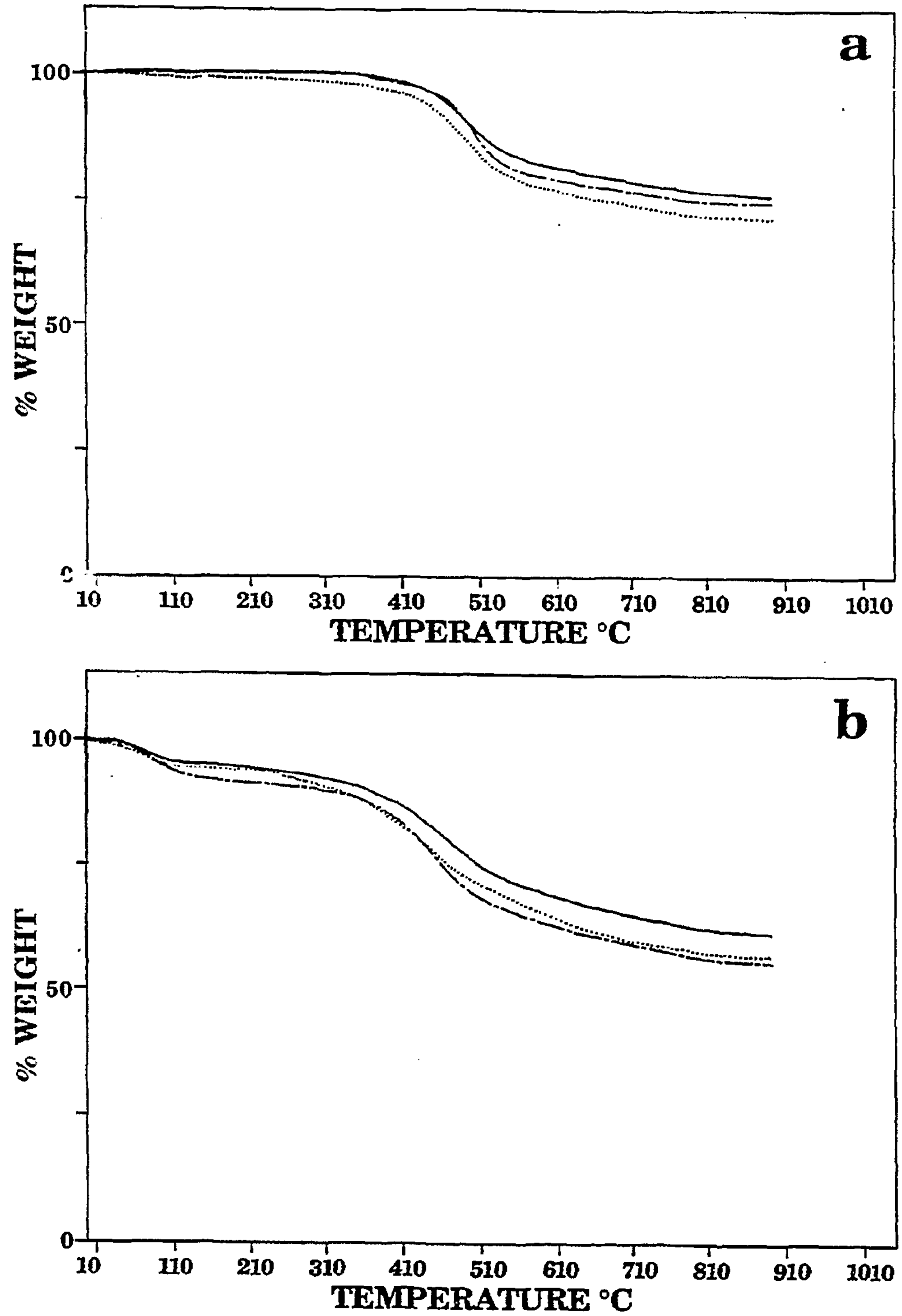

Figure II.A-17. Pyrolysis of a) Upper Freeport Bituminous Coal and b) Wyodak Subbituminous Coal in TGA at 30°C/min in N_2. Solid, Dashed, and Dotted Lines Represent Bulk, Ampoule and Demineralized Samples, Respectively.

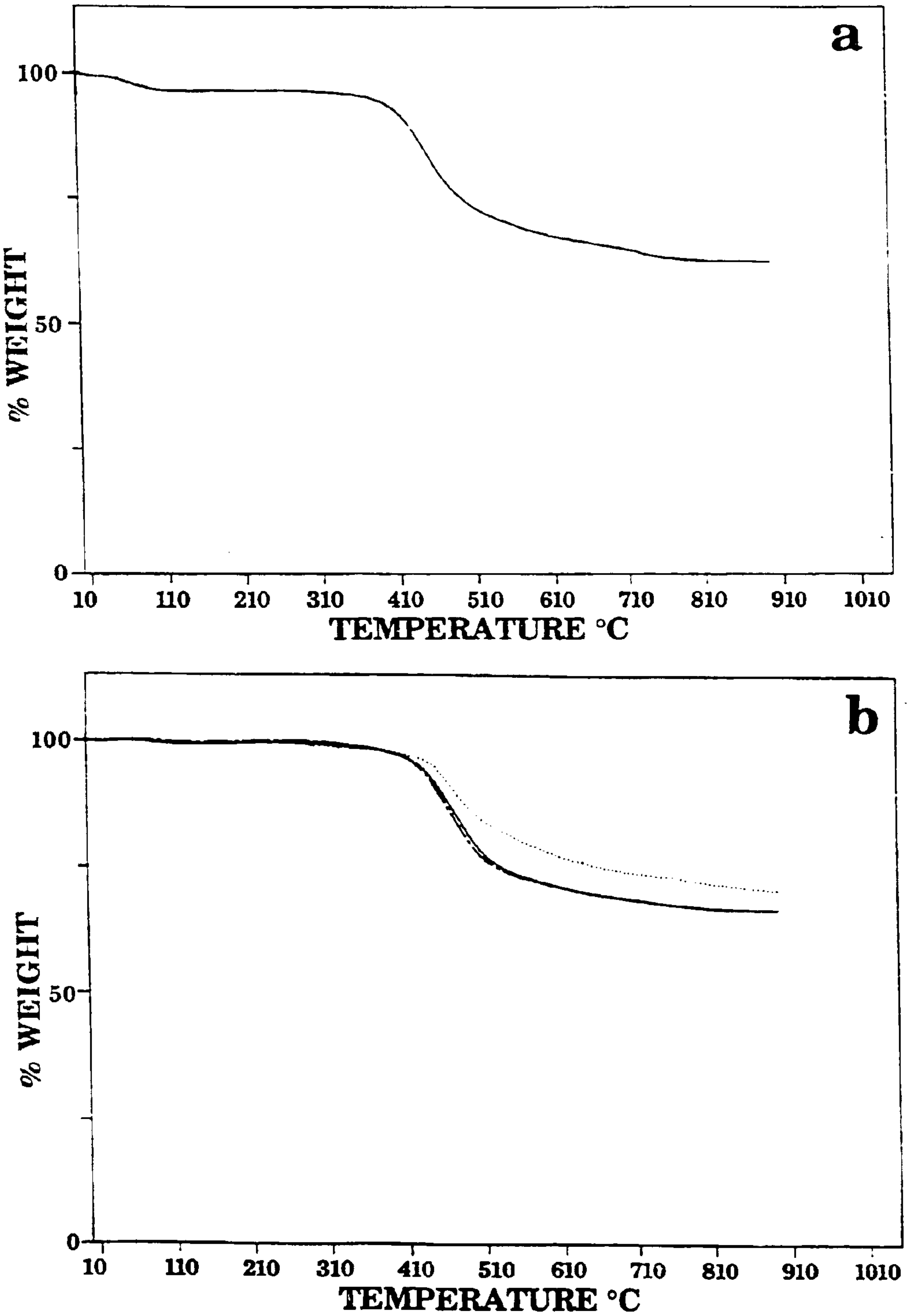

Figure II.A-18. Pyrolysis of a) Illinois #6 Bituminous Coal and b) Pittsburgh Seam Bituminous Coal in TGA at 30°C/min in N_2. Solid, Dashed, and Dotted Lines Represent Bulk, Ampoule and Demineralized Samples, Respectively.

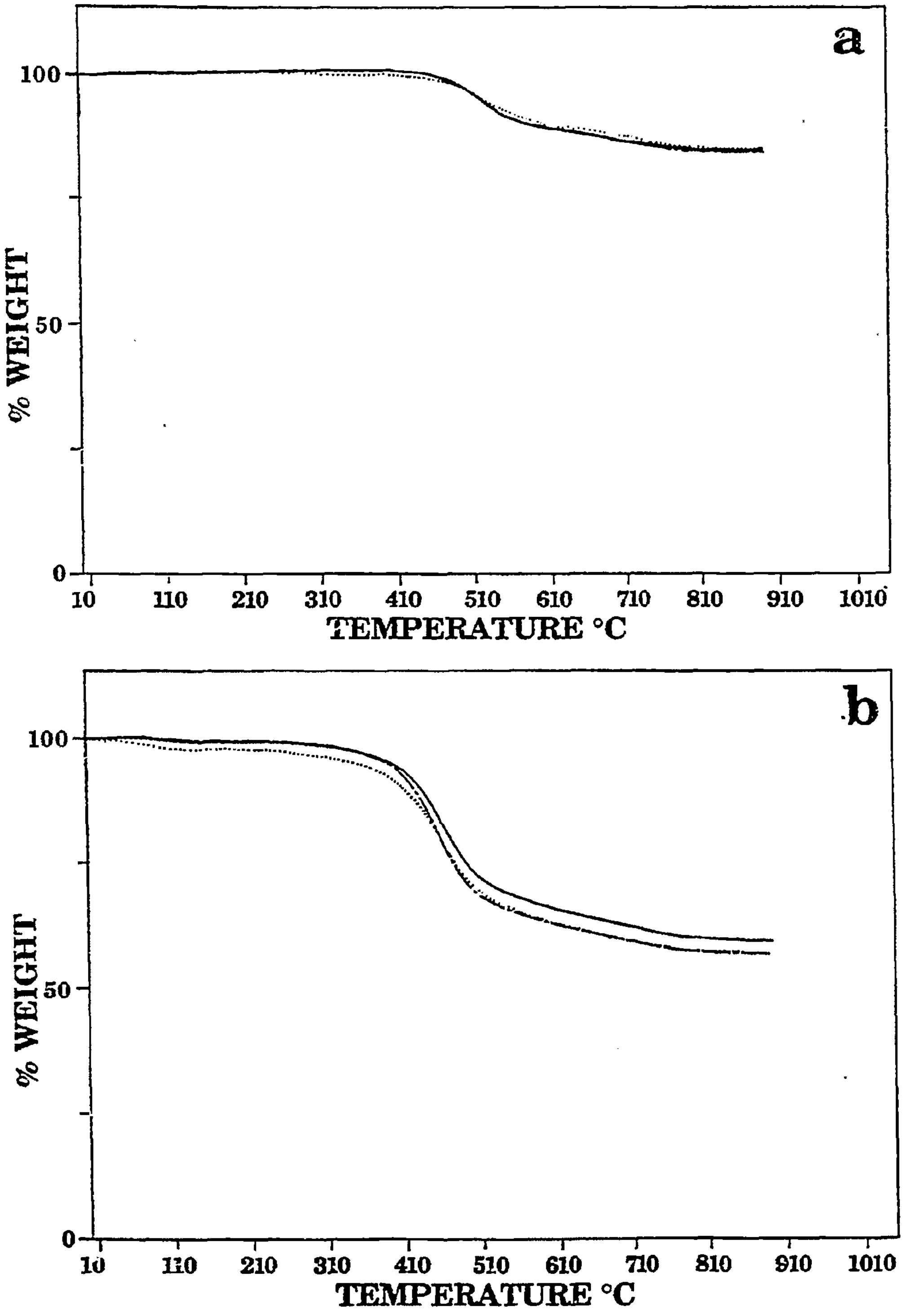

Figure II.A-19. Pyrolysis of a) Pocahontas #3 Bituminous Coal and b) Utah Blind Canyon Bituminous Coal in TGA at 30°C/min in N_2. Solid, Dashed, and Dotted Lines Represent Bulk, Ampoule and Demineralized Samples, Respectively.

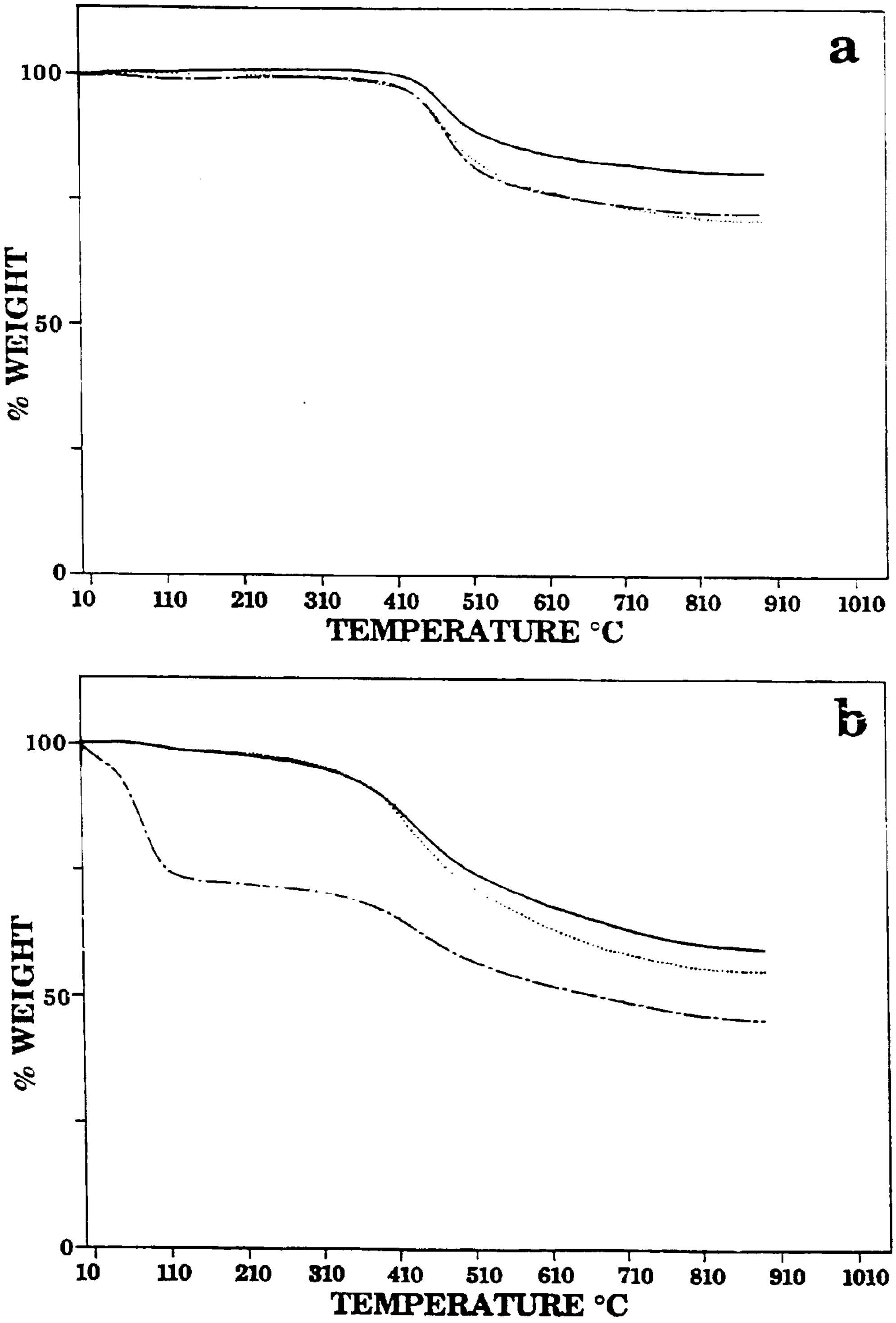

Figure II.A-20. Pyrolysis of a) Upper Knawha Bituminous Coal and b) Zap North Dakota Lignite in TGA at 30°C/min in N_2. Solid, Dashed, and Dotted Lines Represent Bulk, Ampoule and Demineralized Samples, Respectively.

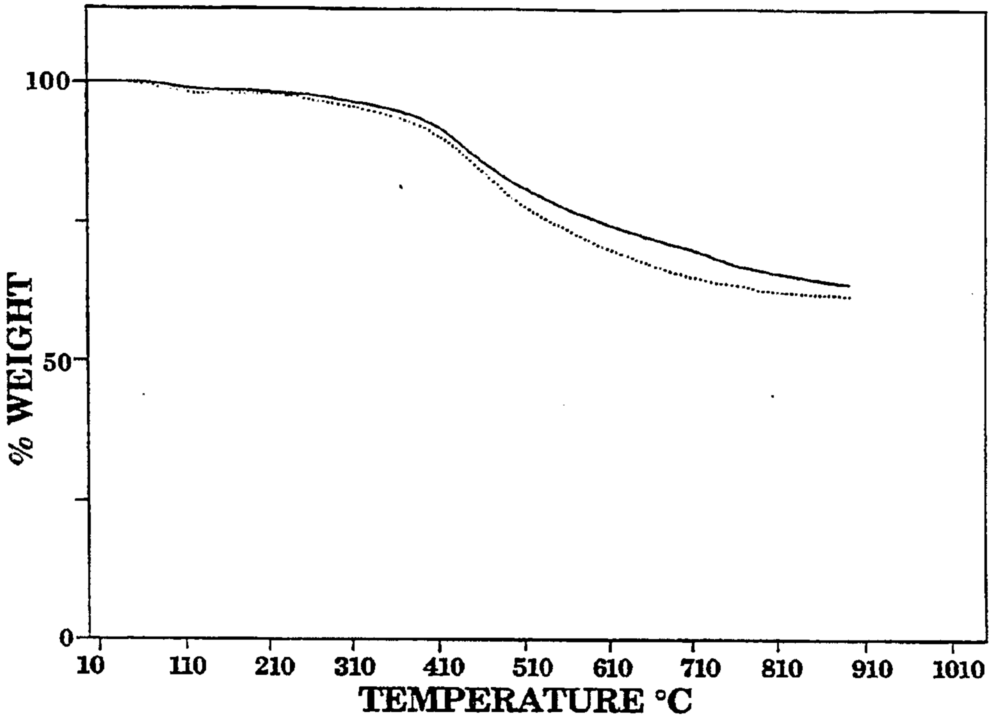

Figure II.A-21. Pyrolysis of Upper Montana Rosebud Subbituminous Coal in TGA at 30°C/min in N_2. Solid, Dashed, and Dotted Lines Represent Bulk, Ampoule and Demineralized Samples, Respectively.

for Wyodak, Upper Knawha, and North Dakota (Zap) lignite.

Char Reactivity in TGA

The reactions of chars prepared from both raw and demineralized coals were measured. The chars were prepared by pyrolysis as described above. The char reactivity measurements were made by employing a non-isothermal technique using the TGA. With an air flow of 40 cc/min and a N_2 purge flow of 40 cc/min, the samples were heated at a rate of 30°C/min until 900°C was reached. The resulting critical temperatures (defined as the temperature at which the derivative of the weight loss reaches 0.11 weight fraction/min) are listed in Table II.A-7 and are also plotted in Fig. II.A-22 as functions of oxygen in the parent coal.

Figure II.A-22a compares the bulk and ampoule samples. There is good agreement between the two and the trend is an increase in reactivity (decreasing T_{cr}) with increasing oxygen.

Figure II.A-22b compares the raw bulk samples with the demineralized samples. The reactivities show interesting trends. Above 15% O_2, the ash content of the coal dominates the char reactivity, increasing the char's reactivity (lower T_{cr}) compared to the demineralized samples. The reason for this increase appears to be the catalytic activity of the organically bound alkali metals as will be discussed in Section II.d. Below 10% O_2, the raw coals have a lower reactivity (higher T_{cr}) than the demineralized samples. The reason for this is not known and is being investigated.

Determination of Percent Ash

Ash percent values ascertained through three different analytical techniques are listed in Table II.A-8. The values are in good agreement for the Argonne ampoule samples. These samples (excluding Montana sample) which were from amber borosilicate glass ampoules flame sealed under nitrogen were subjected to x-ray analysis, TGA analysis and Argonne's proximate analysis. There is more scatter for the bulk samples and the Montana Rosebud subbituminous which were not as well homogenized as the Argonne ampoule samples. The ash in the bulk sample of the upper Knawha coal is much higher than in the ampoules.

Table II.A-7.

Data on Char Reactivity

Coal Name	Abbreviation	Rank	Wt. % Oxygen in Original Coal Sample by Difference (DMMF)	0 - 900°C N_2 Char					
				Ampoules		Bulk Sample		Demineralized Bulk Sample	
				T_{cr}	%Ash	T_{cr}	%Ash	T_{cr}	%Ash
1. Upper Freeport	UF	Medium Volatile Bituminous	4	644	13.81	641	11.63	513	1.93
2. Wyodak	WY	Subbituminous	19	436	8.07	440	11.13	503	0.40
3. Illinois #6	ILL	High Volatile Bituminous	10	519	15.02	---	---	---	---
4. Pittsburgh #8	PITT	High Volatile Bituminous	8	586	9.61	600	9.01	542	1.44
5. Pocahontas #3	POC	Low Volatile Bituminous	3	607	5.10	611	4.83	564	---
6. Utah Blind Canyon	UT	High Volatile Bituminous	13	527	4.45	528	4.68	516	0.80
7. Upper Knawha	WV	Medium Volatile Bituminous	11	529	19.49	544	26.44	498	1.24
9. North Dakota	ZAP	Lignite	21	443	8.98	434	7.54	550	0.26
10. Rosebud		Subbituminous	20	---	---	478	14.72	508	3.47

*HF/HCL demineralized.

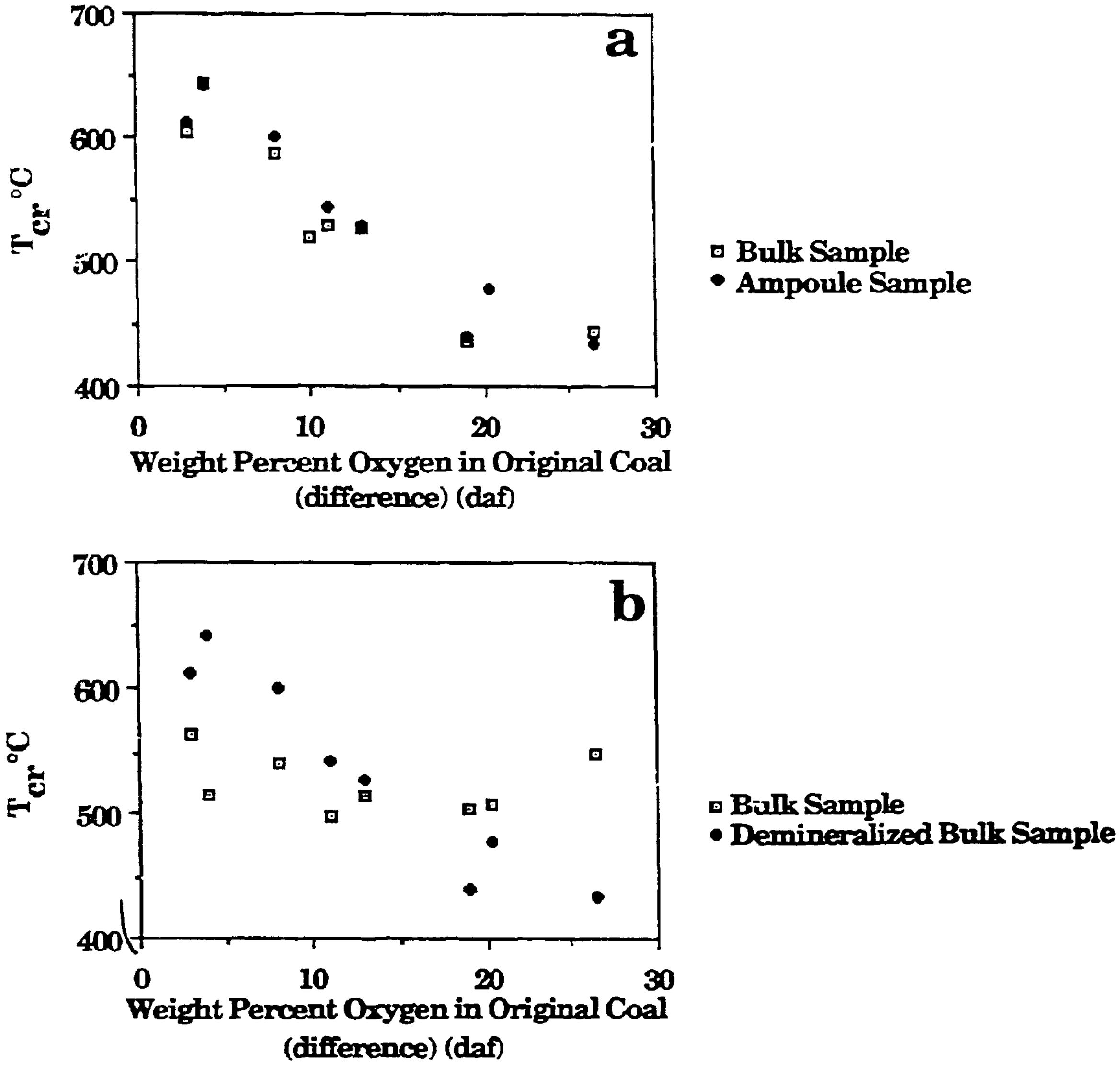

Figure II.A-22. Variation of Reactivity with Coal Rank for Chars Prepared by Heating in Nitrogen at 30°C/min to 900°C.

Table II.A-8. Ash in Dry Weight Percent

Analysis Type	**Upper Freeport**	**Wyodak**	**Illinois No.6**	**Pittsburgh No.8**	**Pocohontas No.3**	**Utah Blind Canyon**	**Upper Knawha**	**North Dakota Lignite**	**Montana Rosebud**
TGA Ampoule	13.81	8.07	15.02	9.61	5.00	4.45	19.49	8.98	---
TGA Bulk	11.63	11.13	--	9.01	4.83	4.68	26.44	7.54	14.72
X-Ray Ampoule	12.49	9.02	16.14	8.51	4.40	3.41	21.48	9.60	12.33
Argonne Proximate (ampoule)	13.16	8.95	17.76	9.44	4.90	4.68	19.81	6.53	--

Pyrolysis in Entrained Flow Reactor (EFR)

The 200 x 325 mesh sieved fractions of 6 of the Argonne coals were pyrolyzed in the entrained flow reactor. The coals were vacuum dried at 105°C for 1 hour prior to the pyrolysis runs. The coal was fed at rates of 1 1/2 - 2 g/min with a N_2 carrier. Particle residence time was approximately 0.66 seconds with the injector height position adjusted to 24" and the furnace operated at 1400°C, 1100°C, and 700°C. The gas analyses were performed using two analytical techniques: 1) FT-IR calibration program and 2) Gas Chromatograph.

The data are presented in Tables II.A-9 to II.A-11. The data are plotted for each coal as a function of temperature in Figs. II.A-23 to II.A-28. The yields show the expected dependence on temperature. These data, as well as data from the TG-FTIR will be modeled using the FG/DVC model during the next year.

FG/DVC Model Development

The combined Functional Group (FG) and Devolatilization, Vaporization, and Crosslinking (DVC) model developed under METC Contract No. DE-AC21-85MC22050 is being improved for application to this program. The FG/DVC model predicts the time and temperature evolution of tar, char, and gases in pyrolysis including:

- Gas (composition and concentration)
- Tar (yield, elemental composition, functional group concentration, molecular weight distribution)
- Char (yield, elemental composition, functional group concentration, extract yield, crosslink density, and viscosity)

A comprehensive description of the model has been prepared for publication. This manuscript is included as Appendix A. The improvements made under the current program are described below.

Mass Transport Limitations

During the past year, work was performed on the mass transport within the particle. This improvement was required, since when comparing the predictions of the model to available data it was found that tar yields were overpredicted when devolatilization occurred at low temperatures. This was observed for either low heating rate experiments (Serio et al., 1987) or experiments with rapid heating to

Table II.A-9.

Pyrolysis in the Entrained Flow Reactor in Nitrogen at 700°C, 24".

Values in Ash Free Weight Percent.

AFR/BYU Run # Species	19 Upper Freeport	20 Upper Knawha	21 Pittsburgh #8	22 Wyodak	23 Pocahontas #3	24 Utah Blind Canyon
Char	64.88	66.95	57.49	59.56	80.64	54.8
Tar & Soot	22.07	17.22	30.5	13.09	10.29	25.8
Gas	5.85	6.95	7.44	13.46	3.83	13.62
H_2O	6.68	3.62	5.96	2.27	2.71	.95
Missing	.53	5.27	-1.4	11.62	2.52	4.83
CH_4	.92	.678	1.1	.696	.784	1.25
CO	.122	.449	.506	2.44	.118	1.04
H_2	0	0	0	0	0	0
CO_2	.408	1.16	.331	4.82	.81	3.47
C_2H_2	.021	.002	.006	.007	1.4×10^{-4}	0.1
C_2H_4	.372	.271	.433	.452	.095	.623
C_2H_6	.373	.169	.393	.198	.201	.66
C_3H_6	.305	.591	.589	.703	.106	.83
C_6H_6	.002	.609	.217	.406	.338	.24
CS_2	.145	.107	.108	.134	.074	.07
SO_2	.024	0	.014	.01	0	.01
HCN*	.094	0	0	0	0	.12
Paraffins	1.93	2.17	2.46	1.73	1.09	3.54
Olefins	1.57	.744	1.32	1.77	.208	1.77

* HCN values not included in gas totals or missing totals.

Table II.A-10.

Pyrolysis in the Entrained Flow Reactor in Nitrogen at 1100°C, 24".

Values in Ash Free Weight Percent.

AFR/BYU Run # Species	10 Upper Freeport	11 Wyodak	12 Upper Freeport	13 Upper Knawha	14 Utah Blind Canyon	15 Pittsburgh #8	16 Pocahontas #3
Char	52.50	43.16	52.14	56.52	40.94	47.91	73.50
Tar & Soot	21.65	7.71	16.59	14.35	13.40	21.84	11.69
Gas	25.99	40.14	24.94	21.49	39.28	28.62	14.17
H_2O	1.73	2.85	3.40	5.64	7.02	4.58	3.58
Missing	-1.88	6.14	2.93	2.60	-.64	-2.95	-2.94
CH_4	4.37	1.86	4.01	3.80	5.34	5.55	3.23
CO	5.46	12.27	5.40	4.16	8.85	6.04	1.82
H_2	1.38	.99	1.22	.77	1.5	1.21	1.04
CO_2	1.91	9.29	2.02	1.02	6.07	1.62	1.03
C_2H_2	1.49	2.09	1.21	.73	2.01	1.06	1.23
C_2H_4	1.95	2.27	1.76	1.84	2.84	2.29	.96
C_2H_6	.005	.006	.009	.15	.05	.08	.08
C_3H_6	.15	.24	.15	.20	.24	.25	.06
C_6H_6	3.32	5.26	3.45	3.23	3.97	3.98	2.08
CS_2	.18	.24	.25	.14	.164	.16	0.097
SO_2	.03	.012	.029	--	.002	.018	---
HCN *	2.16	1.49	1.93	1.36	2.98	2.07	.70
Paraffins	.56	.44	.59	.83	.55	.61	.33
Olefins	3.05	3.66	2.89	3.26	4.68	3.68	1.51

* HCN values not included in gas totals or missing totals.

Table II.A-11.

Pyrolysis in the Entrained Flow Reactor in Nitrogen at 1400°C, 24".

Values in Ash Free Weight Percent

AFR/BYU Run # Species	1 Pocahontas #3	2 Pocahontas #3 Re-run of Run #1	3 Upper Knawha	4 Wyodak	5 Upper Freeport	6 Utah Blind Canyon	8 Wyodak Re-run of Run #4	9 Pittsburgh #8
Char	70.03	70.19	51.22	44.82	46.64	35.24	42.82	37.38
Tar & Soot	13.54	13.22	20.05	15.54	25.85	28.52	13.44	29.75
Gas	14.22	15.34	22.28	43.0	21.91	33.49	45.18	30.64
H_2O	.58	2.23	1.37	2.40	.64	.85	1.46	1.80
Missing	1.23	-.99	5.08	-3.36	4.94	1.90	-2.90	.43
CH_4	.24	.19	.16	.16	.14	.28	.41	.19
CO	7.21	8.27	15.80	30.25	12.95	22.72	31.12	18.92
H_2	4.38	4.11	4.22	4.17	4.55	5.19	4.0	4.82
CO_2	.49	.70	1.80	5.75	1.28	1.42	6.74	1.96
C_2H_2	1.83	1.87	.03	2.36	2.59	3.72	2.59	4.33
C_2H_4	.56	.04	.06	.04	.05	.12	.054	.10
C_2H_6	1.73×10^{-5}	.02	4.86×10^{-6}	.01	.01	6.34×10^{-4}	.001	2.91×10^{-3}
C_3H_6	.03	.01	.02	.04	.03	.03	.01	-1.14×10^{-2}
C_6H_6	.01	.01	.01	.01	.01	.01	.006	1.25×10^{-2}
CS_2	.08	.17	.17	.20	.26	.11	.183	.28
SO_2	.00	.01	.01	.01	.01	.01	.009	1.11×10^{-2}
HCN *	2.22	2.20	3.96	3.30	4.36	5.65	3.56	5.54
Paraffins	0	.109	0	0	0	0	.06	.00
Olefins	0	0	0	0	0	.03	0	-.07

* HCN values not included in gas totals or missing totals.

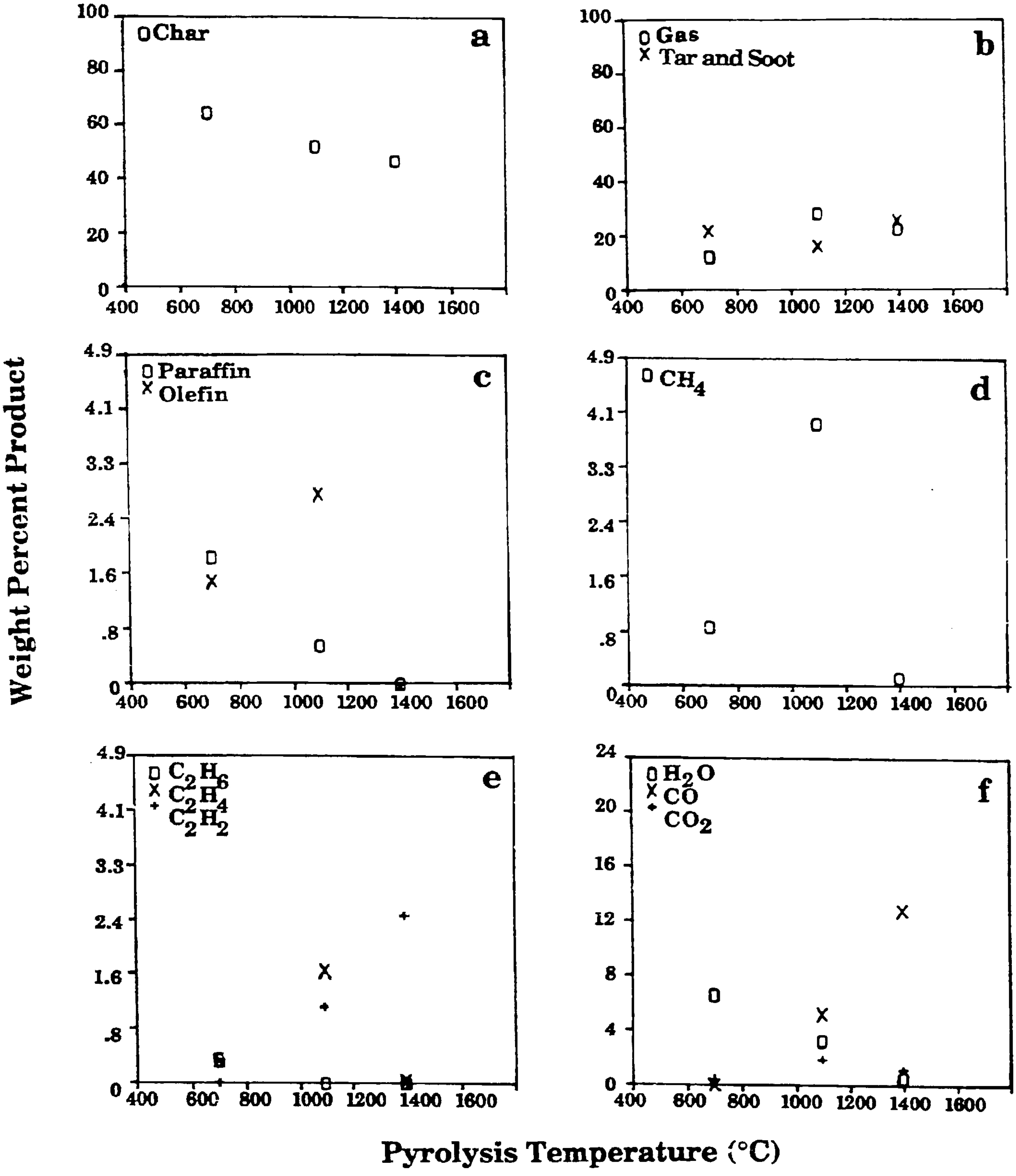

Figure II.A-23. Pyrolysis Results for Upper Freeport Bituminous Coal, 200 x 325 Mesh, in the Entrained Flow Reactor at a Reaction Distance of 24". The Coal was Fed at Rates of 1 1/2 - 2 g/min with an N_2 Carrier Particle Residence Time was Approximately 0.66 Seconds.

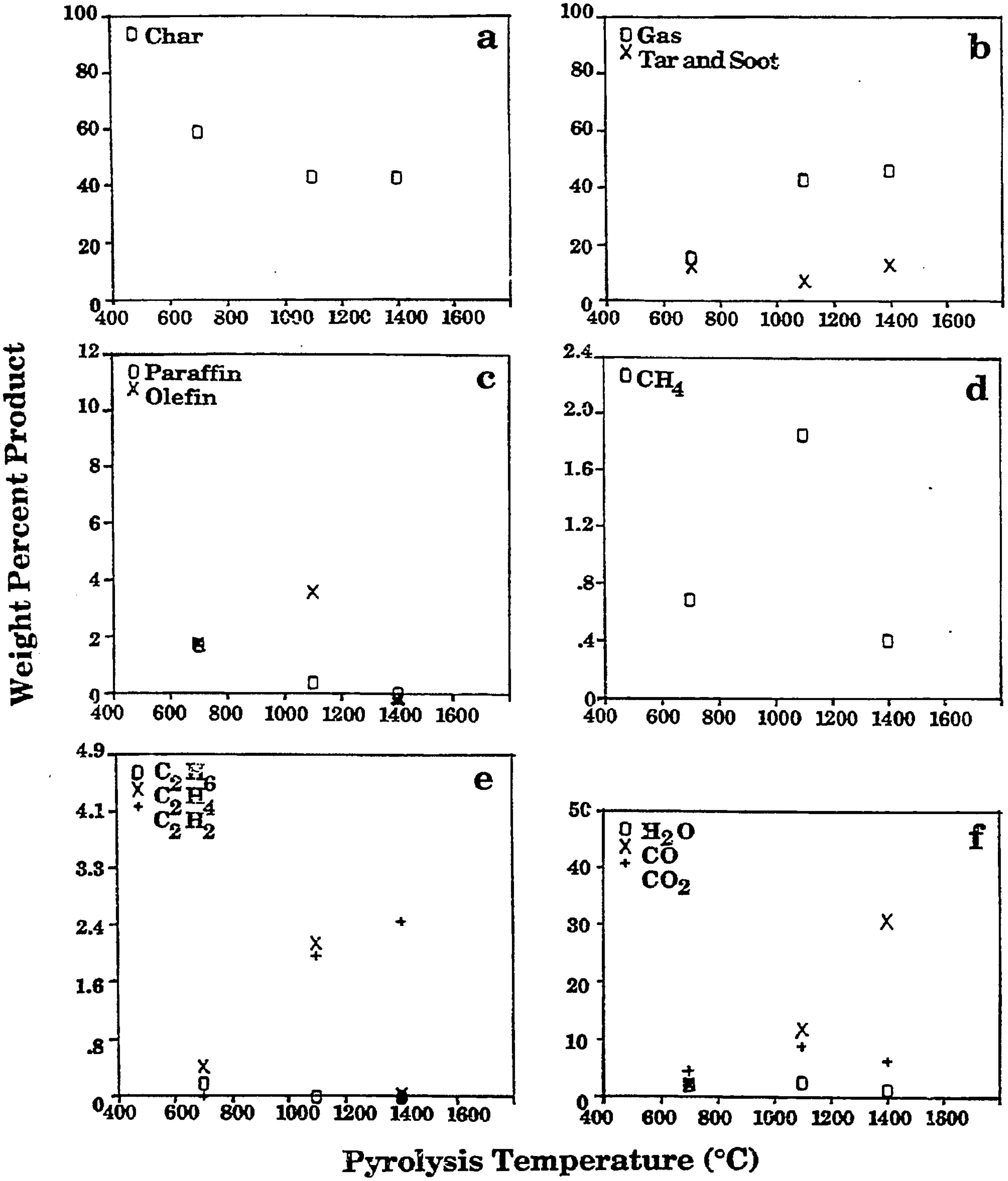

Figure II.A-24. Pyrolysis Results for Wyodak Subbituminous Coal, 200 x 325 Mesh, in the Entrained Flow Reactor at a Reaction Distance of 24". The Coal was Fed at Rates of 1 1/2 - 2 g/min with an N_2 Carrier Particle Residence Time was Approximately 0.66 Seconds.

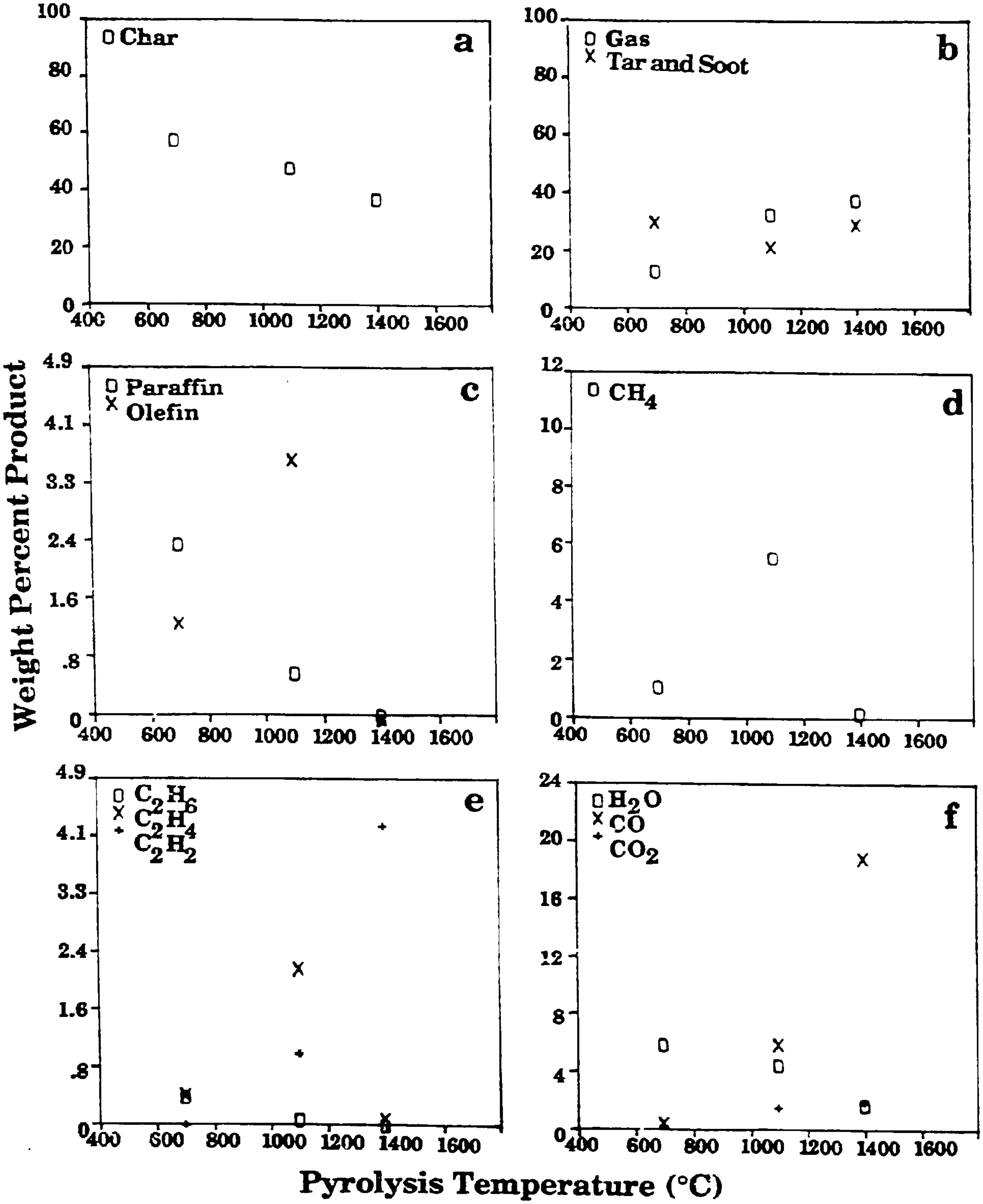

Figure II.A-25. Pyrolysis Results for Pittsburgh Seam Bituminous Coal, 200 x 325 Mesh, in the Entrained Flow Reactor at a Reaction Distance of 24". The Coal was Fed at Rates of 1 1/2 - 2 g/min with an N_2 Carrier Particle Residence Time was Approximately 0.66 Seconds.

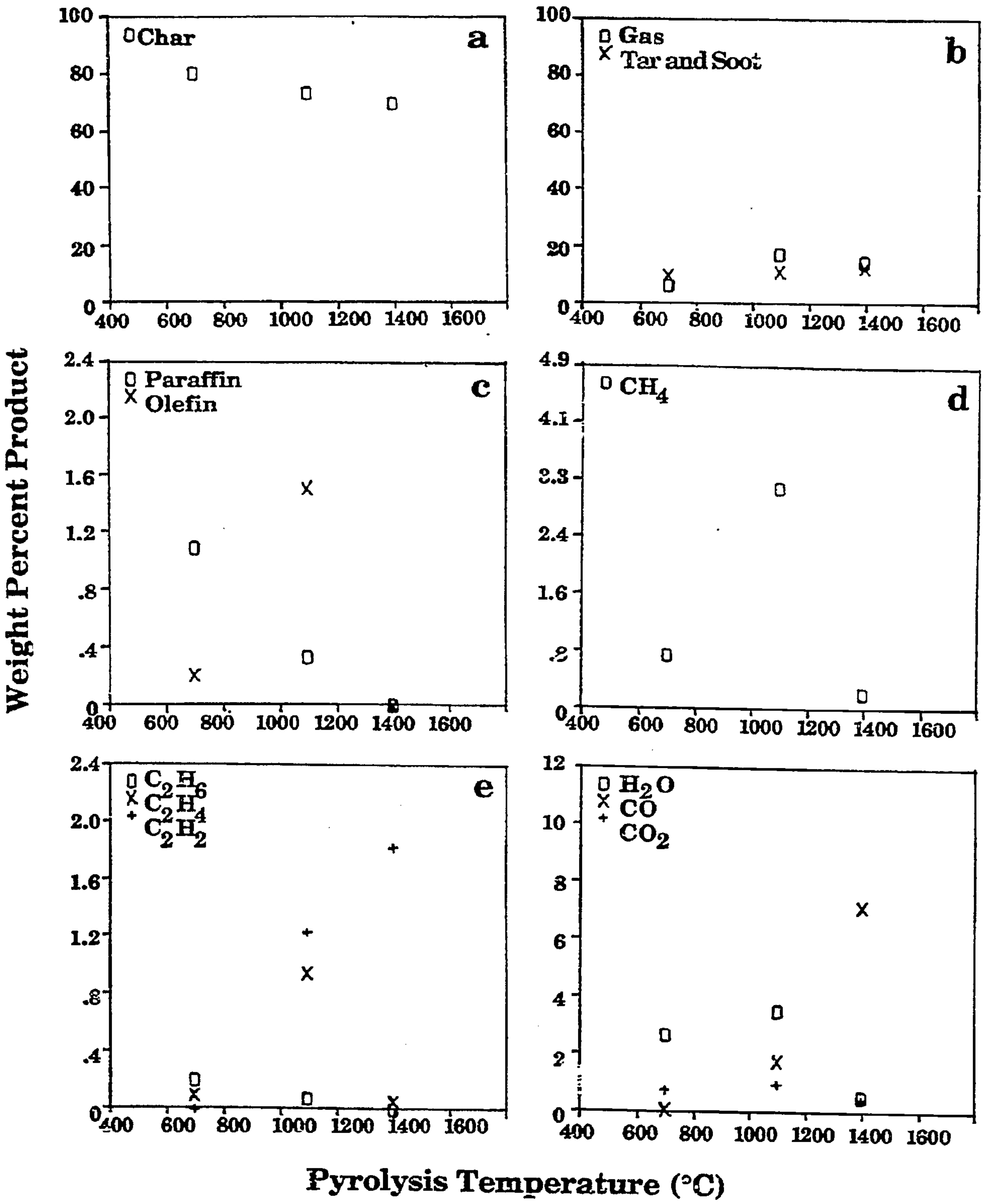

Figure II.A-26. Pyrolysis Results for Pocahontas Bituminous Coal, 200 x 325 Mesh, in the Entrained Flow Reactor at a Reaction Distance of 24". The Coal was Fed at Rates of 1 1/2 - 2 g/min with an N_2 Carrier Particle Residence Time was Approximately 0.66 Seconds.

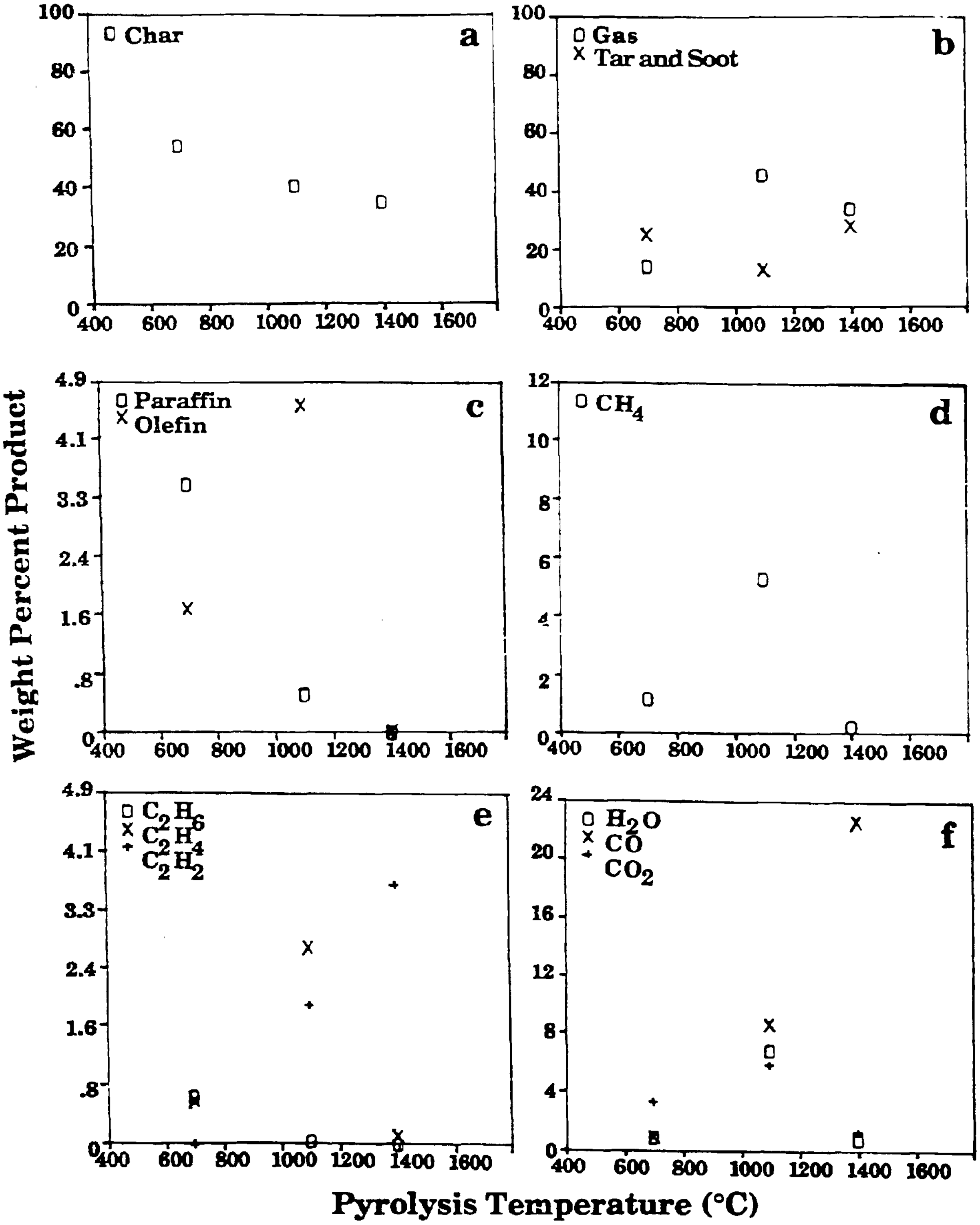

Figure II.A-27. Pyrolysis Results for Utah Blind Canyon Bituminous Coal, 200 x 325 Mesh, in the Entrained Flow Reactor at a Reaction Distance of 24". The Coal was Fed at Rates of 1 1/2 - 2 g/min with an N_2 Carrier Particle Residence Time was Approximately 0.66 Seconds.

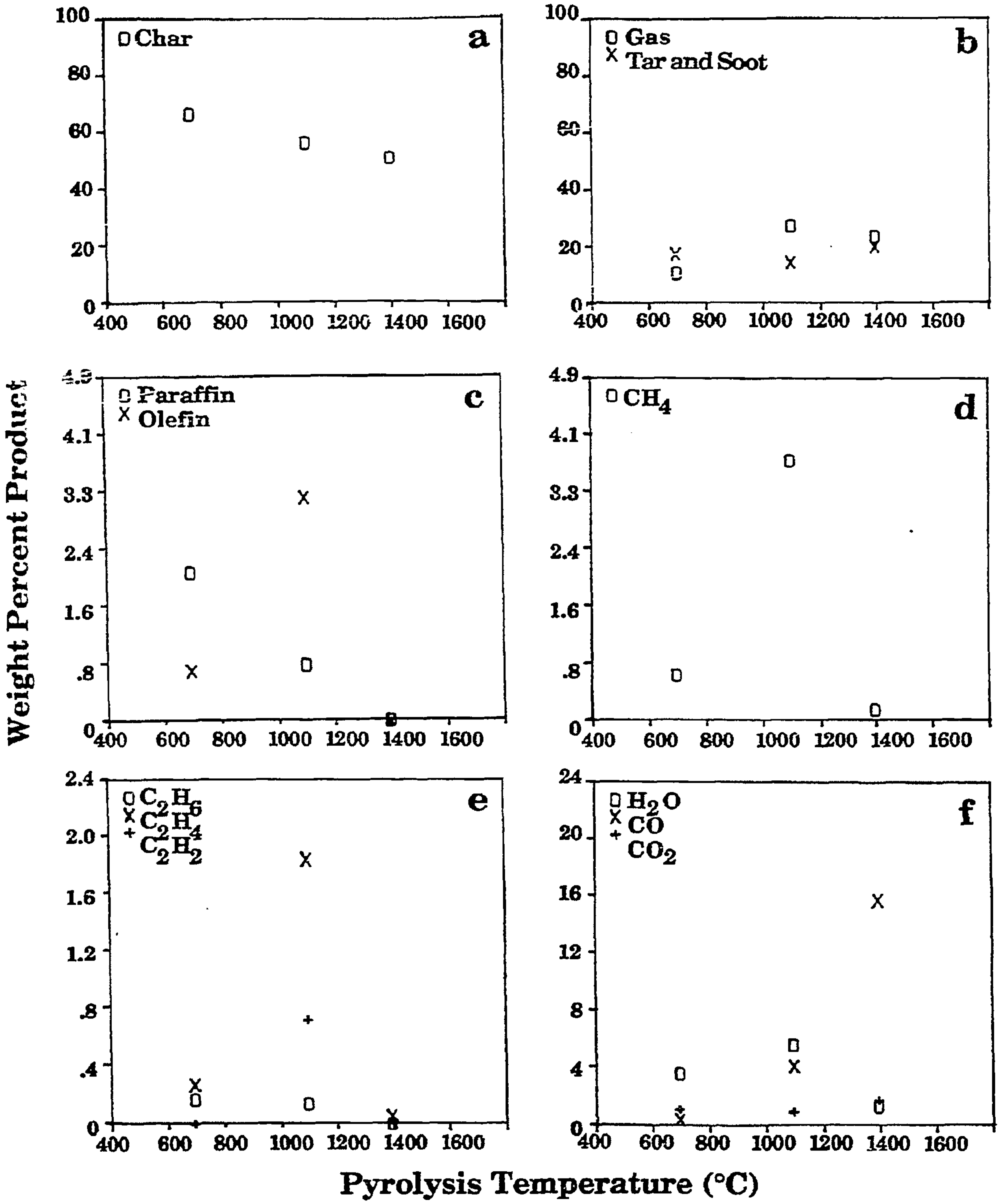

Figure II.A-28. Pyrolysis Results for Upper Knawha Bituminous Coal, 200 x 325 Mesh, in the Entrained Flow Reactor at a Reaction Distance of 24". The Coal was Fed at Rates of 1 1/2 - 2 g/min with an N_2 Carrier Particle Residence Time was Approximately 0.66 Seconds.

relatively low temperatures (Fong et al., 1986). As discussed below, it appears that the lower yields were the result of the additional transport limitations within the particle.

The original model considers external transport from the particle surface to the bulk gas is by vaporization and diffusion through a gas boundary layer. The model of Unger and Suuberg (1981) was originally employed. The modified expression for the vaporization law of Suuberg et al. (1985) is now used to replace that in the original model. The rate of evolution per gram of coal $(dn_j/dt)_{ET}$ of oligomers of molecular weight M_j is given by

$$(dn_j/dt)_{ET} = (3/r_0^3 \rho) r D_j \chi_j \, (P_j^s/RT) \qquad \text{(II.A-1)}$$

where r is the particle radius and r_0 is the initial partial radius, ρ is the particle density, χ_j is the mole fraction of species of molecular weight M_j in the metaplast, P_j^s is the vapor pressure for oligomers of molecular weight M_j, D_j is the diffusivity of species of molecular weight M_j, R is the gas constant and T is the particle temperature.

For softening coals, this limitation can be: 1) the transit of bubbles containing tar from the interior of the particle to the surface: ii) the transport of tars within the liquid to the bubble; iii) the stirring action of the bubble.

In the absence of sufficient information to accurately model these processes, the assumption was made that tars are carried out of the particle in the light devolatilization products (Solomon et al., 1987a) which exit the coal via bubbles or pores. The upper limit for this process is achieved if the heavier tars are at their equilibrium vapor pressure in the light gases. Then the rate of transport is proportional to the volume of light gases evolved which in turn is inversely proportional to the pressure within the particle $P_0 + \Delta P$, where P_0 is the ambient pressure and ΔP is the average pressure difference in the particle. Then,

$$(dn_j/dt)_{IT} = P^s \chi_j \sum_{\text{light products}} (dn_i/dt)_{chem} \left[\frac{1}{P_0 + \Delta P} \right] \qquad \text{(II.A-2)}$$

where $(dn_j/dt)_{IT}$ is the internal transport rate per gram of coal for tar component j. $\sum_{\text{light products}} dn_i/dt)_{chem}$ is the rate of production per gram of coal of component i summed over all gas and tar species with molecular weight less than 300 amu. P_j^s

is the equilibrium vapor pressure for component j (given by Suuberg et al., 1985) and X_j is the mole fraction of component j in the metaplast. For the highly fluid Pittsburgh Seam bituminous coal, we have considered the upper limit to this rate where $P_0 >> \Delta P$. Then all the terms in Eq. II.A-2 can be determined by the combined FG-DVC model. ΔP is proportional to the coal's viscosity and so, will become important for less fluid coals. It is also important when P_0 is small.

The effective rate for tar transport $(dn_j/dt)_{EFF}$ is calculated by assuming that the resistances to internal and external transport occur in series,

$$1/(dn_j/dt)_{EFF} = 1/(dn_j/dt)_{IT} + 1/(dn_j/dt)_{ET} \qquad \text{(II.A-3)}$$

The model has been compared to the data of Fong et al. (1986). Figure II.A-29 compares the results of the model with and without internal transport. The dashed line in Fig. II.A-29 shows the predicted yield in the absence of internal transport limitations. The predicted ultimate yield is clearly too high. The data suggest that the low yields are not a result of unbroken bonds (which would result from a lower bond breaking rate), since the extractable yields at low temperatures are equivalent to those at the higher temperatures. The low yields thus appear to be a result of an additional transport limitation.

The solid line employs the internal transport equation (Eq. II.A-2). There is good agreement between theory and experiment for the ultimate yield with no adjustable parameters.

Improved Model Integration

Work was also done on further integrating the FG and DVC models so that the chemistry of the bridge breaking and crosslinking in the DVC model is completely consistent with the chemistry of gas formation in the FG model. Previously, the communication between the two models was restricted to: 1) the relationship of crosslinking with CO_2 and CH_4 evolution, 2) keeping track of the amount of donatable hydrogen which limits tar evolution. For example, a modification was made to correct the tar molecular weight for the loss of functional groups due to gas evolution.

Viscosity Model

A model for the coal's or char's viscosity is being developed based on the

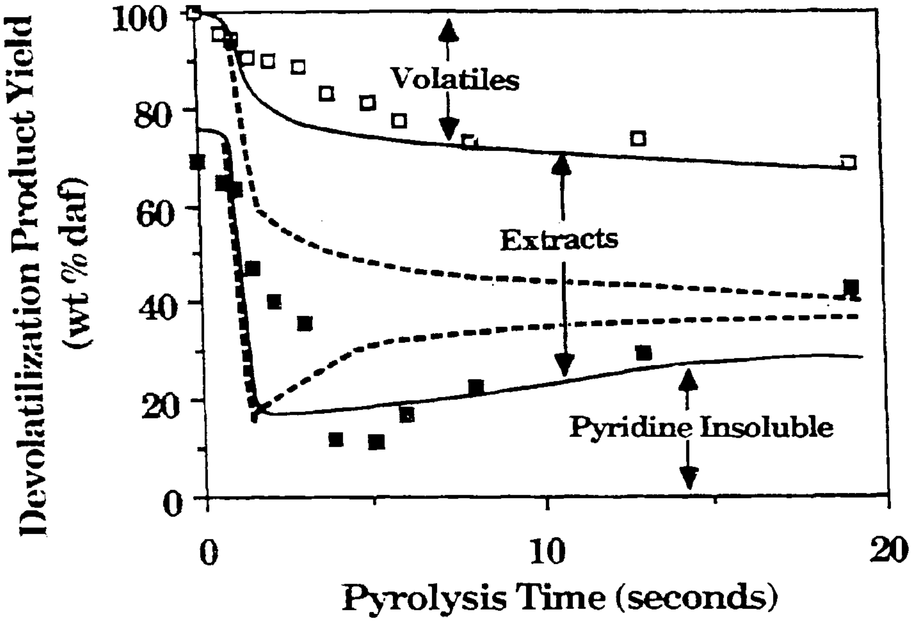

Figure II.A-29. Comparison of FG-DVC Model Predictions (lines) with the Data of Fong et al. (1986) (symbols) for Pittsburgh Seam Bituminous Coal at 813K (470 K/s). P = 0.85 atm. The Dashed Line Shows the Predicted Yield in the Absence of Internal Transport Limitations. The Solid Line Includes Internal Transport Limitations.

molecular weight distribution and functional group concentrations in the coal and char determined, in the FG/DVC model. The viscosity is important since the change in pore morphology (or swelling of the coal) is a balance between the gas evolution (which supplies the pressure to drive changes in the pore boundaries) and the viscosity (which supplies the resistance to change). The char's morphology is important in gasification since it affects mass transport of volatiles out of, and reactive gases into the particle. Swelling affects the coal's aerodynamics and radiative heat transfer processes. The chars morphology also affects its eventual fragmentation which determines the reactivity at the final phase of gasification and the ash size distribution.

High temperature coal in the fluid state can be considered as a two phase, solid-in-liquid material. The overall model that we use to predict the viscosity of the fluid employs two calculations. We first describe the viscosity of the liquid "matrix", and then use a simple relationship employing the volume fraction of the liquid to predict the fluid viscosity (the "solids" model).

Measurements - Fong (1986) has measured viscosity of bituminous coal, in-situ, during its pyrolysis in an inert atmosphere. The viscosity as a function of pyrolysis time has been reported for different time-temperature histories. The coal used was Pittsburgh Seam bituminous coal, the properties of which are given in Table II.A-12.

Fong's viscosity data are used to compare with the results of the viscosity model calculations. A problem in making this comparison is that the transport resistance calculated in the FG/DVC model is only for a single particle. In Fong's viscosity apparatus, the resistance to volatile evolution will be higher than that considered in the model. The apparatus is illustrated in Fig. II.A-30. Volatile products are released throughout the 1.93 x 1.35 cm test volume. These volatiles must transit through the bed and exit through the space around the rotating shaft in the center of the apparatus. An additional resistance must therefore, be added to Eq. II.A-3 to describe this system. In addition, the ambient pressure inside the apparatus will be higher than outside so that the P_0 in Eq. II.A-2 and in the calculation of D_j in Eq. II.A-2 must be adjusted accordingly. In the initial phase of this work, the additional resistance is treated as an adjustable factor α which multiples the resistance in Eq. II.A-3.

Model Description - Liquid Viscosity - The model developed by van Krevelen (1976) to estimate the viscosity of polymer liquid by group contribution methods

Table II.A-12.

Characteristics of Pittsburgh Seam No. 8 High Volatile Bituminous Coal

Proximate Analysis (wt%, dry basis)

Moisture$^+$	1.4
Ash	11.5
Volatile Matter	39.4
Fixed Carbon	49.1

+ as received

Ultimate Analysis (wt%, dry basis)

Carbon	68.8
Hydrogen	4.9
Nitrogen	1.3
Sulfur	5.4
Oxygen	8.2
Ash	11.5

Particle Size Range: 63-75 microns

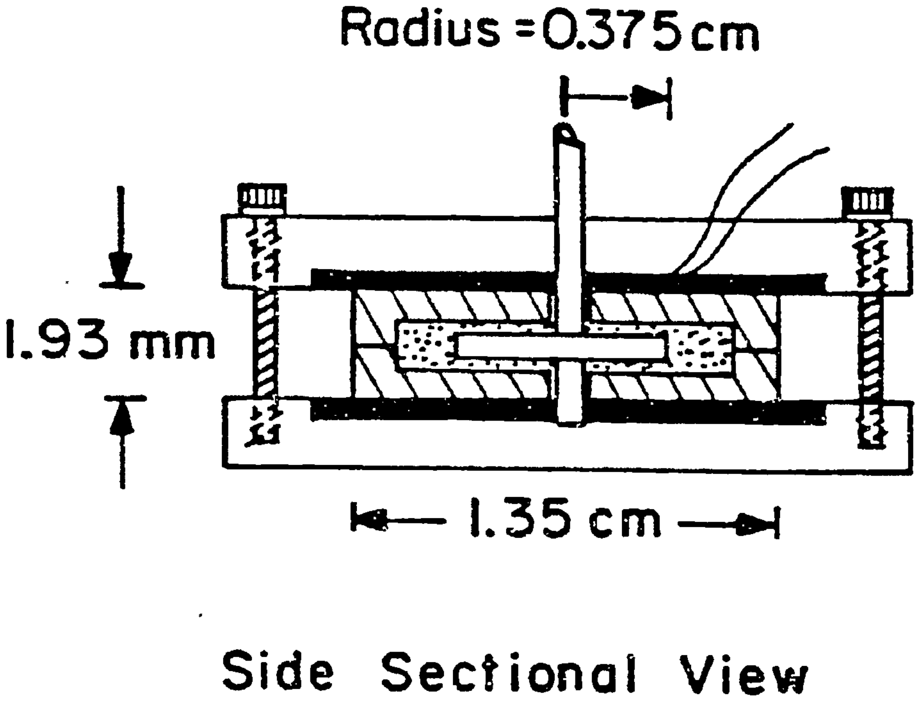

Figure II.A-30. Plastometer Hot Stage from W. Fong, Thesis 1986.

was used to describe the viscosity of the liquid component of high temperature coal melts. van Krevelen considered the factors influencing the resistance to molecules sliding past one another. These factors include: 1) the average molecular weight of the molecules, M_{avg}, 2) their functional group composition (which effects the forces between molecules), 3) the temperature (which provides the molecular motion which help overcome local energy barriers), 4) a structure parameter for the molecules, a critical molecular weight M_{cr}, which describes the weight above which molecules become entangled.

In van krevelen's model, the newtonian viscosity is dependent on the critical molecular weight (M_{cr}) of the polymer, the average molecular weight of the polymer liquid ($\bar{M}_w$) and the newtonian viscosity at the critical molecular weight (η_{cr}). The following equations from van Krevelen (1976) define the newtonian viscosity.

$$\log \eta_0 = \log \eta_{cr} + 3.4 \log (\bar{M}_w/M_{cr}) \text{ if } \bar{M}_w > M_{cr} \qquad \text{(II.A-4)}$$

$$\log \eta_0 = \log \eta_{cr} - \log (M_{cr}/\bar{M}_w) \text{ if } \bar{M}_w < M_{cr} \qquad \text{(II.A-5)}$$

$$\bar{M}_w = \sum N_i M_i^2 / \sum N_i M_i \qquad \text{(II.A-6)}$$

N_i is the number of molecules of molecular weight, M_i. $\log \eta_{cr}(T)$ is determined at any temperature from the correlation (given by van Krevelen, 1976) as a set of curves of $\eta_{cr}(T)/\eta_{cr}(1.2\ T_g)$ versus T_g/T with A as a parameter, where T_g (the glass transition temperature) and A are defined below. The set of curves are given in Fig. II.A-31. $\eta_{cr}(1.2\ T_g)$ is defined by the following equation

$$\log \eta_{cr}(1.2\ T_g) = E_\eta(\infty) \left(\frac{0.052 - 8.5 \times 10^{-5}\ T_g}{T_g} \right) - 1.4 \qquad \text{(II.A-7)}$$

A is given by:

$$A = \frac{E_\eta(\infty)}{2.3\ RT_g} \qquad \text{(II.A-8)}$$

The glass transition temperature T_g (in K) is calculated by group contribution methods,

$$T_g = \frac{\sum_i n_i Y_{gi}}{M} \qquad \text{(II.A-9)}$$

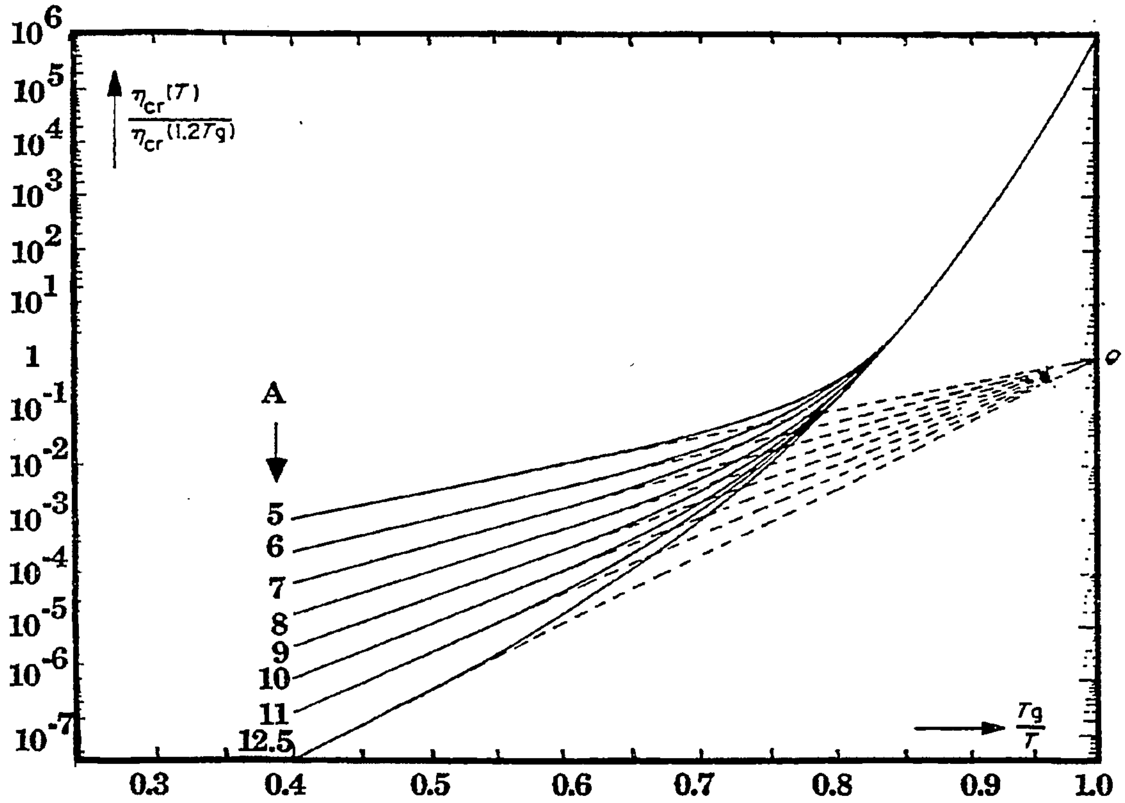

Figure II.A-31. Master Curves for η_{cr} (T) (Van Krevelen and Hoftyzer, 1976).

where Y_{gi} is the group contribution to the molar glass transition function (K ·g/mol), n_i is the number of moles of functional group i in the repeating unit and M is the molecular weight of the repeating unit.

In Eq. II.A-7, $E_\eta(\infty)$ is the activation energy for viscous flow where $T \gg T_g$, and is calculated by group contribution methods which consider a number of functional groups (van Krevelen, 1976)

$$E_\eta(\infty) = \left(\frac{H_\eta}{M}\right)^3 \qquad \text{(II.A-10)}$$

$$H_\eta = \sum_i n_i H_{\eta i} \qquad \text{(II.A-11)}$$

$H_{\eta i}$ is the group contribution to the molar viscosity temperature function ($g \cdot J^{1/3} mol^{-4/3}$) and R is the gas constant (J/ mole/K).

The critical molecular weight of the polymer is defined as

$$M_{cr} = 169/(K_\theta)^2 \qquad \text{(II.A-12)}$$

K_θ is the unperturbed viscosity coefficient and is given by

$$K_\theta = K^2/M^2 \qquad \text{(II.A-13)}$$

K is the molar limiting viscosity number function and is defined as

$$K = \sum n_i K_i + 4.2\ Z \qquad \text{(II.A-14)}$$

where K_i are contributions of specific functional groups to the molar limiting viscosity number function and Z is the number of backbone atoms per structural unit (van Krevelen, 1976).

It can be seen that the liquid viscosity model requires as input the functional group make-up, and the average molecular weight of the liquid, as well as the temperature. AFR's FG/DVC model is used to supply the necessary parameters, as described below.

Modifications to Viscosity Model for Coal - The Pittsburgh Seam No. 8 coal has been used for a variety of pyrolysis studies at AFR and the functional group composition and the various parameters needed for the combined FG/DVC model have been determined by modeling the experimental data published by Fong (1986) and various other investigators. The details can be found in the most recent publication on the combined FG/DVC model, entitled "A General Model of Coal Devolatilization" by Solomon et al. (1987) (Appendix A).

The functional group composition and the structure parameters of the FG/DVC model were used to determine the parameters of the viscosity model. The model as presented by van Krevelen gave excellent agreement with the experimental results for the "leading edge" of the viscosity versus time curves. This is the temperature at which the viscosity drops in response to the bond breaking process. It did not do so well in predicting the value of the viscosity minimum, or the subsequent resolidification. Part of this disagreement is in the difference between the transport resistance in the model and that appropriate for the measurements. The measurements have added transport resistance in the bed and an unknown pressure, which increases due to a constriction limiting the flux of evolved gas from the sample chamber. Part of the difficulty could also lie in the viscosity model, as it was not designed to take into account the effect of crosslinking which occurs in the repolymerization of the melt. It is possible that the FG/DVC model, also, gave rise to a part of the discrepancy.

A number of modifications to the model and parameters have been made initially to fit the data. These are expected to change as additional data is considered and more experience is gained. The initial set of parameters used, as well as the final optimized parameters, are given in Table II.A-13. The following assumptions or modifications made to van Krevelen's model were employed in the final version of our model.

The first assumption is the definition of the liquid fraction in the liquid solid mixture. We assume coal liquid is formed of oligomers of molecular weight less than 3000. This cut off on molecular weight has been used to define the pyridine extractable material in the model, and it describes the formation and destruction of pyridine extractables very well when compared to the experimental data reported by Fong (1986). The pyridine extractable material is believed to form the coal liquid during coal pyrolysis (Oh, 1985). This limit is expected to be temperature dependent, a property not yet included in the model.

A modification was made to the temperature dependence of the viscosity (Fig. II.A-31). The reason for this is that the experimental viscosity data

Table II.A-13. Parameters of Viscocity Model

Independent Parameter	Initial*	Final
$E_\eta(\infty)$ J/mole	40981	58000
T_g, °K	314.9	314.9
M_{cr}, g/mole	2219	2000

*calculated from the functional group composition and structural parameters of FG-DVC model

Calculated Parameters**	Initial	Final
$\log \eta_{cr}(1.2\,T_g)$	1.8839	9.3613
A	6.82	9.6483

** they are calculated from the independent parameters reported by Fong (1986) showed that the viscosity went through the same value of minimum viscosity when heated at 450 K/s to final temperatures of 826 K, 874 K, 936 K, and 1032 K. The initial drop in viscosity to its minimum also traced the same curve. This suggests that there exists a maximum temperature T_{max}, above which the viscosity is temperature independent. This temperature has to be below 826 K. A value of 773 K (500°C) for T_{max} (below which Fig. II.A-31 applies and above which $\eta_{cr}(T) = \eta_{cr}(773)$) was found to describe this type of behavior of viscosity. There is justification for this modification of the model. The correlation of van Krevelen was obtained under conditions in which the molecules are stable (i.e., they do not pyrolyze). Under conditions similar to those used here, values of activation energy for the temperature dependence of viscosity have been reported for carbonaceous pitch by Nazem (1980) and for H-coal liquids by Chao (1979). Both investigators found that the activation energy concept was valid in a very narrow region at low temperatures. As the temperature increases, the activation energy decreases. Oh, (1985) in her model of liquid viscosity, has employed a temperature dependence of the melt viscosity only at low temperatures (< 723 K) to explain melting of pre-existing metaplast.

A second modification was made to change the molecular weight dependence of viscosity (Eqs. II.A-4 and II.A-5). The weight average molecular weight of extractables decreases as the bond breaking progresses during pyrolysis. This decreases the viscosity of the coal liquid, as observed. When the crosslinking reactions take place, the high molecular weight oligomers are crosslinked with a higher probability, as they have more crosslink sites. The effect of this on the model, when the liquid cut off is at 3000 AMU is to reduce the amount of coal liquid (extractables) and to reduce the average molecular weight of the coal liquid. In reality, the liquid cut off should increase with temperature. The molecular weight dependence of the viscosity of the coal liquid is very sensitive to the molecular weight and hence this artifact of the model causes the viscosity to decrease with increasing crosslinking under certain conditions of pyrolysis. The experimental data does not show this kind of behavior. Hence a minimum in the weighted average molecular weight of the coal liquid was used. The value chosen was 1000 gm/gmole. Any reduction in the weighted average molecular weight below this value was due to an artifact of the model, and was not used to calculate the molecular weight dependency of viscosity. This modification may not be necessary if a temperature dependent liquid cutoff is employed.

A third modification is that the value of $E_{\eta}(\infty)$ (Eq. II.A-10) was employed as an adjustable parameter.

Solids Model - As described above, van Krevelen (1976) has given a procedure to estimate the viscosity of polymer liquids from their chemical composition and structures. Fong (1986) has measured the viscosity of a bituminous coal during its pyrolysis. The measured viscosity is for a solid/liquid mixture with some gas pockets. Hence a solids model is needed to predict the melt viscosity. The viscosity of a solid/liquid mixture that we use here is defined as

$$\mu_{mix} = \mu_L * f(\phi) \qquad (II.A-15)$$

where μ_{mix} is the viscosity of solid/liquid mixture, μ_L is the liquid viscosity and $f(\phi)$ is a function defining the solids concentration dependence on viscosity (relative fluidity) and ϕ is the liquid content of the mixture (volume fraction). Frankel and Acrivos (1967) have proposed an equation which is valid where the concentration of solids in the mixture is high as expected for coal. Their asymptotic solution ($\phi \rightarrow 0$) for $f(\phi)$ is

$$f(\phi) = 1/\phi \qquad (II.A-16)$$

This was used in the model that describes the viscosity of the coal melt mixture. Weight fraction instead of volume fraction was used due to absence of density data.

A summary comparing van Krevelen's model with AFR's modified model is presented in Table II.C-14.

Model Results - A comparison of the results of the viscosity model (solid curve) with the experimental data (dotted lines) measured by Fong (1986) is shown in Figs. II.A-32 to II.A-34. In Fig. II.A-32a-c, the data and model results are given where coal is heated at constant heating rates of 75 160 and 450 K/s^{-1}, respectively. The model predictions are presented for $\alpha = 1$ and $\alpha = 5$. The model with $\alpha = 1$ predicts the temperature at which the viscosity starts decreasing and the minimum value of viscosity reasonably well. These data were used to choose a value of $E_\eta(\infty)$ = 58000 J/mole (see Table II.A-13).

In Fig. II.A-33a-d, the data and model results are given where coal is heated at constant heating rate of 450 K/s^{-1} to different final temperatures. The final temperature is kept constant once it is reached. The model predicts the initial drop in viscosity to the minimum value reasonably well. The rise in viscosity due to crosslinking is not predicted very well at low temperatures. The same problem

Table II.A-14. Viscosity Model.

Variable	van Krevelen (polymer melt)	AFR two phase, coal melt
M_{AV}	$\log \eta_o = \log \eta_{cr} + 3.4 \log (M_{AV} / M_{cr})$. $M_{cr} < M_{AV}$ $\log \eta_o = \log \eta_{cr} - \log (M_{cr} / M_{AV})$. $M_{cr} > M_{AV}$	
Functional Group (FG)	$E_\eta = f_E$ (F.G., T) $A^\eta = f_A (E_\eta)$ Tg, glass transition temperature	E_η A is fixed Tg
Temperature	Semi empirical "master" curves	$A \exp (E_\eta / RT)$ $T \leq T$ $A \exp (E_\eta / RT \max)$ $T > T \max$
Structure	M_{cr}	M_{cr}
Two Phase	No	$\eta_{sl} = \frac{\eta_1}{\phi_1}$

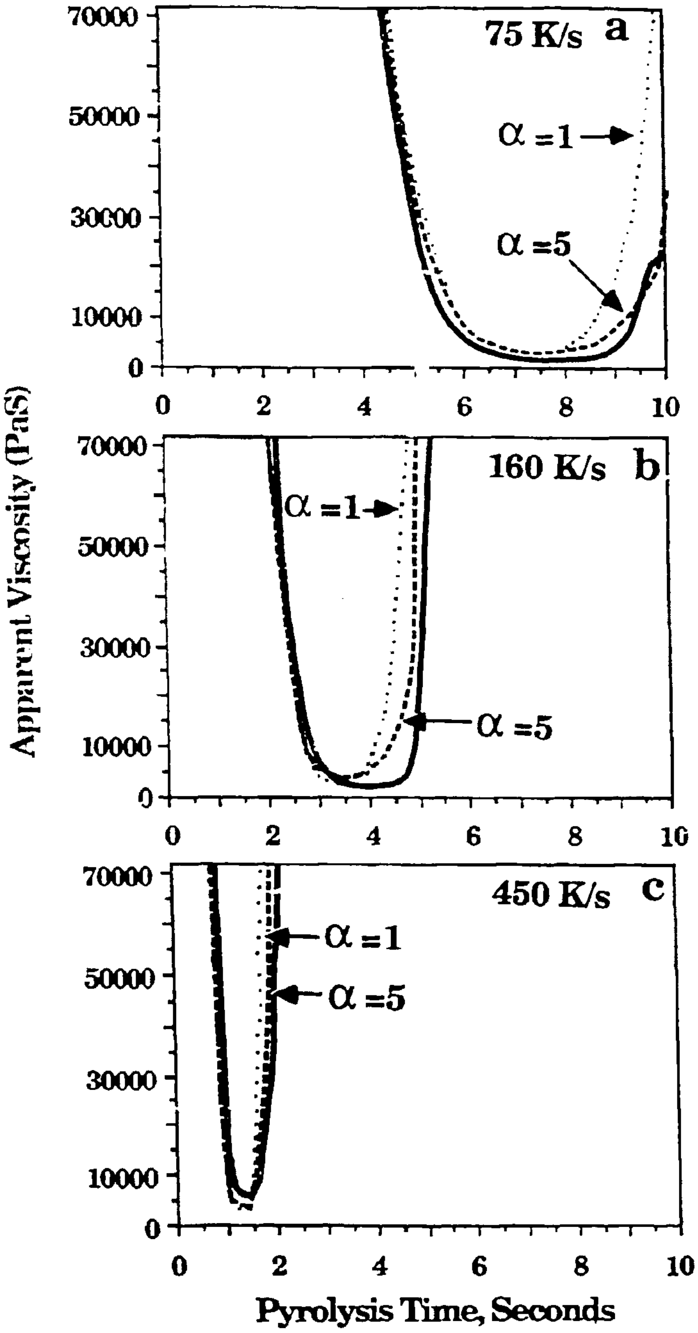

Figure II.A-32. Viscosity vs. Time for Pyrolysis at Constant Heating Rates.

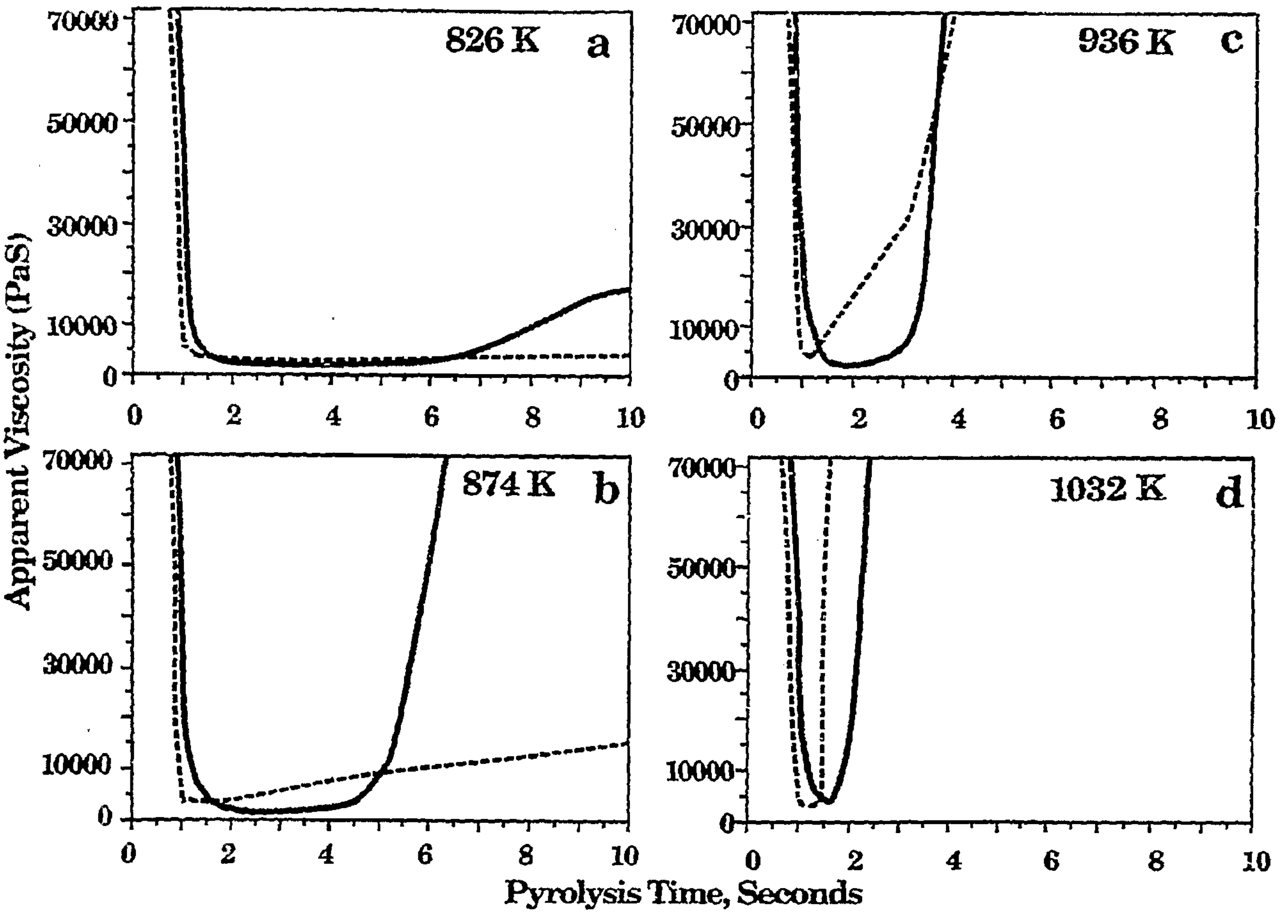

Figure IIA-33. Viscosity as a Function of Time for Pyrolysis at 450 K/sec to a Constant Temperature.

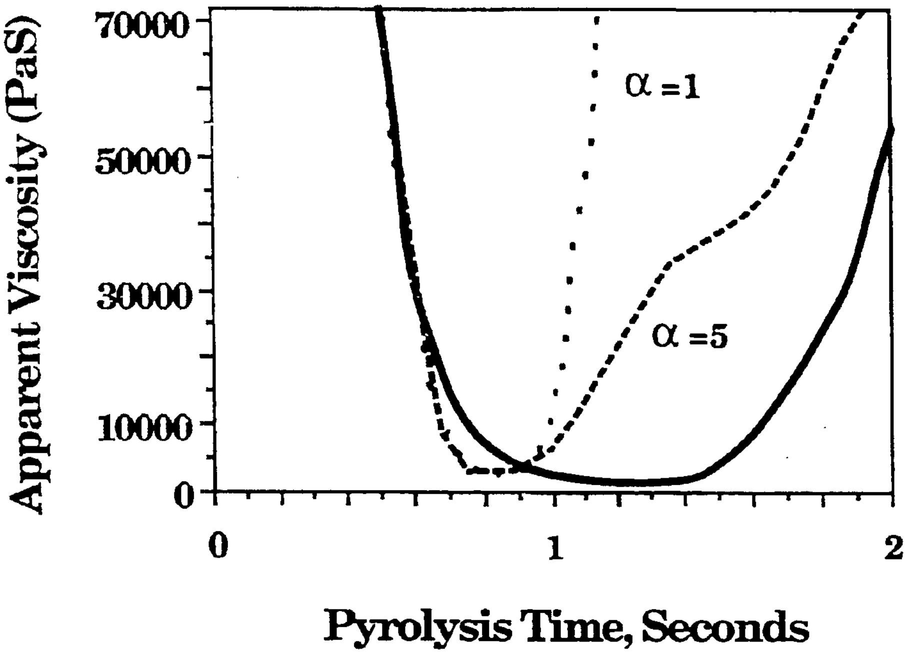

Figure II.A-34. Viscosity as a Function of Time for Pyrolysis at 664 K/sec to 1030 K.

occurs with the extract yields at low temperatures (see Appendix A), and is under investigation.

In Fig. II.A-34, the data and model results are given where coal is heated at 664 K/s to 1030 K after which the temperature is kept constant. The model results (solid curves) are shown for $\alpha = 1$ and $\alpha = 5$. From the model results, it can be seen that the plastic period is increased by increasing the value of α, but the curve describing the rise in viscosity with crosslinking slopes less steeply. The experimental data show a large plastic period but also a steep slope of rise of viscosity with crosslinking. This is an aspect of the experimental apparatus used by Fong to measure viscosity which the current model is not able to describe effectively using a high value of α. Further investigation in this regard is in progress where pressure in the Fong's apparatus is modeled as follows: 1) pressure rises due to volatile evolution from the coal; 2) pressure drops due to escape of volatiles from the experimental chamber through the gaps between the rotating shaft and its bearing. The results of this investigation will be reported in a subsequent report.

The combined model was brought up on our new SUN 3/50 and 3/260 workstations. In addition, software was developed for simultaneously presenting various outputs of the model in the different "windows" of the workstation.

Emissivity

In gasification, the determination of spectral emittance is important for two reasons. First, knowledge of the spectral emittance is necessary for the measurement of particle temperatures. Second, the spectral emittance or the emissivity (the average emittance over wavelength) must be known to calculate the rate of particle heat up, and the power radiated by the particle during combustion.

We have recently developed a new method for on-line, in-situ monitoring of particle streams to determine their spectral emittance, chemical composition, size, and temperature (Best, et al., 1986, Solomon, et al., 1985, Best et al., 1984, Solomon et al., 1986a, 1986b, 1986c and 1987b). The technique uses a Fourier Transform Infrared (FT-IR) spectrometer to perform both emission and transmission (E/T) spectroscopy for a stream of gas suspended particles.

The technique has been applied to measure spectral emittance of coal. Measurements on a variety of samples show that coal of pulverized particle size is not gray, having values of emittance near 0.9 for some regions of the spectrum, but values substantially less than 0.9 in many regions. The spectral emittance is dependent on rank, particle size, and the extent of pyrolysis, approaching a gray-body for chars, anthracite, and large particles. Recent measurements (Solomon, et al., 1987b) show that pulverized coal particles of the size used in entrained gasification undergo a transition from highly non-gray coal to highly gray char ($\epsilon = 0.9$), and finally to moderately gray char ($\epsilon = 0.7$ to 0.8). An example of the non-gray to gray transition is illustrated in Fig. II.A-35 which shows the radiance per unit surface area from char particles. Here a gray body with $\epsilon = 0.9$ would emit at the theoretical lines marked BB (883), etc. The char is least gray at low temperatures, but increases in grayness as the temperature (and exposure time) increases.

To provide understanding of this process and to develop a predictive theory for the emissivity as a function of particle size, rank and extent of pyrolysis, a theoretical analysis has been performed of emissivity during the coal to char transformation. Emissivities were calculated using the frequency dependent complex index of refraction, $m_\upsilon = n_\upsilon - ik_\upsilon$, from the standard equations of electromagnetic theory. For spherical particles these calculations can be performed using Mie theory (Bohren and Huffman, 1983).

The property of coal which determines its non-gray behavior and its variations with rank is primarily the imaginary part of the index of refraction, k_υ. As discussed in (Solomon et al., 1986b, 1986d, Solomon et al., 1987b), n_υ and k_υ can be determined from the infrared spectra of coal and chars prepared in both KBr and CSI pellets. In Fig. II.A-36 are KBr pellet spectra recorded for chars of a Zap North Dakota lignite in differing states of pyrolysis, formed in the heated tube reactor (Best et al., 1986) at an asymptotic tube temperature of 800°C. The 1200-1600 cm^{-1} region is one in which scattering is small in the pellet spectra, so the absorption coefficient can be accurately determined from these data. At higher frequencies (wavenumbers) the determination is less accurate when only KBr pellet spectra are employed, and in this case only provide rough estimates of k.

In Fig. II.A-37 we have plotted (open circles) an average value of k in the 1200 to 1600 cm^{-1} region measured from the char spectra (Fig. II.A-36), as a function of distance, D, traveled in the tube reactor. Here, the extent of pyrolysis increases monotonically with increase in D. Also plotted is the value for k at 2000 wavenumbers (closed circle in Fig. II.A-37a) and k at the absorbance minimum near 1500 cm^{-1} (squares).

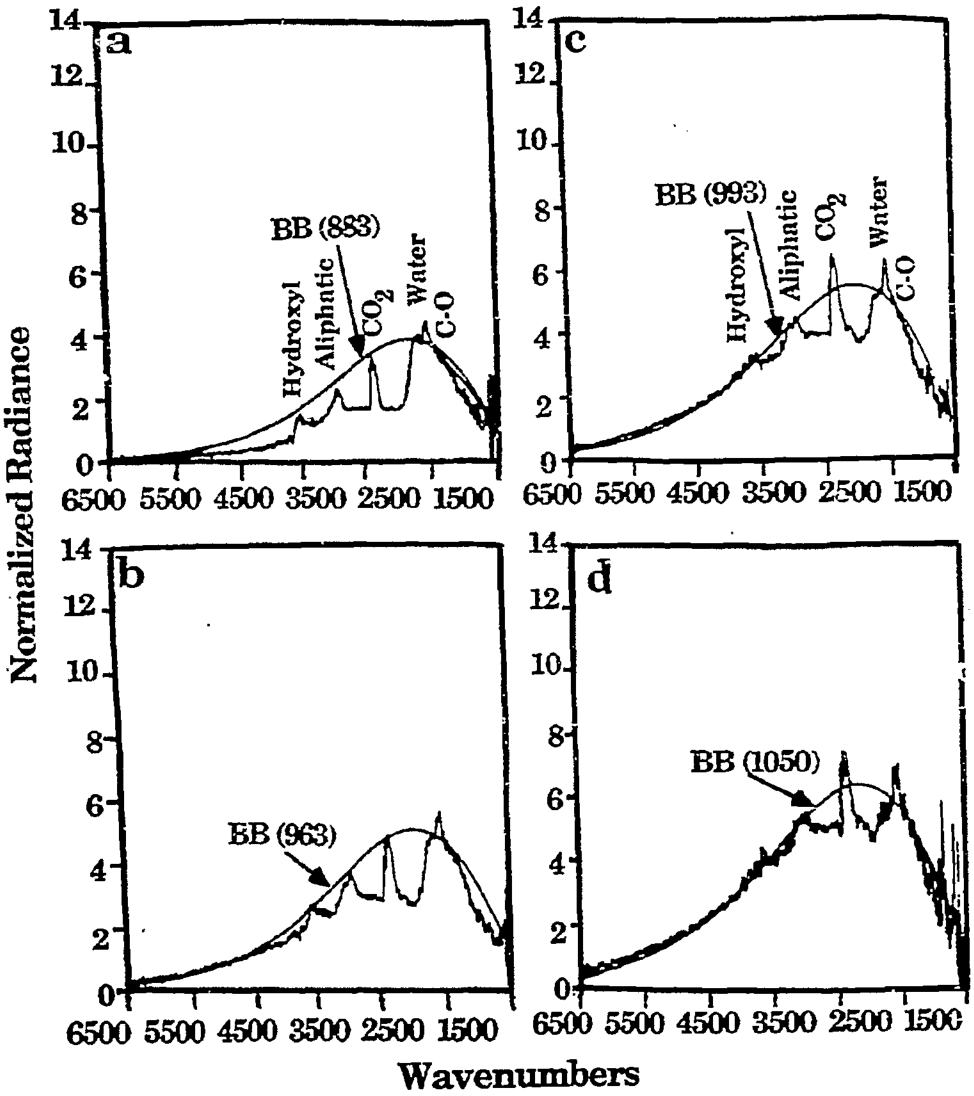

Figure II.A-35. Comparison of Normalized Radiance with Theoretical Grey-body Curves ($\varepsilon = 0.9$) for Chars at Increasing Extents of Pyrolysis (200x325 mesh).

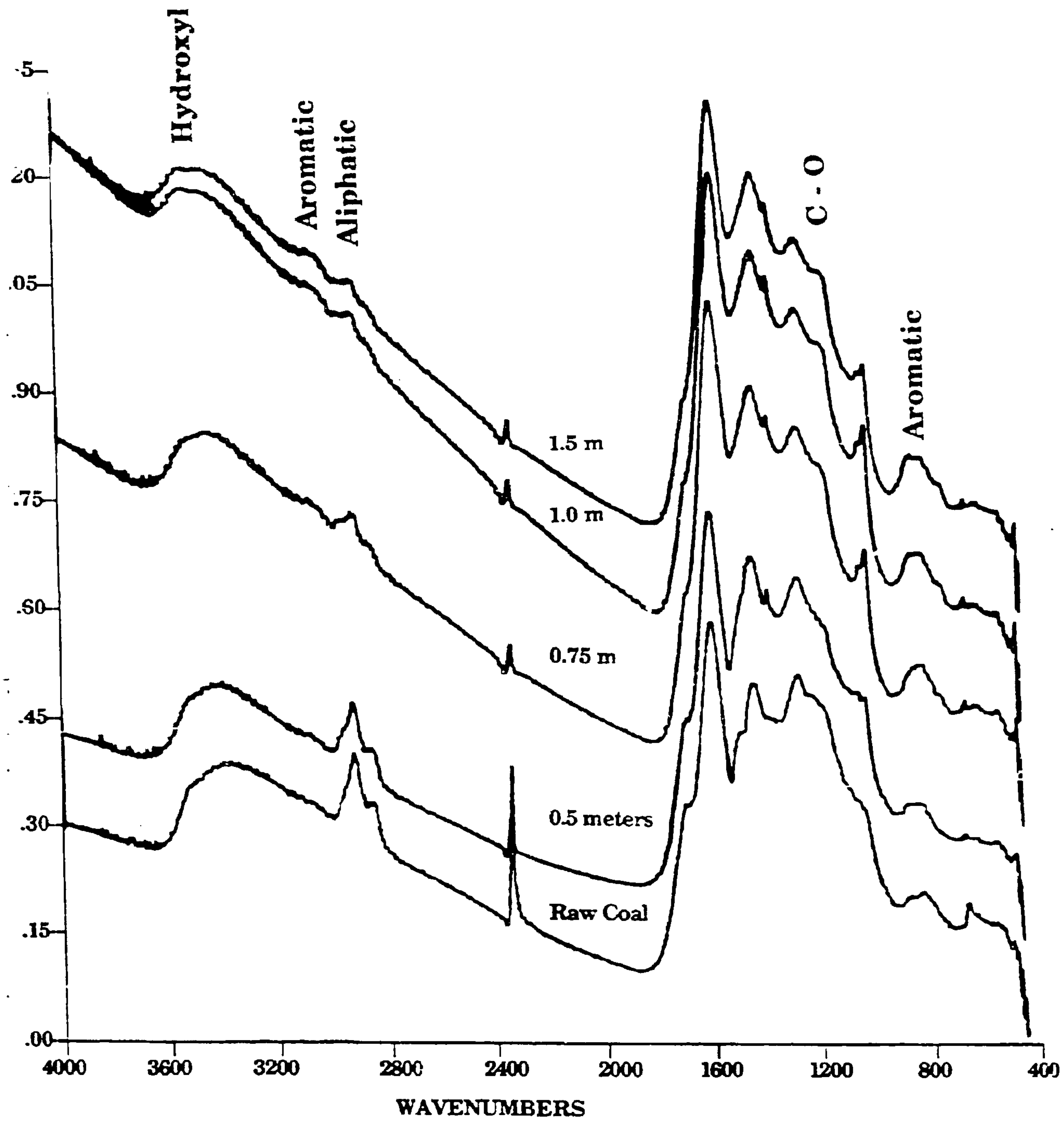

Figure II.A-36. Absorbance Spectra of Coal and Char in KBr-Pellets, as a Function of Distance in the Furnace at 800°C.

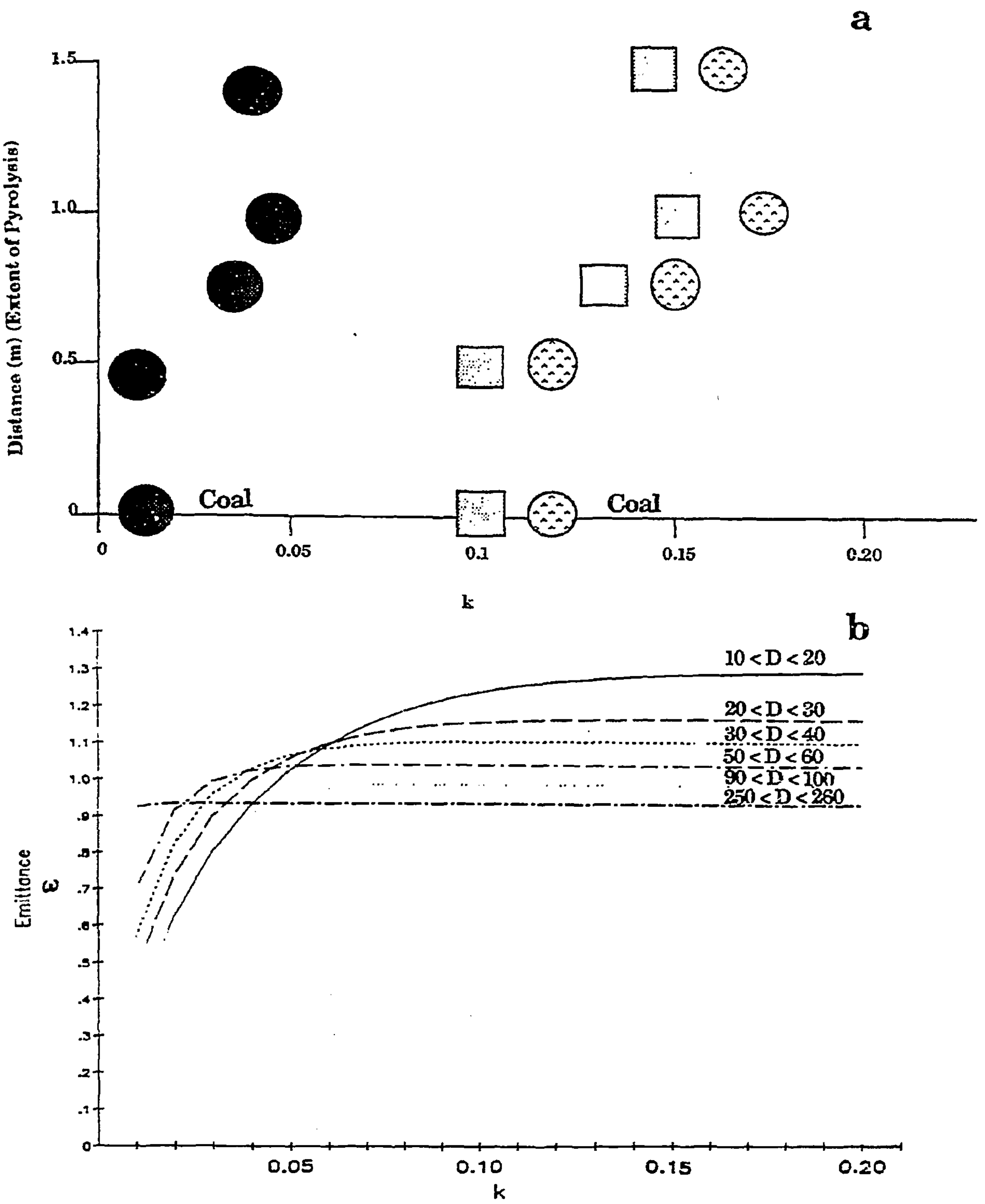

Figure II.A-37. a) Average Value of k in the 1200 to 1600 cm^{-1} Region Measured from the Char Spectra of Figure II.A-36, as a Function of Distance Traveled in the Tube Reactor (open circles): Value of k at the Absorbance Minimum Between 1200 and 1600 cm^{-1} (squares): k for the Raw Lignite at 2000 cm^{-1} (closed circles): b) Calculated Emittance as a Function of k, for Spheres of Various Diameters, with n = 1.6.

Taking a constant value of 1.6 for the real part of the index of refraction, n, we have used the Mie Theory program (Bohren and Huffman, 1983) to calculate the emittance of particles of different size, and different k values (Fig. II.A-37b).

Using Figs. II.A-37a and II.A-37b it can be seen that for all states of pyrolysis, the value of k determined for the chars in the region between 1200 and 1600 cm^{-1} are such that the value of the emittance, ϵ_ν, is constant and is within 10% of 1.05 for particle diameter, d, greater than 20 μm. The actual value depends slightly on particle size, but is practically independent of pyrolysis state. This is the region which has been used for temperature measurements.

At 2000 cm^{-1} the values of ϵ_ν for coals are particle size dependent and significantly less than unity for small particle sizes. As can be seen in Fig. II.A-37b, any increase in k with extent of pyrolysis will affect ϵ_ν at 2000 cm^{-1}. The estimated values of k at 2000 cm^{-1} for the chars of Fig. II.A-36 suggest that ϵ_ν for a 50 micron particle increases from 0.6 - 0.7 to a value of 1.0 during pyrolysis. This is in reasonable agreement with the observed emittance in Fig. II.A-35 which are for comparable conditions to those for which the chars were obtained.

There is a stage in pyrolysis beyond which ϵ_ν in the 1200 to 1600 cm^{-1} region starts to vary. This occurs when the coal starts to graphitize and both the real and imaginary parts of the complex index of refraction ($m_\nu = n_\nu + ik_\nu$) start to increase. In Fig. II.A-38 we display contour plots of emittance in the n-k plane for 55 μm diameter spheres. That part of the figure which contains the n and k values appropriate to coals in the infrared region of the spectrum is shown cross-hatched, on the left hand side of the figure. The region for graphite is cross-hatched on the upper right hand side of the figure. During pyrolysis, the emittance in the 1200 to 1600 cm^{-1} region (where $k = 0.1$) drops from a value greater than 1, towards the value for graphite. In other regions of the spectrum where k 0.01, ϵ_ν first increases and then decreases as k increases i. Our experimental observations suggest that for residence time on the order of 1 sec, n and k increase significantly only above 1000°C, and it is above this temperature that ϵ_ν is observed to decrease. For a highly graphitized char ϵ_ν can be as low as 0.7.

Besides the calculation of the emissivity, the MIE theory program can be used to calculate the total extinction cross section F^t_ν. F^t_ν determines the shape of the transmittance, τ_ν

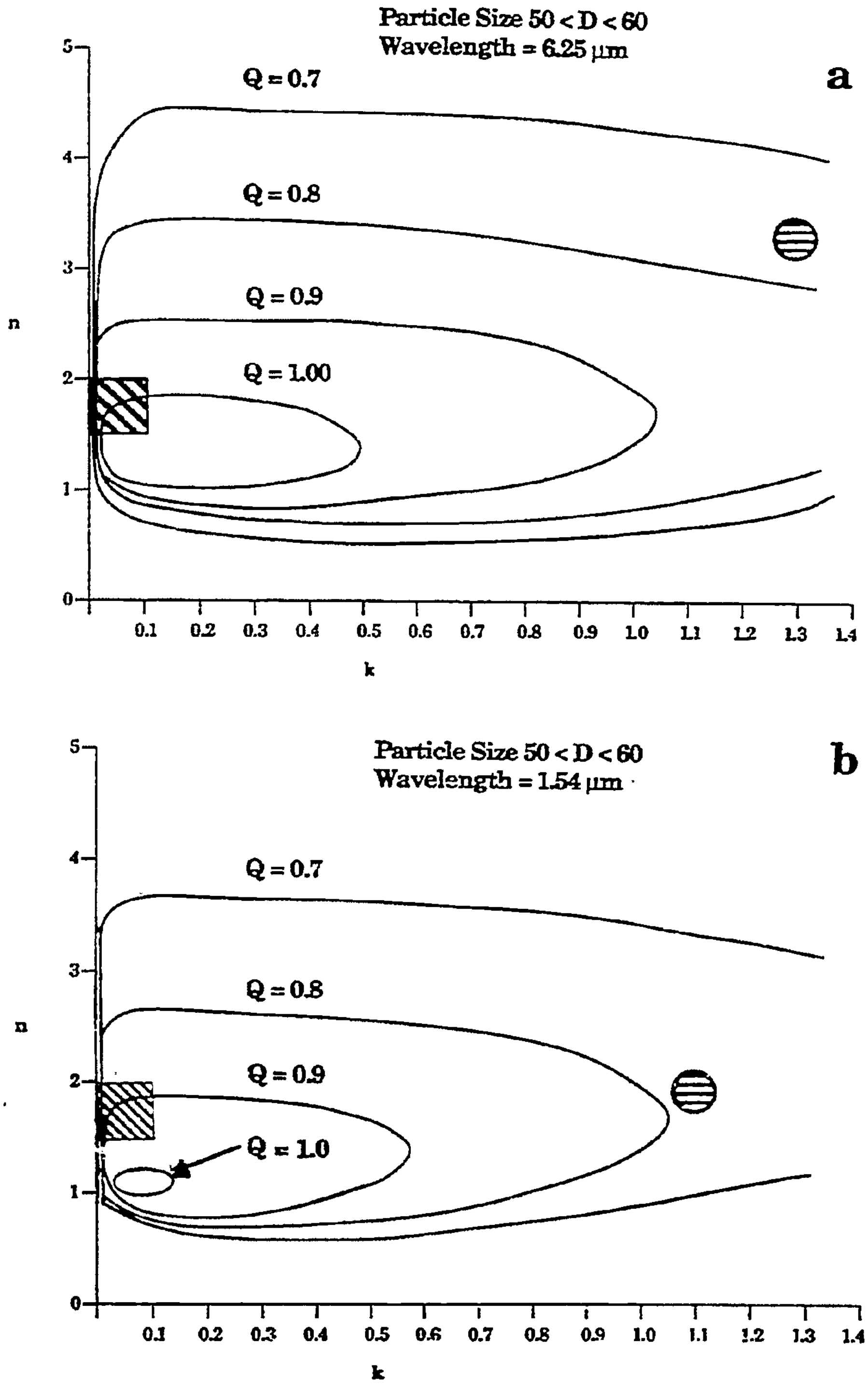

Figure II.A-38. Contour Plots of Constant Emittance, Q, Calculated by Mie Theory for Spheres of Various Values of n and k, for 55 µm Diameter Particles. The Combinations of n and k found for Coal in the Infrared are Shown Shaded on the Left Hand Side of the Diagram: Those for Graphite are Shaded on the Right (the values for graphite are taken from Foster and Howarth, Ref. 7). The Calculations are for Radiation of two Wavelengths, as Shown.

$$\tau_{\upsilon} = \exp(-NA\ F^t_{\upsilon}L)$$

where N, A and L are the particle number density, particle area and path length through the particle stream, respectively.

Some calculations of F^t_{υ} are presented in Fig. II.A-39. In Fig. II.A-39a we show calculations of F^t_{υ} for a Nicolet 7199 FT-IR, using the optical constants we have derived for a Montana subbituminous coal (Solomon et al., 1986d). The Nicolet 7199 FT-IR spectrometer, with a 4" diameter, 9.5" focal length collection mirror, has a semi-cone acceptance angle of 12° which was used for the calculations in Fig. II.A-39a. It can be seen that F^t_{υ} is a smooth function of wavenumber, even though k changes substantially across the spectrum. For swelling coals, F^t_{υ} must be measured at each temperature because it varies with particle size. Indeed, the shape of the F^t_{υ} spectrum has been made the basis for a method of particle size determination (Solomon et al., 1987b). The shape of F^t_{υ} can, however, be determined from measurement with the use of the above equation. For particles above 40 μm diameter, F^t_{υ} at 6500 cm^{-1} is relatively insensitive to size, being equal to 1.1 $\pm$ 0.10. The temperature measurement can therefore be made on swelling coals as well.

The sensitivity of the spectral shape of F^t_{υ} to particle size distribution makes the measured F^t_{υ} spectra useful monitors of the size distribution. Particle break-up, or swelling can be easily detected.

Plans

Continue characterization and pyrolysis of coals. Perform reactivity experiments on ion-exchanged coals. Improve and compare the FG/DVC model with data. Continue development of the viscosity model. Devise experiments to test internal and external mass transport submodels of combined FG/DVC model by doing experiments under pressure.

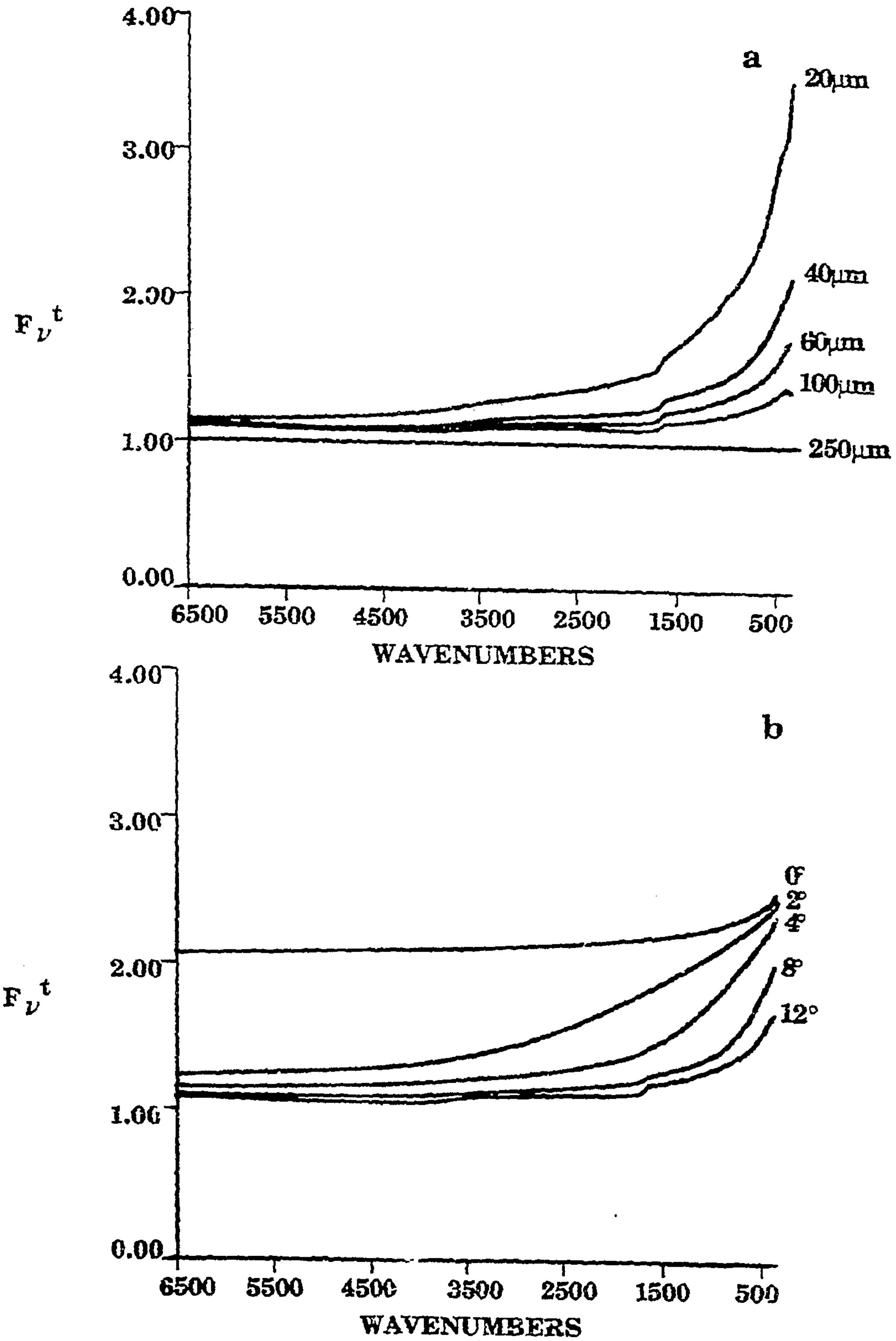

Figure II.A-39. a) Calculations of F_ν^t Spectra for Our Instrument, for Particles of Various Diameters. and having the Wavelength Dependent Optical Properties of a Montana Rosebud Subbituminous Coal (2). The Calculation for the 250 μ m Diameter Particle was done with Raleigh Large Particle Theory. b) Calculations of F_ν^t Spectra for Instruments of Differing Half-Acceptance Angles, for Particles of Mean Diameter 60 μm.

II.B. SUBTASK 2.b. -- FUNDAMENTAL HIGH-PRESSURE REACTION RATE DATA

Senior Investigators -- Geoffrey J. Germane and Angus U. Blackham

Brigham Young University
Provo, Utah 84502
(801) 378-2355 and (801) 378-6536

Objectives

The overall objectives of this subtask are 1) to measure and correlate fundamental reaction rate coefficients for pulverized coal char particles as a function of char burnout in oxygen at high temperature and 2) to provide fundamental kinetic rate measurements of sulfur species with sorbents for a range of stoichiometries under laminar, high-pressure conditions.

The specific objectives for the first-year reporting period include:

1. Organize the interdisciplinary research team.
2. Review appropriate literature in pertinent areas.
3. Survey existing high pressure reactors in preparation for the design of a high pressure reactor for this study.
4. Develop elements of the experimental test plan for the char oxidation and sulfur capture studies.
5. Design the high pressure reactor and support systems.

Accomplishments

Four components of this subtask have been identified to accomplish the objectives outlined above: 1) char preparation at high temperature and high pressure, 2) determination of the kinetics of char-oxygen reactions at high pressure, 3) design and construction of a laminar-flow high pressure reactor, and 4) measurements of fundamental sulfur capture rates by sorbents.

Component 1 -- Char Preparation at High Temperature and High Pressure

Utah bituminous coal has been selected as the first coal for study under this program because of the availability of this coal at the BYU Combustion Laboratory and its inclusion as one of the coals in the Argonne Premium Coal Sample Bank and in the PETC Coal Sample Bank. Char will be prepared by two methods: 1) utilization of the BYU high-pressure, entrained-flow gasifier at a pressure between 10 and 20 atm and above 1700 K to produce a relatively large amount of char, and 2) passing the coal through a hot ceramic tube (approximately 1 cm in diameter) at pressures between 1 and 20 atm and above 1700 K to produce small quantities of char. When the high-pressure reactor for this project is completed, it will be used to prepare char from this same coal under similar conditions. The properties of the samples obtained from these procedures will be measured to identify any significant differences, even though the temperatures and pressures of the procedures are to be nearly the same. If no significant differences are observed, then the most convenient char preparation procedure will be used for the remaining four coals. Because these chars will contain residual sulfur, some of them will also be used in the sorbent capture studies.

A trial char preparation run using Utah coal in the BYU high-pressure gasifier is planned for next quarter. The objective is to obtain sufficient char so that size fractioning will give two samples--about 500 grams of 45 mm average particle size and 500 grams of 70 mm average particle size. These particle sizes will enable comparison with char oxidation measurements at atmospheric pressure planned for a separately funded study in the BYU Combustion Laboratory. Another char preparation approach with this coal planned for the next quarter involves passing pulverized coal samples of up to ten grams through a hot ceramic tube at high- pressure and high-temperature, entrained in nitrogen. The resulting char will also be fractionated into samples of 45 and 70 mm average particle size.

Component 2 -- Kinetics of Char-Oxygen Reactions at High Pressure

Oxidation of pulverized coals and their residual chars in oxygen at elevated pressures is important in several processes of interest to METC. coal-fired gas turbines may operate at high pressure with excess oxygen. In entrained gasification there is some evidence that direct oxygen attack on residual char occurs early in the reaction process before the oxygen is consumed (Brown and Smoot, 1986). However, little work in high pressure oxygen atmospheres is reported or is in progress. Present emphasis in other METC-funded work deals with high pressure reaction of coals and chars with steam and CO_2. Low pressure data cannot necessarily be extrapolated to high pressure because of the complex interaction of intrinsic kinetics with heat and mass transport.

The proposed program schedule indicates the completion of the char oxidation studies and the sulfur/nitrogen sorbent studies for pulverized coals by October 1989 (the end of the third year). Since the focus of these studies is high-pressure, a reactor capable of functioning at 400 psi (27 atmospheres) is being constructed. For the determination of kinetic parameters, data taken at atmospheric pressure will be included. These data will be obtained with an atmospheric pressure reactor under separate funding. The three coals used for the other study are the same coals proposed in this study: a Utah bituminous coal, a North Dakota lignite, and a Wyoming subbituminous coal. Two additional coals for this study will be specified during the next year.

Literature Review -- Though many studies have been conducted to examine the kinetics of coal and char reactions for a variety of operating conditions, the majority of these have been at atmospheric pressure (Nsakala, et.al., 1978; Maloney and Jenkins, 1984; Kobayashi, et. al., 1977; Solomon, et.al., 1982; Tsai and Scaroni, 1984; Badzioch and Hawksley, 1970). The high-pressure studies available in the literature were conducted with stationary char particles; none of the tests used laminar flow furnaces. The changes in grain size and tar formation with variation in pressure, heating rate, and temperature were investigated by van Heek et al. (1984). The tests were performed using a wire mesh in a pressure chamber. Anthony et al. (1976) used a similar test facility and discovered that the volatiles yield increased significantly with decreased pressure for a bituminous coal. Tamhankar et al. (1984) and Sears et. al. (1985) used a TGA apparatus to find that higher pressures reduced the extent of pyrolysis but at higher temperatures there was less pressure dependence on char reactivity.

Char Reactivity Measurements. The experimental plan for char reactivity is based on a simple model (Smoot and Smith, 1984) of diffusion rate and surface reaction rate. The diffusion rate, rd, is given by

$$r_d = n_p k_m A_p (C_{ob} - C_{os}) \qquad \text{(II.B-1)}$$

where n_p is the number of particles, k_m is the mass transfer coefficient, A_p is the particle surface area, and C_{ob} and C_{os} are the bulk and surface concentrations of the oxidizer, respectively. The reaction rate, r_k, is given by

$$r_k = n_p k_r C_{os}^n A_p \qquad \text{(II.B-2)}$$

where n_p is the reaction order and k_r is an Arrhenius reaction rate constant, given by

$$k_r = Ae^{(-\frac{E}{RT_p})} \qquad \text{(II.B-3)}$$

where T_p is the particle temperature.

The overall reaction rate, r_o, is then expressed as

$$\frac{1}{r_o} = \frac{1}{r_d} + \frac{1}{r_k} \qquad \text{(III.B-4)}$$

The model identifies five quantities that need to be measured in order to determine reaction rates: particle size, mass, and temperature as functions of time at a given pressure and oxidizer concentration.

In situ optical measurements will provide particle temperatures, diameters, and velocities and particle mass loss will be determined from the amount of titanium in the ash. Pressure and oxidizer concentrations will be determined by the experimental conditions. Elemental and proximate analysis, N_2 BET surface area, and scanning electron micrograph measurements will characterize the composition, surface area, and porosity of the char.

Tests will be conducted with chars from five different coals, under the conditions shown in Table II.B-1, to determine, for example, the effect of pressure on the specific reaction rate constants, the char oxidation reaction order, and on diffusion.

TABLE II.B-1

TEST CONDITIONS FOR CHAR OXIDATION MEASUREMENTS

Reactor Condition	Ranges
Temperature	1300-1700 K
Pressure	1-27 atm
Residence time	20-150 ms
Particle size	45-70 mm
Gas composition	1) air 2) O_2 (5-20%, CO_2 (15-35%) H_2O (10-45%), N_2 (balance)

Component 3 -- High-Pressure Reactor Design and Fabrication

Experimental Plan

A literature review of char oxidation and sulfur capture by sorbents at high pressure was conducted to find suitable models to predict char oxidation rates and sorbent behavior, and to determine the current knowledge in both areas to assist in developing the experimental plans for the char oxidation and sulfur capture studies, which would be expected to influence some reactor design parameters.

The design of the high pressure reactor and optical instrumentation for particle temperature, size and velocity measurements is essentially complete. Specific plans for char preparation at high pressure in an entrained-flow coal gasifier have been made, and the previously proposed experiments for char preparation, char oxidation kinetics, and sorbent capture of SOx at high pressures adequately summarize the present plan.

Literature Survey -- A great deal of literature is available on atmospheric-pressure, drop-tube furnaces (Field, 1969; Badzioch and Hawksley, 1970; Nsakala, et al., 1977; Scaroni, et al., 1981; Solomon, et al., 1982; Seeker, et al., 1980; Baum and Street, 1971; Kobayashi, et al., 1977; Maloney and Jenkins, 1984) but considerably less is available for high-pressure reactors. Requests for information to those who operate high-pressure, laminar-flow reactors have been received to date from AFR (Solomon, 1985), METC (Bissett, 1985), and MIT (Bush, 1980).

The AFR reactor (high pressure) operates at up to 14 atm pressure and 1923 K. The entire reactor is enclosed in a pressure containment vessel that allows no optical access. The total gaseous effluent from a test run is collected in a tank for later analysis. The particle residence time is 5 seconds.

The METC high pressure facility also has long residence times, ranging from 2 to 10 seconds. It operates up to 60 atm pressure and 1650 K. Coal particles and preheated gases are turbulently mixed before the flow becomes laminar. The reactor is used for coal devolatilization and gasification studies.

MIT's reactor operates at 7 atm and 1273 K. No optical access is provided but the wall heaters are divided into zones in order to control the axial temperature profile. Particle residence times are less than 1 second. Although the facility is operated at only atmospheric pressure, quartz observation ports allow in situ particle velocity measurements (Kobayashi, et al., 1977).

Flaxman and Hallett (1987) have discussed the importance of the flow field through the reactor. Flow visualization studies were conducted to explore the effects of different flow straighteners, Reynolds numbers, and primary-to-secondary gas flow ratios. Maloney (1984) stressed the importance of accurate characterization of the flow field and showed that discrepancies between the results of different researchers was primarily due to poor approximations of particle residence time.

Performance Requirements -- The experimental plan requires that the reactor operate in a temperature range of 1300-1700 K and a pressure range of 1-27 atm. In order to determine accurate reaction rates, the temperature profile along the length of the reaction tube must remain isothermal. The reactor inlet is the most critical location, since incoming particles need to reach reactor temperature and oxygen concentration as rapidly as possible.

Residence times ranging from 1-1000 ms must be obtained while maintaining laminar flow. The mass flowrate of gas must be considerably greater than that of the particles to ensure that any changes in local temperature or gas composition caused by particle reactions will be insignificant. Experiments will help determine the range of flowrates necessary to achieve this. Particles will be fed into the reactor at a constant but adjustable rate of less than 0.5 g/min. The char particles will range from 20-100 μm and the sorbents are about 1 μm in diameter.

In situ measurements of temperature, particle size, and velocity necessitate optical access to the reaction tube. This access must allow two orthogonal lines of sight through the reactor in a plane perpendicular to the centerline of the tube. The optical instrumentation also requires a particle loading no greater than 0.5 g/min. Direct sampling of the reacting particle is also required. The particle must be quenched and withdrawn from the reactor just after it passes through the optical volume.

Pressure Vessel -- A flow diagram for the entire system and a diagram of the preliminary reactor vessel are shown in Figures II.B-1 and 2, respectively. Particles are fed with the primary gas through the injector, which is moveable to allow adjustment of axial particle inlet location in order to vary particle residence times. The honeycomb, ceramic flow straightener, fastened to the end of the injector, keeps the injector at the centerline of the reaction tube and ensures laminar flow of the secondary gas. The secondary gas flows into the top, where it is preheated before

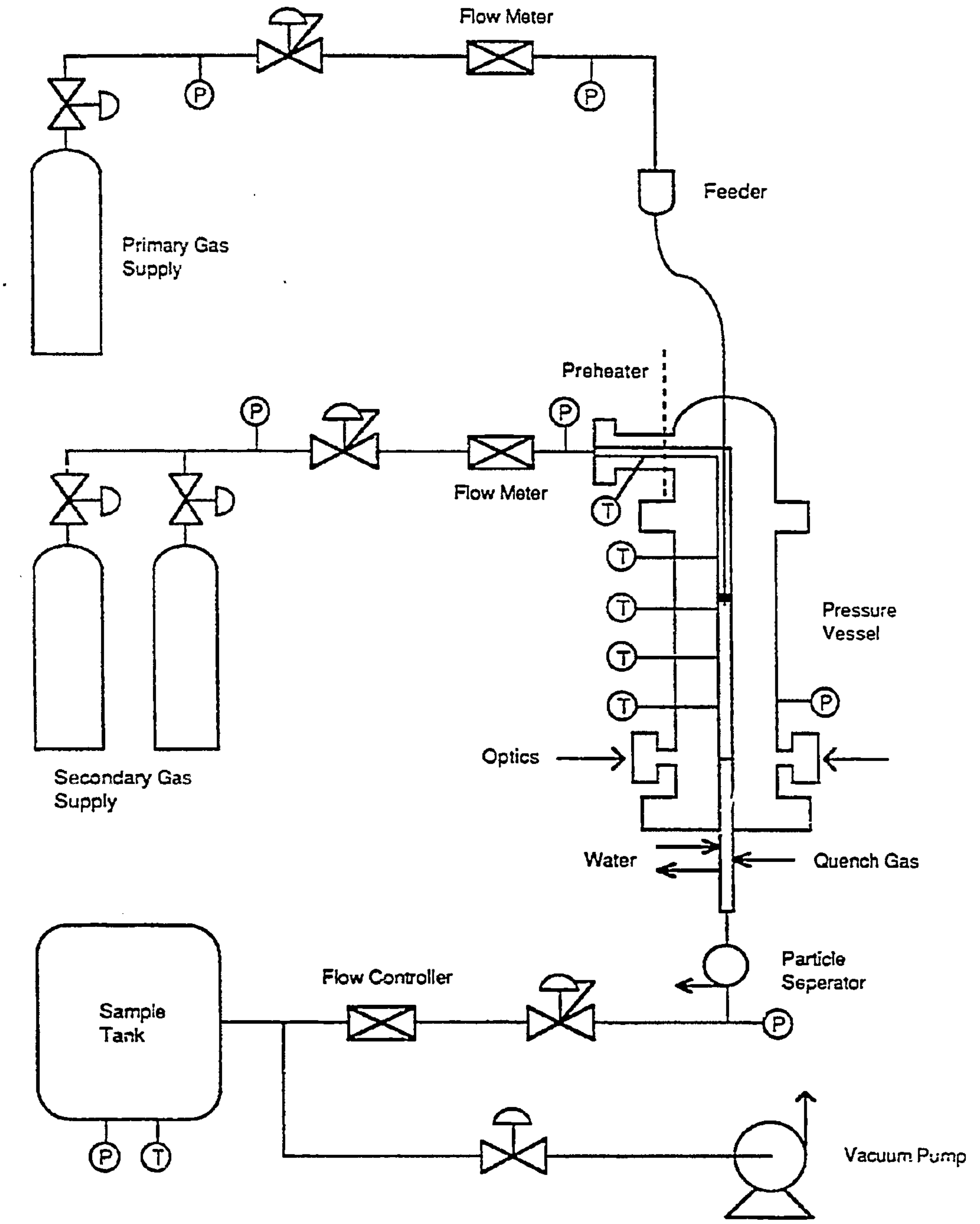

Figure II.B-1. Flow diagram.

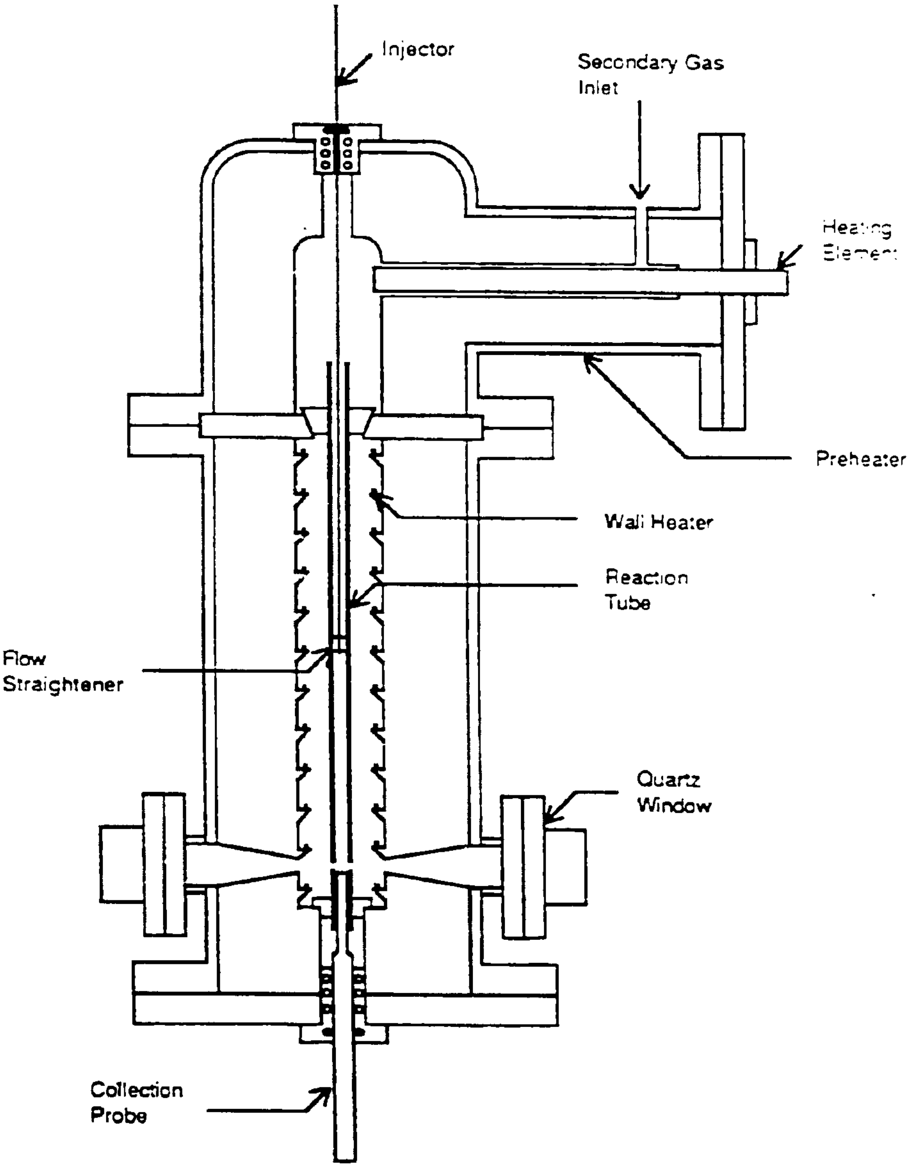

Figure II.B-2. Reactor cross section.

flowing into the reaction tube. The primary and secondary flows mix in the reaction tube, initiating the particle reaction. Wall heaters maintain an isothermal temperature profile. Holes in the reaction tube wall and quartz windows on the outer shell allow optical measurement of the particles as they flow through the diagnostic volume. The collection probe collects the entire mass flow and quenches the particle reaction directly following the optical access. The particles are then captured either in a filter or by a cyclone, while the remaining gases are collected in the sample tank.

The vessel consists of three parts: the top section that contains the preheater and injector seal; the center section that houses the reaction tube, wall heaters, and optical heaters; and the lower section that contains the collection probe seal and supports the insulation. The outer wall of the vessel is 1.3 cm thick stainless steel pipe about 30 cm in diameter, which gives a safety factor of 2 for the most severe operating conditions (27 atm pressure and 530 K wall temperature). The wall is lined with 10 cm of ceramic insulation that provides support for the wall heaters along its inner diameter. The insulation in the center section is removeable to allow insertion of the wall heaters.

A plexiglass model of the reactor was constructed to study the flow field (see Figure II.B-3). The main concern was the flow in the vicinity of the reaction tube optical holes. Experiments showed that there was significant flow through these holes at higher pressures. Similar flow in the test reactor would lead to inaccurate results. It was determined that the volume surrounding the reaction tube must be isolated from the secondary gas. A simple ceramic seal between the top and center sections forms a dead space between the reaction tube and wall heaters. This seal prevents flow of the secondary gas down past the heaters and into the reaction tube through the optical holes. Since the pressure difference between the dead space and reacting flow is small, only small forces are exerted on the reaction tube.

The reactor design allows the use of reaction tubes from 1 to 5 cm indiameter. This is necessary to achieve the wide range of times at the conditions called for in the experimental plan. The reactor can also be

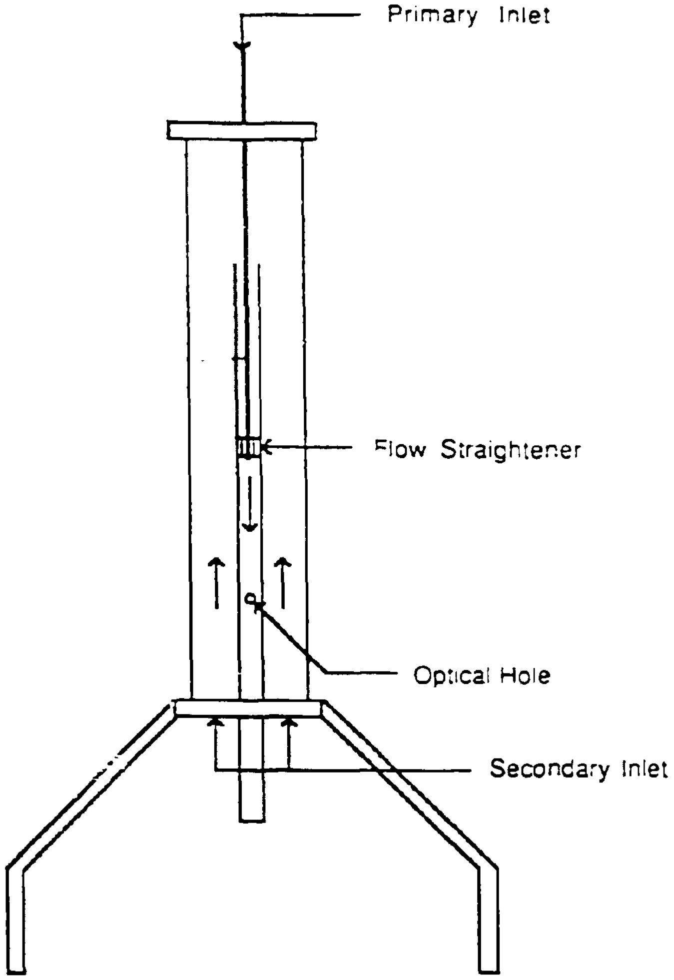

Figure II.B-3. Flow model.

lengthened to increase residence time by adding an extension section between the top and center sections and installing a longer reaction tube. The extension section is similar to the center section with wall heaters but no optical access ports. Quartz windows provide optical access through the vessel wall while containing the internal reactor pressure. The access wall and flanges are water-cooled to ensure that the quartz remains below 475 K. Both the injector and collection probe are positioned by water-cooled O-ring pressure seals in the reactor shell.

Materials -- The choice of high temperature materials is important in two areas of the reactor: the insulation and reaction tube. A standard cast mullite reaction tube will be used. It will withstand high temperatures with no reaction with the gases flowing through it, and the thermal shock of a cooled probe or injection tube. The optical access ports will be machined at Brigham Young University. A low value of thermal conductivity for high temperature insulation materials can allow the outside reactor casing to be cooled by free convection and still be cool enough so that the optical access will not be effected. The insulation also must be compatible with the electric heaters. A fibrous alumina insulation was found which has a very low thermal conductivity, and is strong and rigid enough to support the required heating elements.

Heating System -- Several types of heating systems were available that would attain the temperatures needed for this reactor. These included electric resistance heaters, induction or resistance-heated graphite, and backfired heaters. The heating system needs to provide a controllable profile along the reaction tube to achieve isothermal conditions, and it cannot interfere with optical access to the reaction zone.

To achieve a controllable axial temperature profile, the heating for the reactor will consist of twelve circular elements, each encircling the reactor centerline and arranged axially along the reactor. Figure II.B-4 shows one heating element, which will be custom-formed molybdenum disilicide rods. It is planned that these be connected in several sets of multiple elements, each controlled separately. The number of elements in each set will be variable. This will allow for more heat addition where there is an

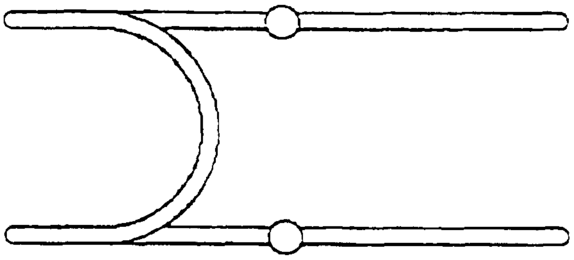

end view

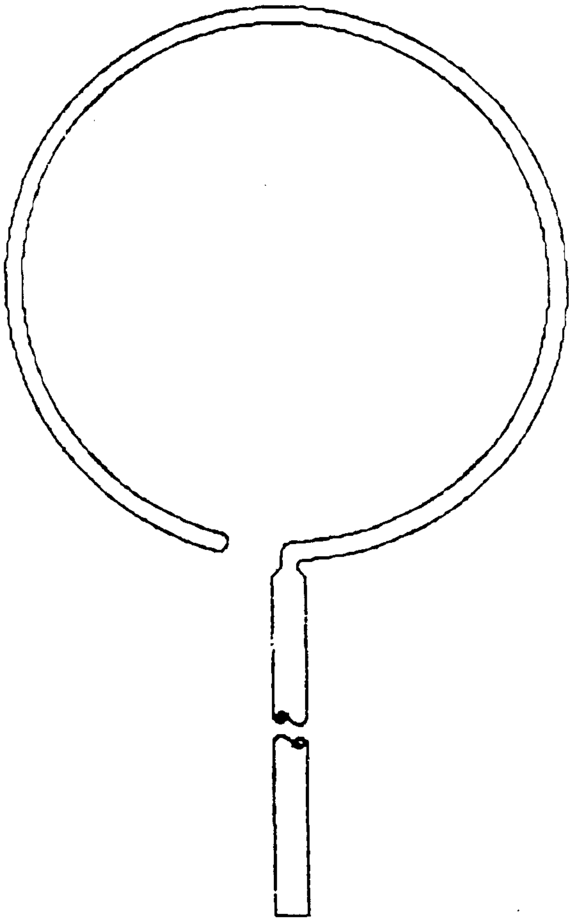

top view

Figure II.B-4 Heating Element

increased heat loss due to the probe, injection tube, or windows, and will also allow an isothermal profile to be kept. The variable number of heating elements in each set will allow for variations from run to run such as pressure, temperature, or location of the injection tube.

The heating rods selected for the reactor are compatible with the insulation materials and the atmosphere in the reactor. They also will operate on a moderate voltage and current, unlike some other heating methods, which will allow use of available power supplies and wiring.

Preheater -- In the preheater, the secondary air is heated by a silicon carbide heating element, which is capable of temperatures higher than the projected maximum temperature of the reactor. The primary flow will not be preheated. The placement of the preheater, shown in Figure II.B-2, is close to the reactor to minimize heat loss.

Feed System -- The feeder, based on an MIT/AFR design (Solomon, et al., 1982) and chosen to produce constant particle feed at low flow and high pressure, is shown in Figure II.B-5. The three separate feeder tubes help give a more uniform flow. High frequency, low amplitude vibration of the feeder will reduce the tendency of the char to pack. The particles are fed from the somewhat fluidized top of the reservoir. As the outlet tube is withdrawn very slowly with a motor, the particles are entrained by the flowing air through the tube. The feed rate will be controlled by adjusting the speed of the outlet tube.

The ceramic tube used to feed char particles into the reactor will not be cooled and will protrude into the reaction tube so the particles will equilibrate with reactor temperature when they enter the oxidizing atmosphere. A cooled injector tube will be used for sorbents to keep them from sintering before reaching the reacting environment. A ceramic flow straightener will be located at the end of the injection tube to ensure laminar flow in the test section.

Collection System -- A total collection probe will quench any particle reactions while directing the flow out of the reactor. As the gas enters

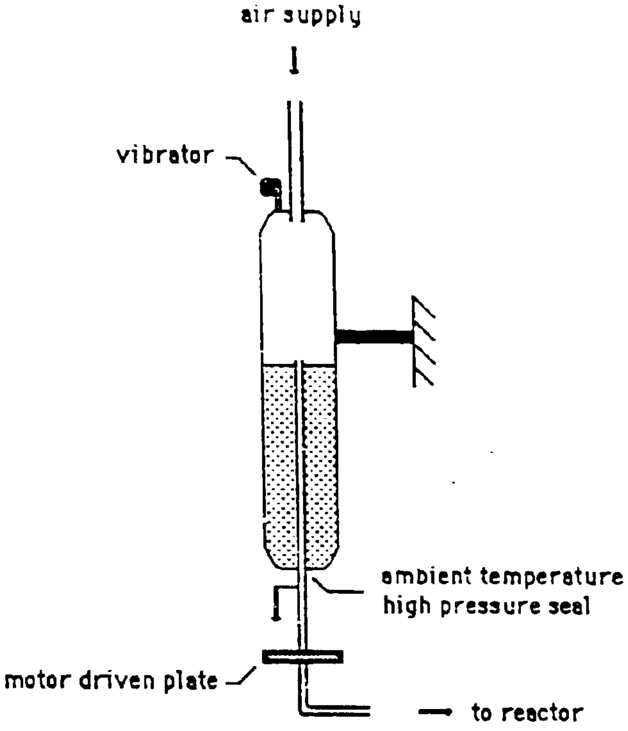

Figure II.B-5 Particle Feeder

the probe, which is smaller in diameter than the reactor, its velocity will increase while pressure decreases. Particle reactions will be quenched by injecting an inert gas into the flow at the top of the probe, to lower the gas temperature and oxygen concentration. The portion of the probe that extends into the reaction tube will be made of two concentric ceramic tubes. The quenching gas will flow between these and be injected into the main flow at the upper end of the probe. The lower ends of these ceramic tubes will be brazed to stainless steel tubes. This lower end will be water-cooled and protrude through the vessel wall. Fittings for the reactor outlet, quench gas inlet, and cooling water will be attached to the steel tube outside of the vessel.

Instrumentation -- The flow diagram for the facility was shown in Figure II.B-1. Before each test, the complete system will be evacuated. During the test, all of the products will be collected in the sample tank. The regulator and electronic flow controller at the reactor exit ensure a constant mass flow through the system and adjust the pressure differential to keep the reactor pressure constant as the sample tank pressure increases during a run. Flow meters in the primary, secondary, and quenching gas lines will measure the mass flows of the gasses, while particle mass flows will be determined by weighing the feeder before and after each run.

Platinum-rhodium thermocouples will measure the temperatures in the preheater and along the axis of the reaction tube. These will be input into the temperature controllers to maintain an isothermal profile. A number of pressure transducers at various locations will provide measurements for both control and monitoring purposes. Optical instrumentation will provide measurements of temperature, particle diameter, and velocity. This method has been successfully used (Tichenor et al.,1984 and Niksa et al.,1984) at Sandia National Laboratory. The data acquisition will most likely be performed by a microcomputer that will also reduce the data. Sandia's data acquisition system samples at a rate of 2 MHz with an accuracy of 12 bits. A similar optical instrument under construction at BYU's Combustion Laboratory will be used to determine if this speed and accuracy is needed. The system consists of optical lenses and filters, a trigger laser, photomultiplier tubes, a two channel data acquisition system, and calibration equipment. Particle temperature is obtained by measuring the light transmitted from the particle in two wavelength bands, using two-color pyrometry. Particle size and velocity are determined by measuring the pulses produced by the particle as it passes by a coded aperture.

High-Pressure Reactor Status -- The design of the high-pressure reactor is essentially complete. The reactor will enable combustion experiments at high-pressure and temperature with a wide range of residence times and axially controllable wall heat flux profiles. A design review was conducted with other researchers in the Combustion Laboratory and a cost and construction schedule has been developed.

Component 4 -- Fundamental Sulfur Capture Experiments

Sorbent capture of hazardous sulfur pollutants from coal during combustion or gasification represents a potentially important method for reducing sulfur oxides in entrained-flow systems, particularly at high pressure. However, the influence of fuel-rich or fuel-lean high pressure environments on sulfur capture by sorbents is not known, nor is the influence of such environments on nitrogen species well understood. Fundamental kinetic rate measurements for the formation, capture or destruction of sulfur or nitrogen species can provide valuable evaluation data for the pollutant submodel being developed under Subtask 2.g.

Literature Review -- There have been many studies of the capture of SO_2 by sorbents at atmospheric pressure. Most have focused on large particles (>50um) for times from minutes to hours; almost none were conducted at elevated pressures. Recently, there have been several small particle studies, also at atmospheric pressure, which show a particle size dependence.

Newton and Pershing (1987) showed that sulfation of small particles of CaO occurred very quickly, slowing significantly after about 300 ms due to blockage of the microporosity by growth of the product layer at the pore mouths, leaving fewer sites available for reaction. As expected, increasing the overall surface-to-volume ratio by decreasing particle size increased calcium utilization because proportionately more calcium is closer to the surface. Silcox et al. (1985) indicated that sulfur capture was insensitive to SO_2 partial pressure. Newton and Pershing (1987) confirmed this by showing that changes in S02 partial pressure above 1000 ppm have little effect on calcium sulfate formation. Silcox et al. (1985) also demonstrated that sulfur capture increased with an increasing Ca/S ratio. Milne and Pershing (1987) found that calcium utilization decreased with increasing Ca/S ratio. Newton et al. (1986) found that SO_2 capture was limited at 1500 K by the stability of the calcium sulfate.

Milne and Pershing (1987) showed that mixing was critical to early SO_2 capture. Slow mixing decreased the early capture, but had little effect on the overall sulfur capture. Newton et al. (1986) showed that SO_2 capture was strongly dependent on the sorbent used, dolomites giving a higher capture than calcites. Newton and Pershing (1987) suggested that this is due to MgO not reacting, which slows the pore mouth closure and therefore enhances capture. Borgwardt and Bruce (1986) found that the capture rate was strongly dependent on initial surface area of the sorbent. This meant that the calcination process was important to sorbent capture. Also, Pershing (1987) presented a graph that showed that hydrates calcine before significant sintering can occur. Carbonates calcine much more slowly, and sintering occurs before the calcination is complete. This gives hydrates a larger surface area than carbonates and makes them more reactive.

Sulfur Capture Model -- The only model that has been tested for particles smaller than 20μm and times less than 1 sec. is that developed by Newton and Pershing (1987), which includes surface and pore sulfation. Since pore mouth closure limits interior utilization, the model uses a simplified geometry of a spherical particle with cylindrical, non-intersecting pores pointing toward the particle center. It uses the distributed pore model, so it takes into account varying pore size. It also assumes that diffusion through the product layer controls the rate of the reaction.

The literature on sorbent capture reveals that mixing and calcination and sintering of the sorbent will have to be addressed for the experiments in the high pressure reactor. Good mixing of the sorbent and the SO_2 carrying gas must be developed to ensure good sulfur capture data. Poor mixing will yield a lower rate of reaction between the sulfur and sorbent. The sorbent must not be exposed to high temperatures until it is in the presence of SO2 to avoid premature calcination and sintering. The calcination will have to be carried out in such a way that the sorbent will have maximum reactivity when it is introduced into the reactor atmosphere.

No experiments or models discuss the effects of higher total pressure on sulfur capture. In consultation with combustion associates in the BYU Advanced Combustion Engineering Research Center (ACERC) and in Subtask 2.g. of this study, an experimental plan will be designed to determine the effects of high pressure on the sorbent-sulfur reaction. The literature search on high pressure and small particle sorbent studies will continue.

Plans

Reactor Construction

The reactor will be constructed during the next quarter. The Brigham Young University Research Machine Shop and the Mechanical Engineering machine shop will perform the majority of the reactor fabrication and an outside vendor will provide the custom heaters.

Instrumentation

Instrumentation for the facility will either be shared with the Combustion Laboratory or purchased during the first and second quarters of the second year. Sample time and resolution requirements for the optical data acquisition system will also be determined during this time. A similar optical system is in the process of being constructed for another project in the Combustion Laboratory. Tests will be conducted with this facility to determine the requirements necessary for the high pressure reactor optics.

Reactor/Instrumentation Checkout

To ensure safe operation, the facility will be pressure-tested first cold and then at maximum temperature before any other tests are conducted. The following tests will then be completed for a number of operating conditions in order to make necessary adjustments and verify proper operation:

1. The temperature profile will be checked by attaching a thermocouple to the injection tube and taking measurements axially along the reaction tube.
2. The flow controller will be monitored to ensure that the mass flow and reactor pressure remain constant.
3. Mass balances will be conducted to verify that the collection probe is collecting 100% of the injected particles.
4. The optical instrumentation will be operated with spherical particles of known diameters and velocities.

After the reactor has been completely adjusted and checked out, experiments similar to those done by previous researchers will be conducted to develop experimental procedures.

Char Preparation

As indicated previously, during the next quarter chars will be prepared from the Utah bituminous coal. As comparisons are made between properties of the chars prepared from the different methods discussed, decisions will be made for the preparation of chars from the remaining four coals (a North Dakota lignite, a Wyoming subbituminous, and two others yet to be specified). Chars from these coals will then be prepared during the second year. Measurements to be made include titanium in the ash, elemental and proximate analyses, surface area (N_2 BET), density, and particle size.

Experiments

During the second year, the construction of the high-pressure reactor will be completed and tested with the chars from the Utah bituminous coal. The first experimental runs for determining the rates of char oxidation will be with temperatures approximately 1300 K and pressures of about 5 atmospheres at various residence times. It will be important to determine whether or not diffusion dominates the rate measurements and the extent to which the rates of the chemical reactions can be measured.

II.C. SUBTASK 2.c. - SECONDARY REACTION OF PYROLYSIS PRODUCTS AND CHAR BURNOUT SUBMODEL DEVELOPMENT AND EVALUATION

Senior Investigator - Michael A. Serio
Advanced Fuel Research, Inc.
87 Church Street, East Hartford, CT 06108
(203) 528-9806

Objective

The objective of this subtask is to develop and evaluate by comparison with laboratory experiments, an integrated and compatible submodel to describe the secondary reactions of volatile pyrolysis products and char burnout during coal conversion processes. Experiments on tar cracking, soot formation, tar/gas reaction, char burnout, sulfur capture, and ignition will be performed during Phase I to allow validation of submodels in Phase II.

Accomplishments

Studies of ignition and soot formation in flames were performed in the transparent wall reactor (TWR). Several questions (calibration, detector saturation, aperture size, etc.) on the FT-IR technique were addressed. Attention is being focused on what controls ignition (heterogeneous or homogeneous oxidation) and soot formation. Four samples have been completed: a raw Rosebud subbituminous coal, chars prepared from this coal at 900 and 1500°C and a demineralized Rosebud coal. To provide data on the relative rate of volatile loss vs oxidation weight loss, measurements were being made on a TGA and chars are being prepared for measurements in the TWR.

Results

FT-IR Diagnostics

Improvements were made in the optical system for the Transparent Wall Reactor (TWR). We have had some problems with detector saturation when using the FT-IR diagnostics for making temperature measurements. An ethylene diffusion flame has been used in order to provide a simpler system for solving the problems in the optics. It is also a system which has been well characterized in other reactors. The recent addition of a silicon filter appears to solve the detector non-linear response problem for laminar flow conditions, although problems still occur under turbulent flow conditions.

Additional work was done on the optics for the Transparent Wall Reactor (TWR). A detector change was made from the MCT type to the InSb type. The latter is more sensitive to the infrared source and does not exhibit the non-linear effect, although, it cuts off in the 1800 wavenumber region. This appeared to help the data acquisition.

Hydrocarbon Cracking

The literature reviews continued for components 1 (gas-phase cracking) and component 3 (tar/gas reactions). It was found that the extent of homogeneous cracking of tar appear to be well correlated with the aromatic hydrogen and aromatic carbon content but that the nature of heterogeneous cracking depends strongly on the surface type. The reactivity of tar toward reactive gases like CO_2 and O_2 depends on its prior thermal history. In this respect, the tars are similar to chars.

Combustion Studies

Studies were made of ignition and soot formation in the Transparent Wall Reactor (TWR). Measurements were made using FT-IR diagnostics on raw Rosebud subbituminous coal, demineralized Rosebud, and Rosebud char. The measured properties include concentrations and temperature of gas species, char and soot.

Experimental - The Transparent Wall Reactor (TWR) facility, shown in Fig. II.C-1, consists of an electrically heated furnace and a heat exchanger. Gas is passed through the heat exchanger and exits the top of the furnace after passing a screen to smooth the flow. The hot gas stream, which is 10 cm in diameter, remains relatively hot and undisturbed for approximately 20 cm above the screen. Coal entrained in a cold carrier gas is injected through a co-axial 4 mm diameter tube.

The coal is fed using a previously described system (Solomon et al., 1982) in which gas enters the top end of an enclosed cylinder filled with coal and exists through a tube which is slowly lowered through the bed of coal at a constant rate. Three cylinders were used to achieve a steady flow. Nitrogen was used for pyrolysis studies and air for combustion. The feed rate for the carrier gas was

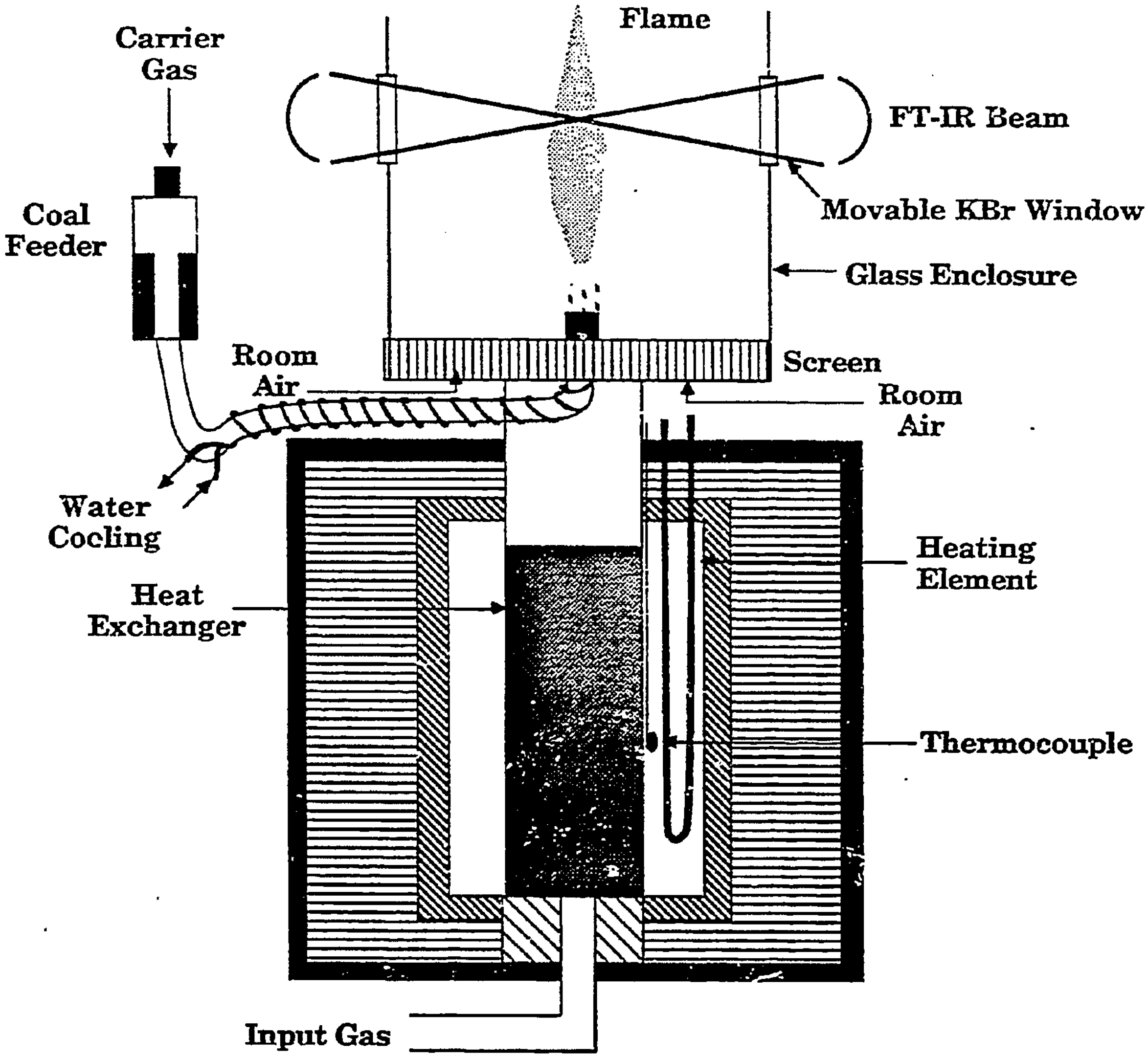

Figure II.C-1. Transparent Wall Reactor.

225 ml/min and for the hot gas, 175 l/min. The hot gas exits the screen at a temperature of 850°C and a velocity of 2.8 m/sec. Short exposure photographs show particle tracks which indicate that the coal particles are moving at about 2.5 m/sec near the injector and 4.8 m/sec in the flame.

An octagonal glass enclosure shields the reacting stream from room air currents. The enclosure has movable KBr windows to allow access to the flame by the FT-IR spectrometer which is shown in Fig. II.C-2. A flow of air along the inside of the enclosure keeps the glass from overheating. The cooling air and reacting stream are vented into a duct connected to an exhaust fan through a damper valve. The damper valve, and gas flows were adjusted to achieve a steady flame under combustion conditions. Figure II.C-3 shows photographs of a lignite which ignites close to the nozzle and a low volatile bituminous coal which ignites higher up.

The Nicolet 20SX FT-IR and transfer optics to focus the beam within the sample stream are illustrated in Fig. II.C-2. Emission measurements are made with the movable mirror placed in the beam to divert it to the emission detector as shown. Transmission measurements are made with the movable mirror out of the beam.

The samples used in these experiments were -200, +325 mesh sieved fractions of coal, char and demineralized char. The samples were also characterized in a TGA to determine their weight loss at constant heating rate in nitrogen and in air.

Analysis - For multi-phase reacting systems, measurements are made of the transmittance and the radiance, and from these a quantity called the normalized radiance is calculated. The analysis, which follows Siegel and Howell (1972) has been presented previously (Best et al., 1986). The relevant equations for a homogeneous medium are presented below.

Transmittance, τ_ν - The transmittance, τ_ν, is defined as

$$\tau_\nu = I_\nu / I_{o\nu} \qquad \text{(II.C-1)}$$

where $I_{o\nu}$ is the intensity transmitted in the absence of sample, while I_ν is that transmitted with the sample stream in place. For a medium containing gases and soot with absorption coefficients α_ν^g and α_ν^s and particles of geometrical cross sections area A at a density of N particles cm^{-3},

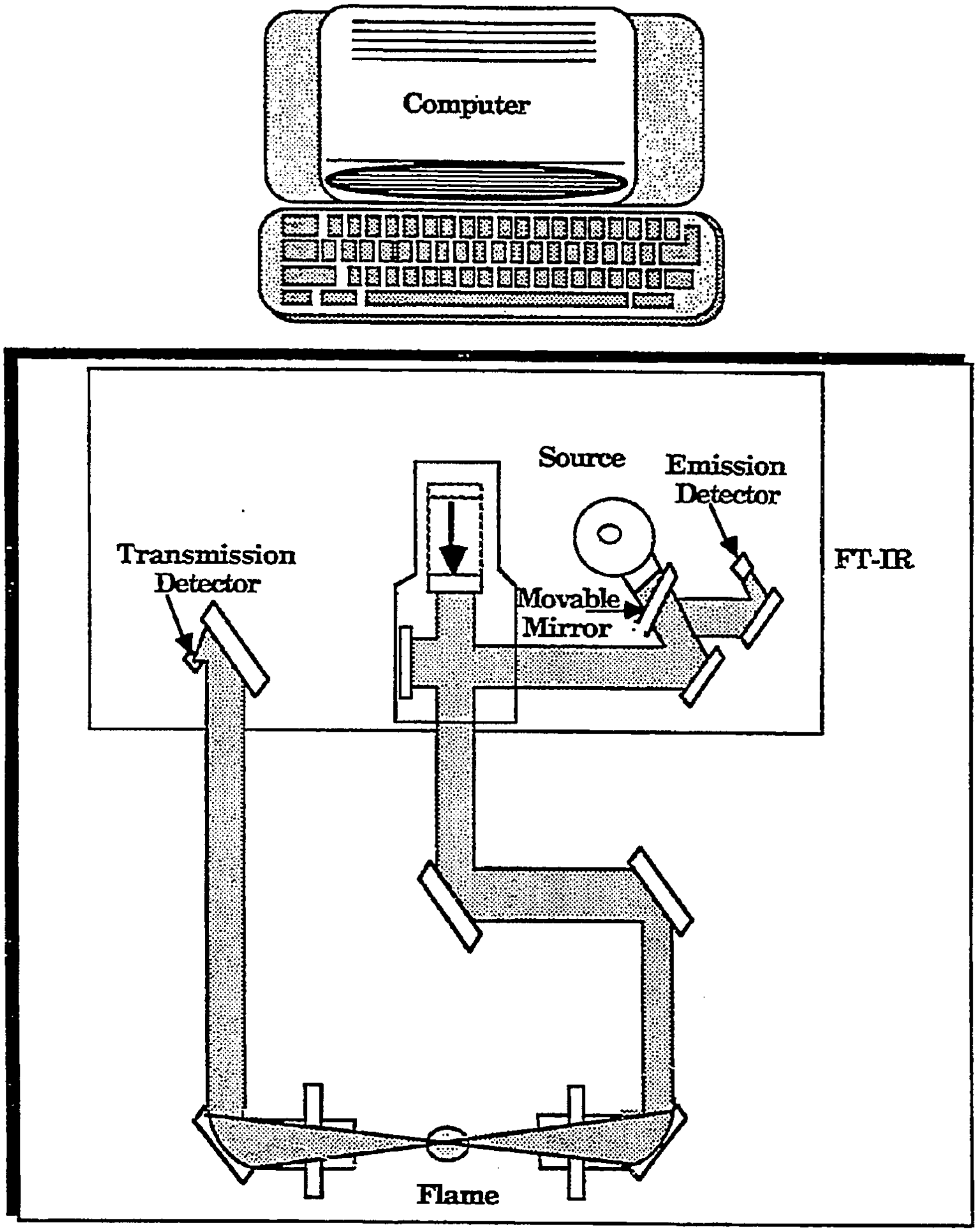

Figure II.C-2. Spectrometer and Transfer Optics.

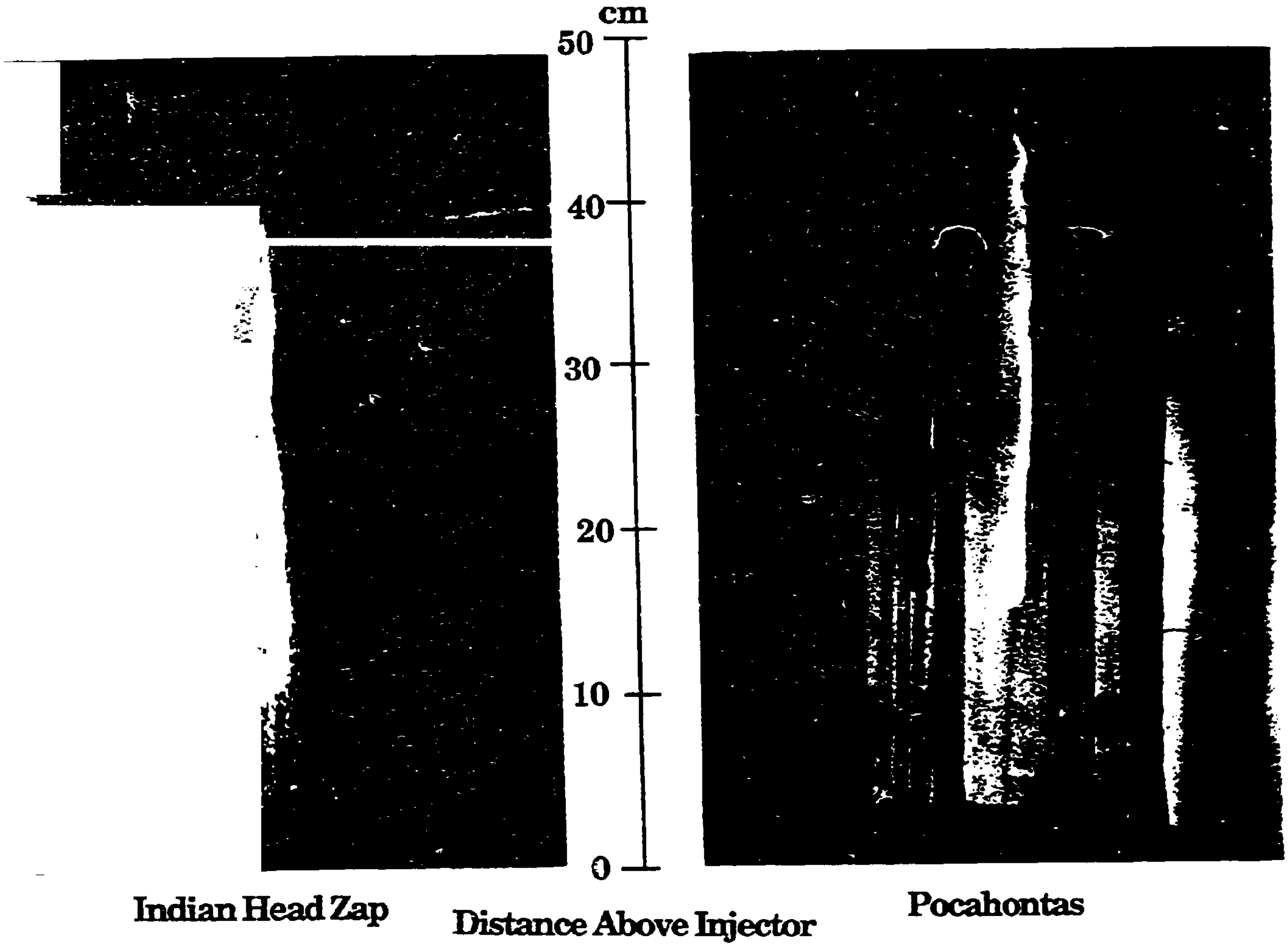

Figure II.C-3. Photographs of Zap North Dakota Lignite Flame (left) and a Pocahontas Bituminous Coal Flame (right). The Scale in the Center is Distance above the Injector Nozzle.

$$\tau_\nu = \exp(-(\alpha^s_\nu + \alpha^g_\nu + NAF^t_\nu)\, L) \qquad \text{(II.C-2)}$$

where F^t_ν is the ratio of the total cross section (extinction) to geometric cross section, and L is the path length. τ_ν is sometimes plotted as a percent.

Radiance, R_ν - To measure the sample radiance, R_ν, the radiative power emitted and scattered by the sample with background subtracted, S_ν, is measured, and converted to the sample radiance,

$$R_\nu = S_\nu / W_\nu \qquad \text{(II.C-3)}$$

where W_ν is the instrument response function measured using a black-body cavity.

Normalized Radiance, R^n_ν - The normalized radiance, R^n_ν, is defined as,

$$R^n_\nu = R_\nu/(1-\tau_\nu) \qquad \text{(II.C-4)}$$

which can be expressed in terms of the properties of the medium as

$$R^n_\nu = \frac{\alpha^s_\nu R^b_\nu(T_s) + \alpha^g_\nu R^b_\nu(T_g) + NA\,\epsilon_\nu\, R^b_\nu(T_p) + NAF^{s'}_\nu R^b_\nu(T_w)}{\alpha^s_\nu + \alpha^g_\nu + NAF^t_\nu} \qquad \text{(II.C-5)}$$

where $R^b_\nu(T_g)$, $R^b_\nu(T_s)$ and $R^b_\nu(T_p)$ are the black-body emission spectra at the temperatures of the gas, soot, and particle, respectively. ϵ_ν is the particle's emittance and $F^{s'}_\nu$ is the cross section for scattering radiation into the spectrometer. No scattering is assumed for soot particles in the IR region. For the geometry of the TWR where measurements are made perpendicular to the length of an optically thin flame, the scattering term may be neglected.

Results - Results were obtained for a series of samples in the TWR using the FT-IR diagnostics for concentrations and temperatures and in the TGA for pyrolysis and oxidative weight loss.

FT-IR Measurements - FT-IR measurements were made along the center of the flame at several positions above the coal injector for flames from several coals under identical conditions. Figures II.C-4 and II.C-5 are spectra obtained with Rosebud subbituminous coal. Figure II.C-4 presents four pairs of spectra (transmittance and normalized emittance) at: 5 cm above the nozzle, in the region

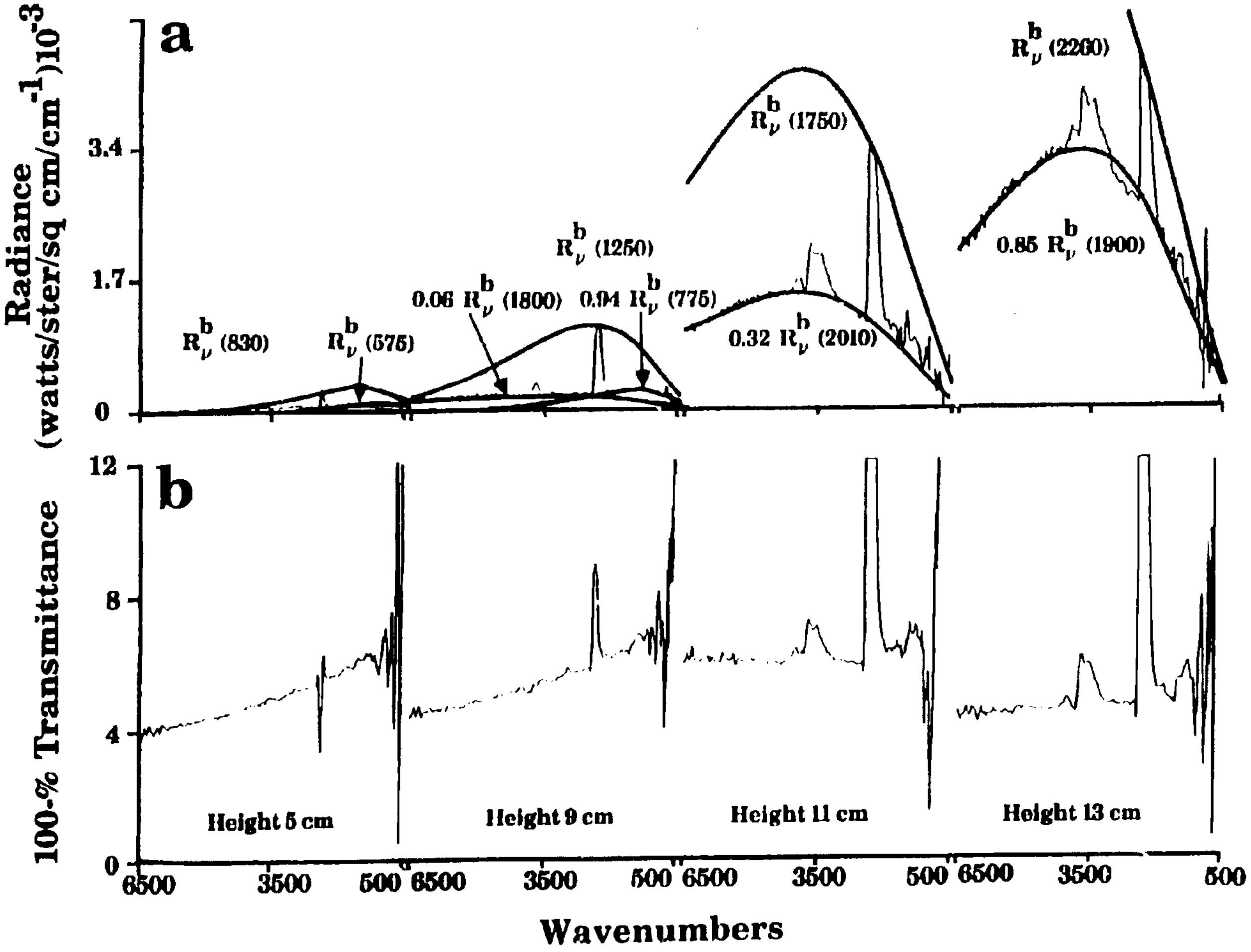

Figure II.C-4. FT-IR Spectra at Several Positions within the TWR for a Rosebud Subbituminous Coal Flame. a) Normalizing Emittance and b) 100% - Transmittance.

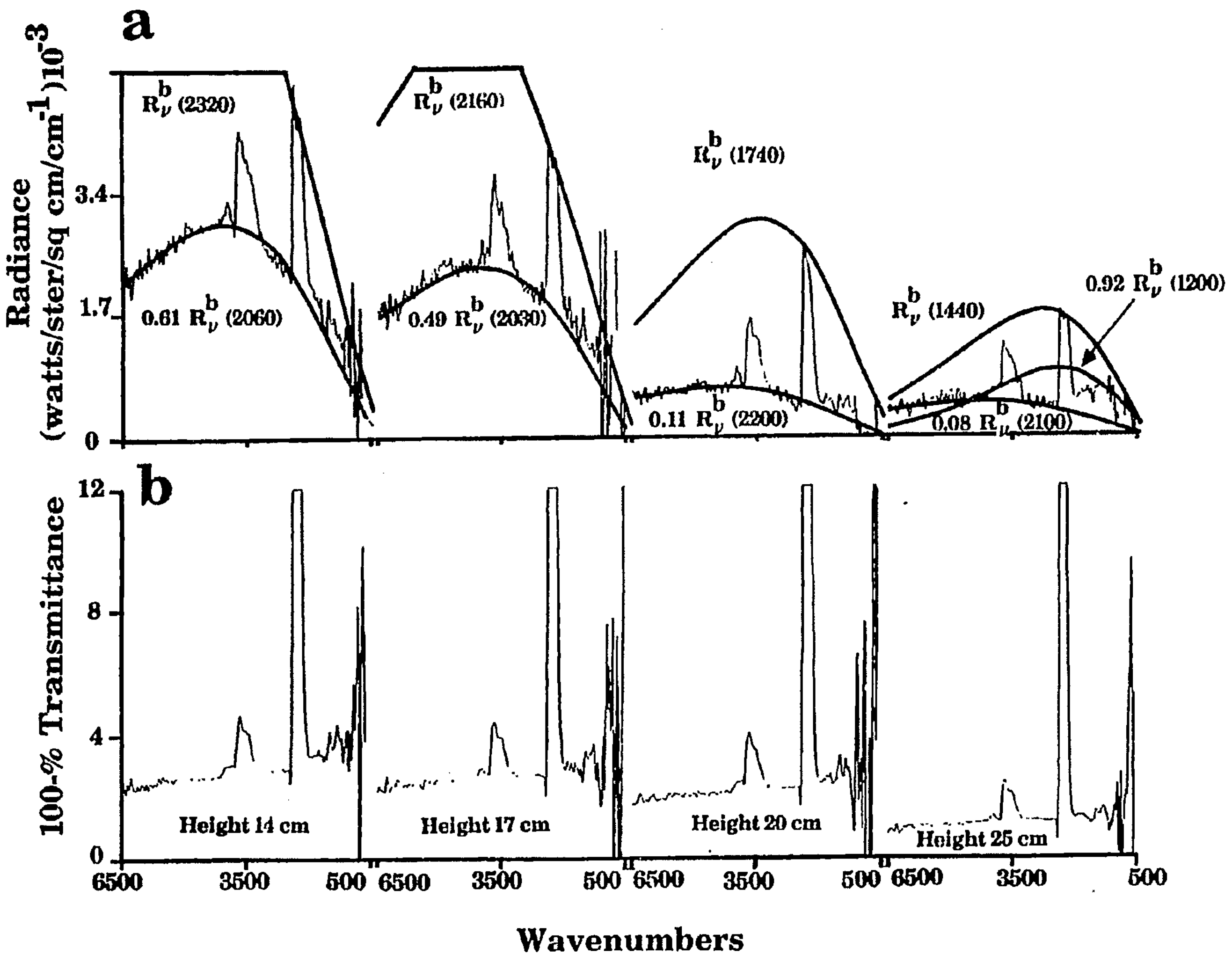

Figure II.C-5. FT-IR Spectra at Several Positions within the TWR for a Rosebud Subbituminous Coal Flame. a) Normalizing Emittance and b) 100% - Transmittance.

prior to ignition; 9 cm, at the beginning of the ignition region; 11 cm, in the ignition region; and 13 cm, in the brightest part of the flame.

The attenuation in Fig. II.C-4b (5 cm) is almost entirely from particles i.e., α_ν^g and $\alpha_\nu^s \approx 0$. The shape of the spectrum slopes due to diffraction effects. In the optically thin limit, the amplitude of $(1-\tau_\nu)$ is proportional to the intersected surface area of the particles, NAL, times the extinction efficiency, F_ν^t. F_ν^t has the shape predicted by Mie theory for 200 x 325 mesh particles and a 2° collection angle in the spectrometer. At 9 cm, a few particles have ignited and attenuation from CO_2 and H_2O is larger. At 11 cm, the attenuation is lower due to spreading and heating of the particle stream and flatter due to the appearance of soot. The attenuation in the ignition zone (11 and 13 cm) contains larger contribution for CO_2 and H_2O, a contribution from soot, as well as a contribution from the particles. F_ν^t for the particles is assumed to have the same shape as prior to ignition and the soot contribution is the difference between the particle attenuation and the total as shown in Fig. II.C-6. Much larger soot contributions are observed for bituminous coals. Figure II.C-5b illustrates the spectra above the ignition region. $(1-\tau_\nu)$ is progressively reduced at 14, 17, 20, and 25 cm as the particles have burned out. The 25 cm case on an expanded scale in Fig. II.C-6c shows the presence of ash (the dips between 2500 and 500 cm^{-1}).

Radiance measurements are shown in Figs. II.C-4a and II.C-5a. In the absence of soot and in regions of the spectrum away from gas lines Eqs. II.C-2, II.C-4 and II.C-5 reduces to R_ν = NAL ϵ_ν $R_\nu^b(T_p)$ in the optically thin limit. NAL can be determined from the transmittance spectrum using the theoretical value of F_ν^t at one wavelength (F_ν^t = 1.2 at 6500 $cm,^{-1}$). The temperature can then be determined by comparing R_ν/NAL with $R_\nu^b(T_p)$ if ϵ_ν is known. Figure II.C-4a shows R_ν/NAL prior to ignition (5 cm). A particle temperature of 575 K is determined from the region between 1200 and 1600 cm^{-1} where for coal (which is non-gray (Solomon et al. 1986d, 1987b, Best et al. 1986)) $\epsilon_\nu = 1$. The spectra at 9 cm shows, R_ν /NAL in the region where a few particles have ignited. The temperature of the ignited particles (1800 K) is determined from the shape of the region above 4000 cm-1 assuming a gray-body for char (Best, 1986). It is substantially higher than the unignited particles (775 K). This is shown on an expanded scale in Fig. II.C-7. Figure II.C-4b shows the R_ν/NAL in the region where many (11cm) and then most (13 cm) of the particles are ignited. The shape of the spectrum is consistent with a temperature of 2010 K. The amplitudes are only 0.32 and 0.85 of the black-body. This is as expected, assuming $\epsilon_\nu = 0.7 \rightarrow 0.9$ for char (Best, 1986). In Fig. II.C-5b, the particle contributions to the radiance becomes progressively lower as the

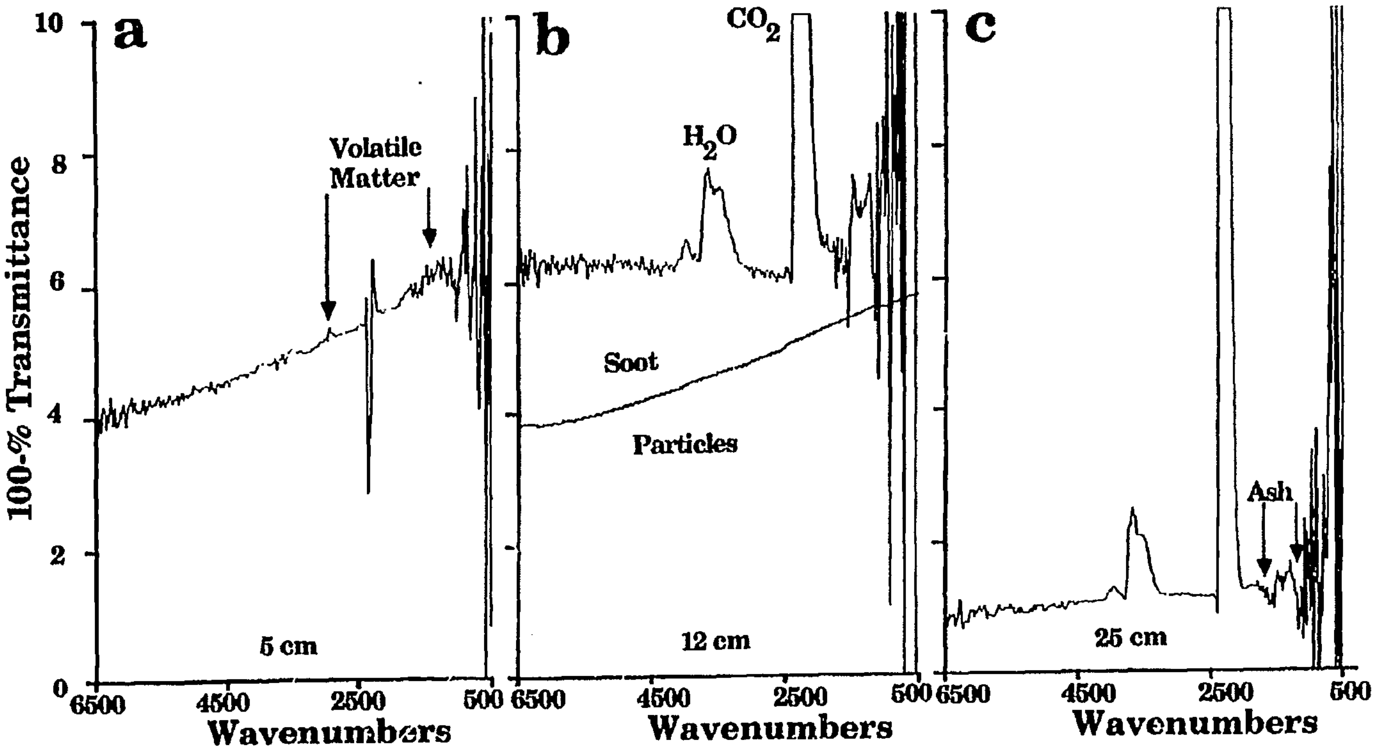

Figure II.C-6. 100% - Transmittance at Several Positions in the Flame Showing a) Particles Alone, b) Particles plus Soot, and c) Ash.

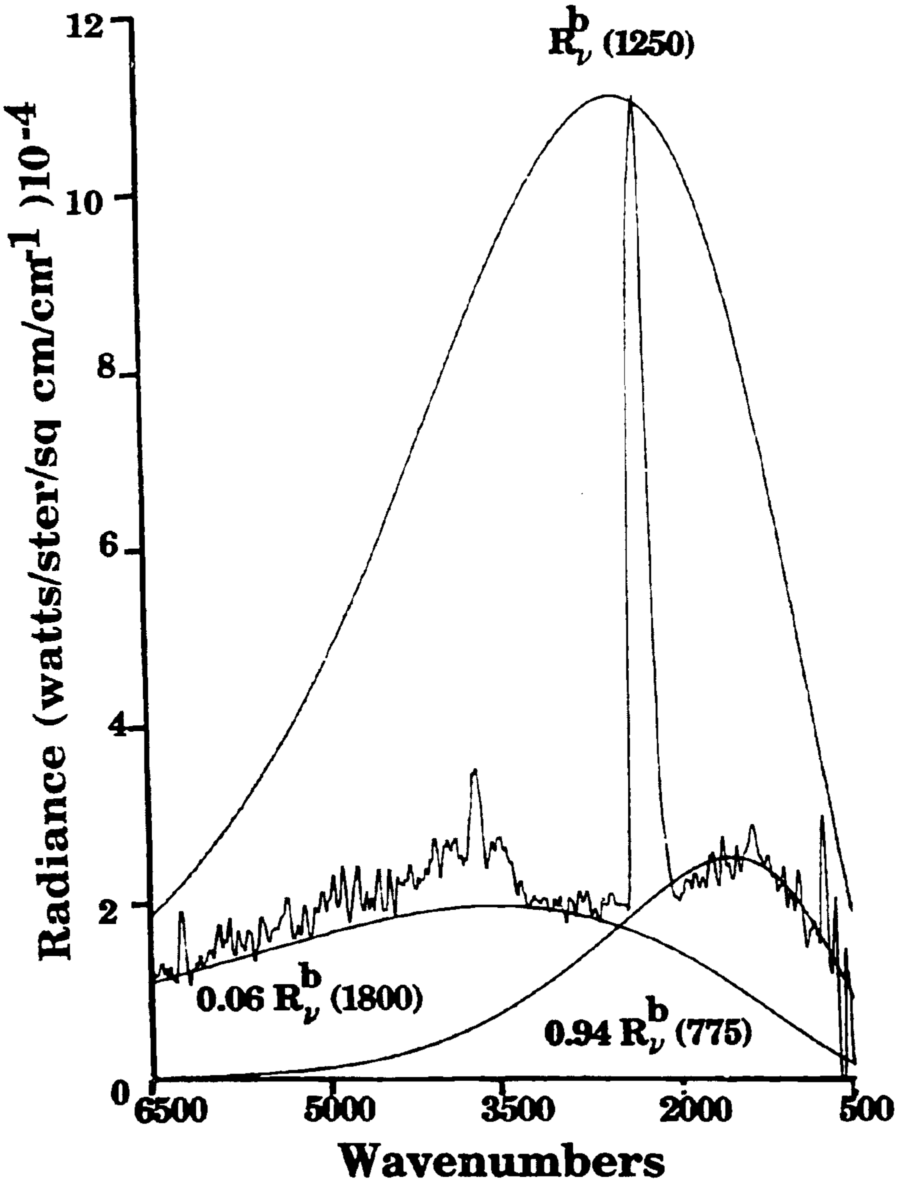

Figure II.C-7. Normalized Radiance at 9 cm Above the Nozzle where a few Particles have Ignited. Same as in Fig. II.C-4 (9 cm).

particles burnout leaving fly ash.

After the particle temperatures and attenuation contributions from particles have been determined, the CO_2 temperatures can be obtained from the normalized radiance by application of Eq. II.C-5. In the absence of particles, Eq. II.C-5, reduces to $R^n_\upsilon = R^b_\upsilon(T_g)$.

Flame Characteristics for Four Samples - In addition to the Rosebud coal flame discussed above, flames of the Rosebud chars prepared at 900°C and 1500°C and of a demineralized Rosebud coal were also studied. The properties of these samples are discussed in Table II.C-1. The results are summarized in Tables II.C-2 to II.C-5 and Figs. II.C-8 to II.C-11 which present the particle and CO_2 temperatures and percent of particles ignited times the emissivity, as well as the soot, CO_2 and particle concentrations as a function distance above the nozzle

The chars ignite heterogeneously since they contain little volatile matter. The 900°C char ignites at about 13 cm, slightly above the coal. The 1500°C char does not ignite until 33 cm. Neither char produces much soot.

The demineralized Rosebud also ignites at about 13 cm, higher than the coal (10 cm). It is possible that the mineral matter helps the ignition either heterogeneously or homogeneously through the organically bound minerals. The difference in ignition distance of 3 cm is not large compared to the expected, uncertainty of ± 2 cm, so additional investigation is necessary.

The low reactivity (1500°C) char produces a significantly lower particle temperature than 900°C char or the raw coal. The demineralized char also shows a lower particle temperature. This is believed to be due to (or be correlated with) the higher soot yield which radiates energy, lowering the temperature. The soot concentration for the demineralized coal is more than twice as high as that for the raw coal. The two chars show almost no soot, consistent with their low volatile yields.

A comparison of the four sets of curves in Figs. II.C-9 to II.C-11 shows several additional features. 1) The Rosebud and demineralized coals show a distinct ignition point where the coal particle temperature, CO_2 temperature, CO_2 concentration and soot concentration all take a sudden jump. Photographs of the flame show volatile flames around the particles just at the ignition point. 2) In contrast, the two chars (which ignite heterogeneously) show a more gentle change in

TABLE II.C-1

CHARACTERISTICS OF SAMPLES USED IN THE FLAME STUDIES

Sample	% Ash Air, 30°C/min to 900°C, corrected for H_2O	% Volatile Matter, N_2 30°C/min to 900°C corrected for H_2O	% DAF Volatile Matter
Rosebud	15.14	36.3	42.8
Demineralized Rosebud	3.68	37.7	39.1
900°C Rosebud Char	23.54	14.6	19.1
1500°C Rosebud Char	23.38	2.0	2.6

Table II.C-2. Flame Properties for Montana Rosebud Subbituminous Coal.

Height (cm)	Particle R_n^b(K)	CO_2 T(°K)	% of Gray Body	Particle Conc.	Soot Conc.	CO_2 Conc.	H_2O Conc.
5	575	1056	100	3.94	0	0	0.13
9	1800 775	1585	6, 94	4.27	0.14	2.04	0.56
10	1920 875	1860	14, 86	5.13	0.91	10.83	1.27
11	2000	2130	32	3.98	2.09	21.56	2.61
12	1955	2300	56	3.98	2.30	26.59	2.98
13	1900	2330	85	2.86	1.51	31.20	2.86
14	2060	2370	61	2.01	0.41	31.93	3.29
15	2050	2320	54	1.81	0.49	31.51	2.86
17	2030	2190	49	1.75	0.55	33.07	2.76
20	2190	1790	11	1.53	0.22	33.32	3.04
25	2100	1465	8	0.71	0.07	25.50	1.81

Table II.C-3. Flame Properties for Montana Rosebud 900°C Char Formed in the Entrained Flow Reactor.

Height (cm)	Particle R_n^b(K)	CO_2	% of Gray Body	Particle Conc.	Soot Conc.	CO_2 Conc.	H_2O Conc.
5	1020	1227	0.32	7.57		0.83	0
11	1230	1307	0.26	6.97		2.47	0.25
13	1545	1555	0.17	6.04		3.65	0.56
15	1820	1726	0.27	4.45	0.12	7.33	0.48
16	1905	2100	0.28	6.97		10.53	0.87
17	1965	2327	0.31	5.98		15.13	1.18
18	2100	2339	0.36	4.73	0.37	24.04	1.78
19	2150	2390	0.34	3.79	0.41	26.10	2.00
20	2100	2322	0.39	3.29	0.45	24.57	1.37
21	2120	2233	0.37	3.16	0.30	28.14	1.81
23	2080	2280	0.41	3.16	0.22	27.03	1.84
25	2070	2192	0.37	2.47	0.14	26.79	1.52
28	2090	2098	0.28	2.03	0.14	26.81	1.51
33	2020	1680	0.20	1.08	0.10	17.37	0.83
43		1410		0.25		8.6	0.36

Table II.C-4. Flame Properties for Montana Rosebud 1500°C Char Formed in the Entrained Flow Reactor.

Height (cm)	Particle R_n^b(K)	CO_2 T(°K)	% of Gray Body	Particle Conc.	Soot Conc.	CO_2 Conc.	H_2O Conc.
5	820	N.A.	52	10.26	0	0.43	0.45
14	950	980	67	6.05	0	0.39	0.09
25	1050	1065	67	5.49	0	0.56	0.15
33	1175	1815	53	4.72	0	0.89	0.13
40	1850	2365	32	2.28	0	3.20	0.23
44	1850	2225	64	0.84	0	11.88	0.70

Table II.C-5. Flame Properties for Demineralized Montana Rosebud Subbituminous Coal.

Height (cm)	Particle R_n^b(K)	CO_2 T(°K)	% of Gray Body	Particle Conc.	Soot Conc.	CO_2 Conc.	H_2O Conc.
5	700	1310	100	7.05	0	0.31	0.31
10	755	1315	100	7.66	0	0.76	0.34
13	775	1385	100	7.83	0.21	1.69	0.45
14	1975	3500	44.2	6.91	1.22	8.36	0.76
15	1780	2135	56.8	5.72	3.74	20.93	2.08
16	1690	2380	79.4	6.08	5.31	20.56	2.12
17	1710	2105	86.2	6.22	3.58	25.36	2.56
18	1800	2083	56.2	5.57	1.52	27.03	2.42
20	1800	1955	57.5	4.23	0.96	26.78	2.01
23	1850	2085	62.5	3.20	0.53	26.72	1.97
26	1840	2040	61.0	2.05	0.10	26.67	1.94
31	1810	2005	70.5	1.85	0.05	28.10	1.76
39	1700	1865	77.0		0		
44	1590	1835	80.6	0.73	0	20.43	1.44

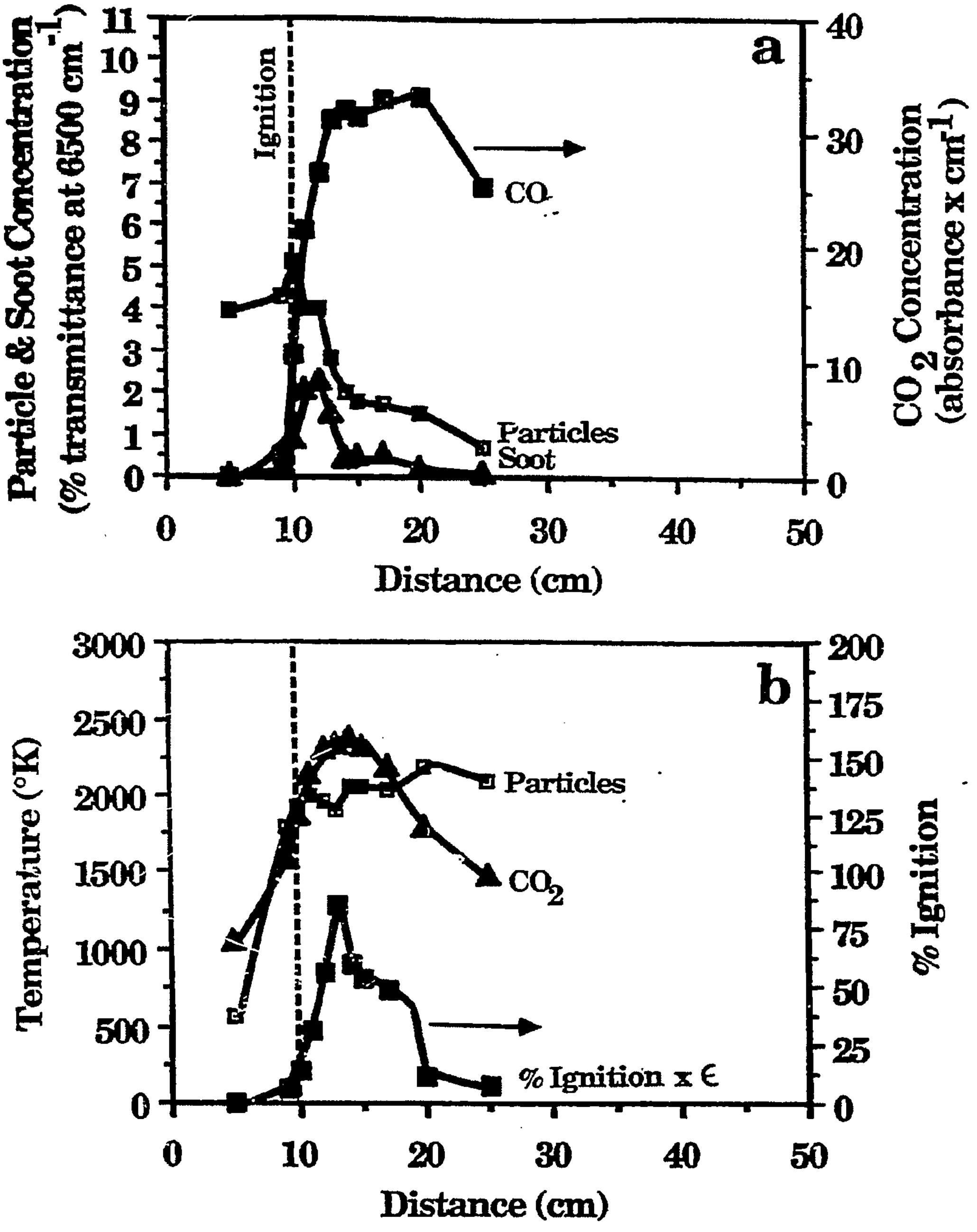

Figure II.C-8. Flame Properties as a Function of Distance Above the Injection Nozzel for Montana Rosebud Subbituminous Coal. a) Concentrations of CO_2, Particles and Soot and b) Temperature of Particles and CO_2 and Percent of Particles Ignited Times Emissivity.

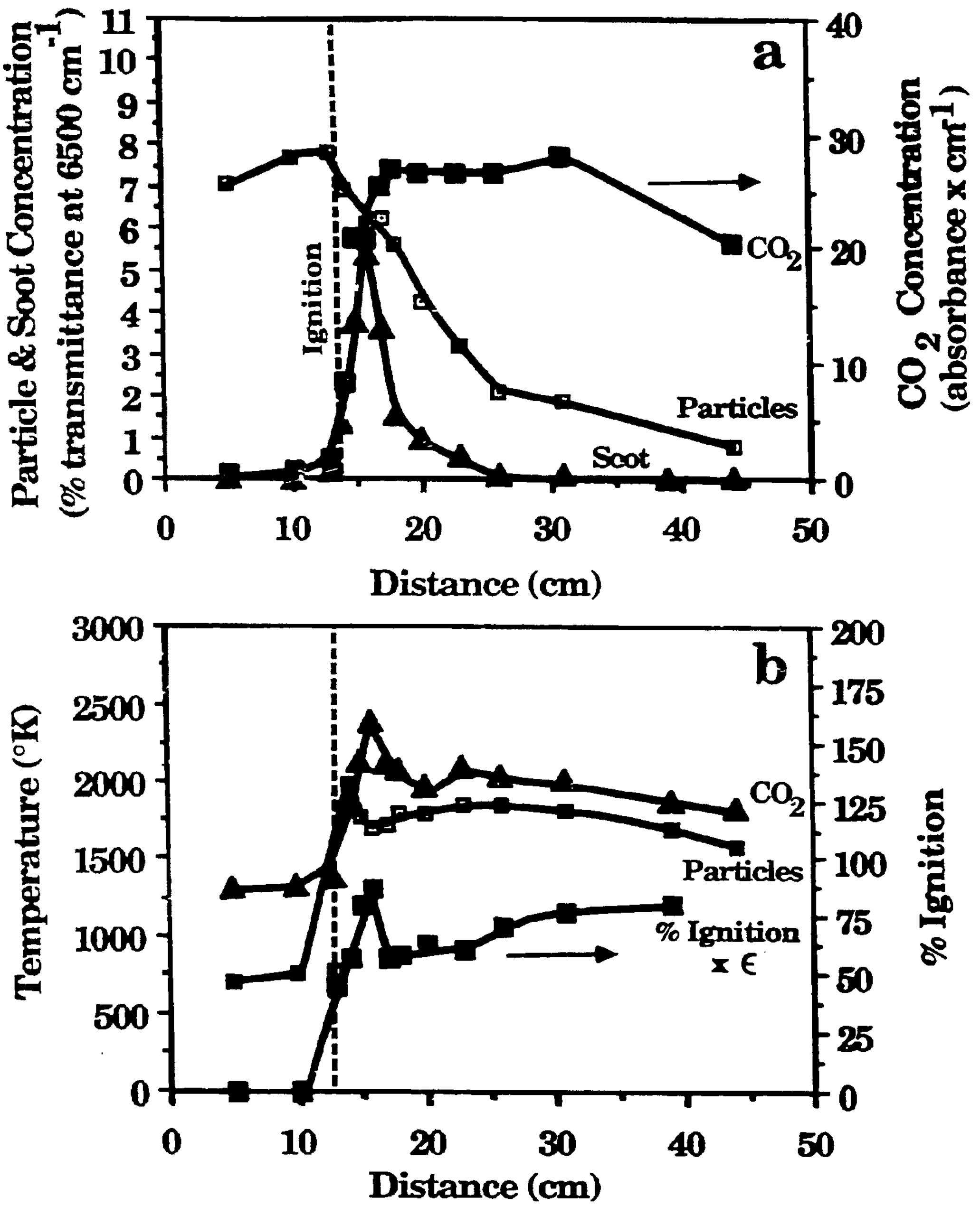

Figure II.C-9. Flame Properties as a Function of Distance Above the Injection Nozzel for Demineralized Montana Rosebud Subbituminous Coal. a) Concentrations of CO_2, Particles and Soot and b) Temperature of Particles and CO_2 and Percent of Particles Ignited Times Emissivity.

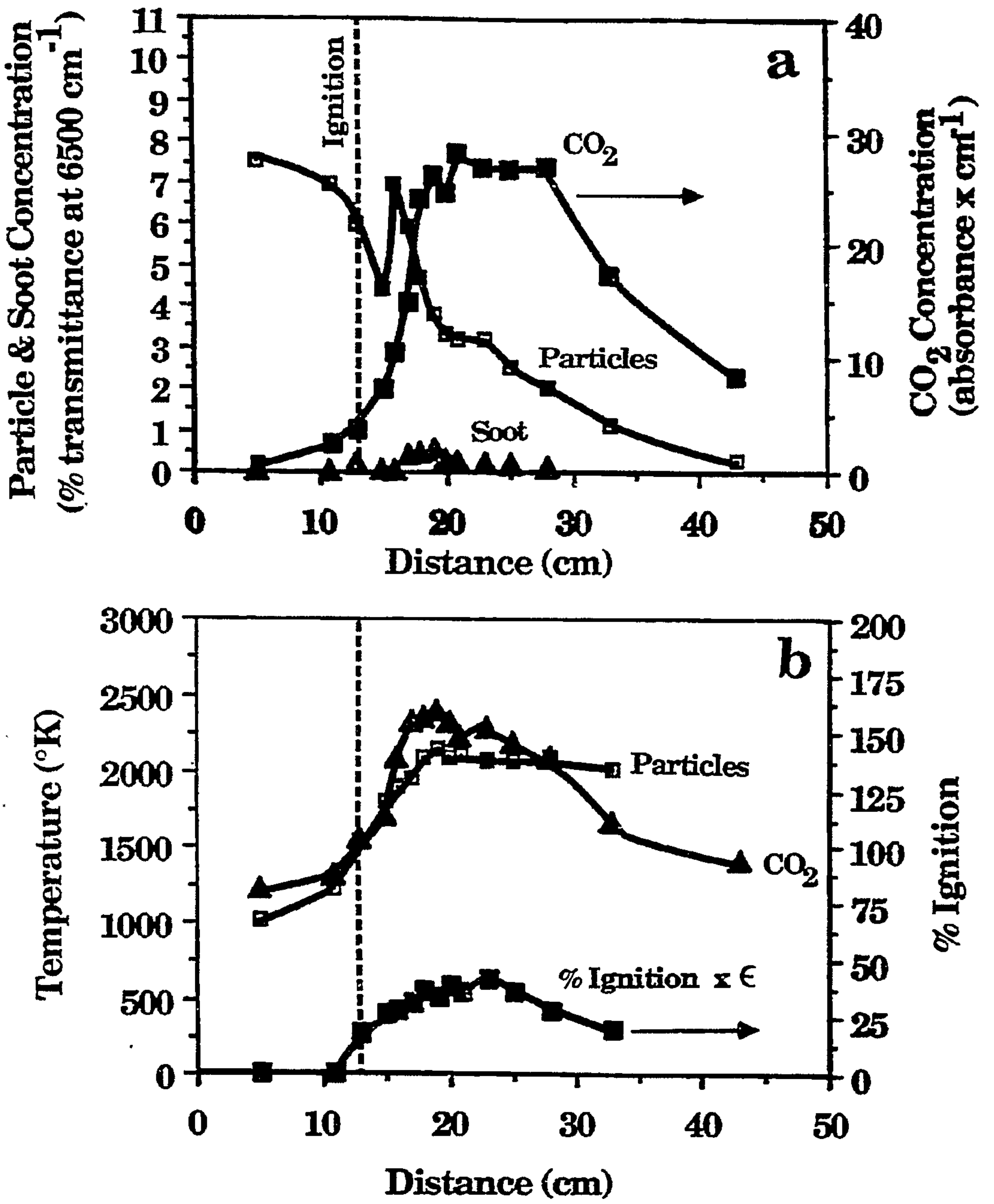

Figure II.C-10. Flame Properties as a Function of Distance Above the Injection Nozzel for Montana Rosebud 900°C Char Formed in the Entrained Flow Reactor. a) Concentrations of CO_2, Particles and Soot and b) Temperature of Particles and CO_2 and Percent of Particles Ignited Times Emissivity.

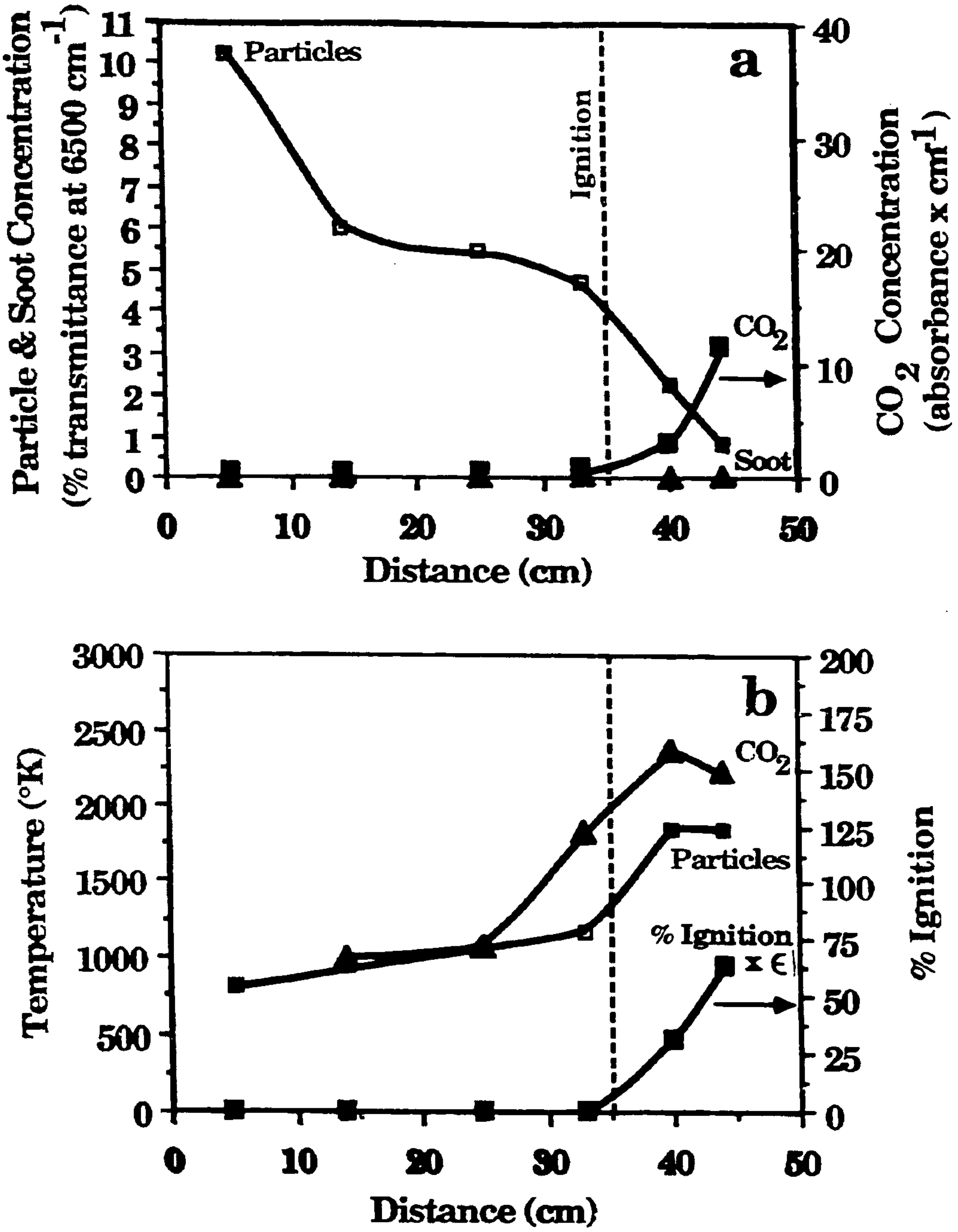

Figure II.C-11. Flame Properties as a Function of Distance Above the Injection Nozzel for Montana Rosebud 1500°C Char Formed in the Entrained Flow Reactor. a) Concentrations of CO_2, Particles and Soot and b) Temperature of Particles and CO_2 and Percent of Particles Ignited Times Emissivity.

the ignition region and no volatile flame. 3) The burnout of the flame is most rapid for the Rosebud followed by the demineralized Rosebud and Rosebud 900°C char which are similar and then the 1500°C char. 4) It is interesting to note that at 5 cm above the nozzle, it is the Rosebud char which produces the hottest particles. It appears that the volatile exiting the coal prevents any heterogeneous oxidation. 5) The fraction of ignited particles times the emissivities is high for the demineralized coal and fairly low for the chars. Either the percent of ignited particles is low or the emissivity is low. A possible reason for low emissivity is the coating of minerals on the surface. This possibility is being investigated.

TGA Measurements - A goal of this research is to relate the gasification behavior to properties of the coal or char which can be easily measured in the laboratory. As a possible indicator of ignition behavior, measurements were made of the weight loss measured at constant heating rate in air in a TGA. If it is assumed that any volatile products would be rapidly oxidized, then this test indicates the rate of oxidation of the coal either through heterogeneous combustion or homogeneous combustion of the volatiles.

The results for weight loss in air for the four Rosebud samples are present in Figs. II.C-12 and II.C-13 as the solid lines. The temperatures at which 10% weight loss is achieved (excluding moisture loss at 100°C) are summarized in Table II.C-6. The temperatures are plotted in Fig. II.C-14 as a function of the ignition distance above the injection nozzle. The ignition distances are taken from Figs. II.C-8 to II.C-11. For these four samples, there is good correlation between the temperature required for 10% weight loss and the ignition distance.

To address the question of whether the ignition is heterogeneous or homogeneous, the weight loss was also measured in the TGA under nitrogen. These are presented as the dashed lines in Figs. II.C-12 and II.C-13. The temperature for 10% weight loss are also summarized in Table II.C-6. For the chars, the weight loss in air is completely due to heterogeneous oxidation, as the pyrolysis weight loss occurs at a much higher temperature.

For the demineralized coal, the 10% weight loss is mostly from pyrolysis. If this result is projected to temperatures appropriate to the TWR, the pyrolysis weight loss should be even more dominant if activation energies of 55 Kcal and 34 Kcal are assumed for pyrolysis and oxidation, respectively. Photographic observations of the ignition zone shows volatile flames burning as spherical regions much larger than the particles, consistent with homogeneous ignition.

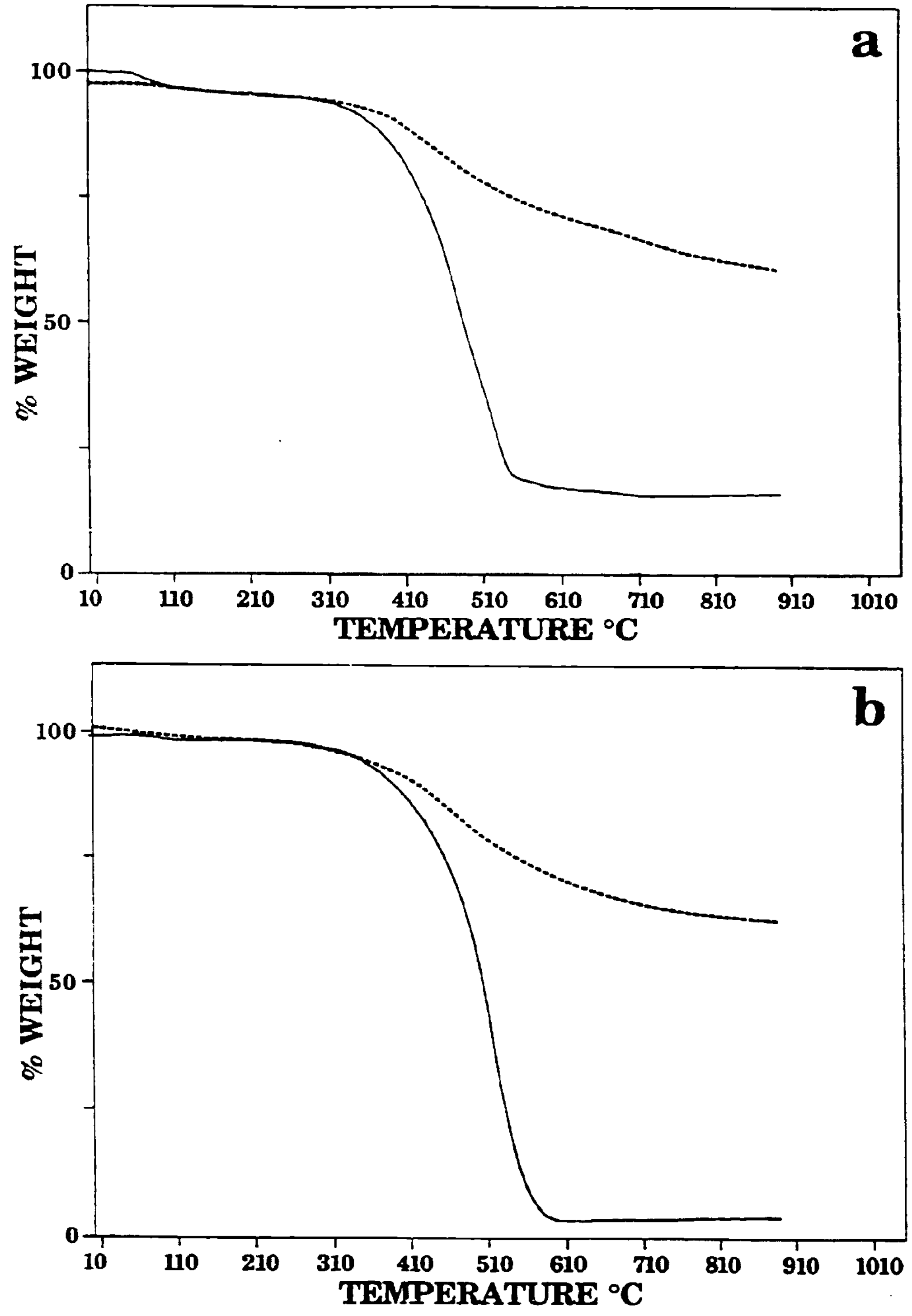

Figure II.C-12. TGA Weight Loss for a) Rosebud Subbituminous Coal and b) Demineralized Rosebud Subbituminous Coal. Solid Lines are Weight Loss in Air, Dashed Line in N_2.

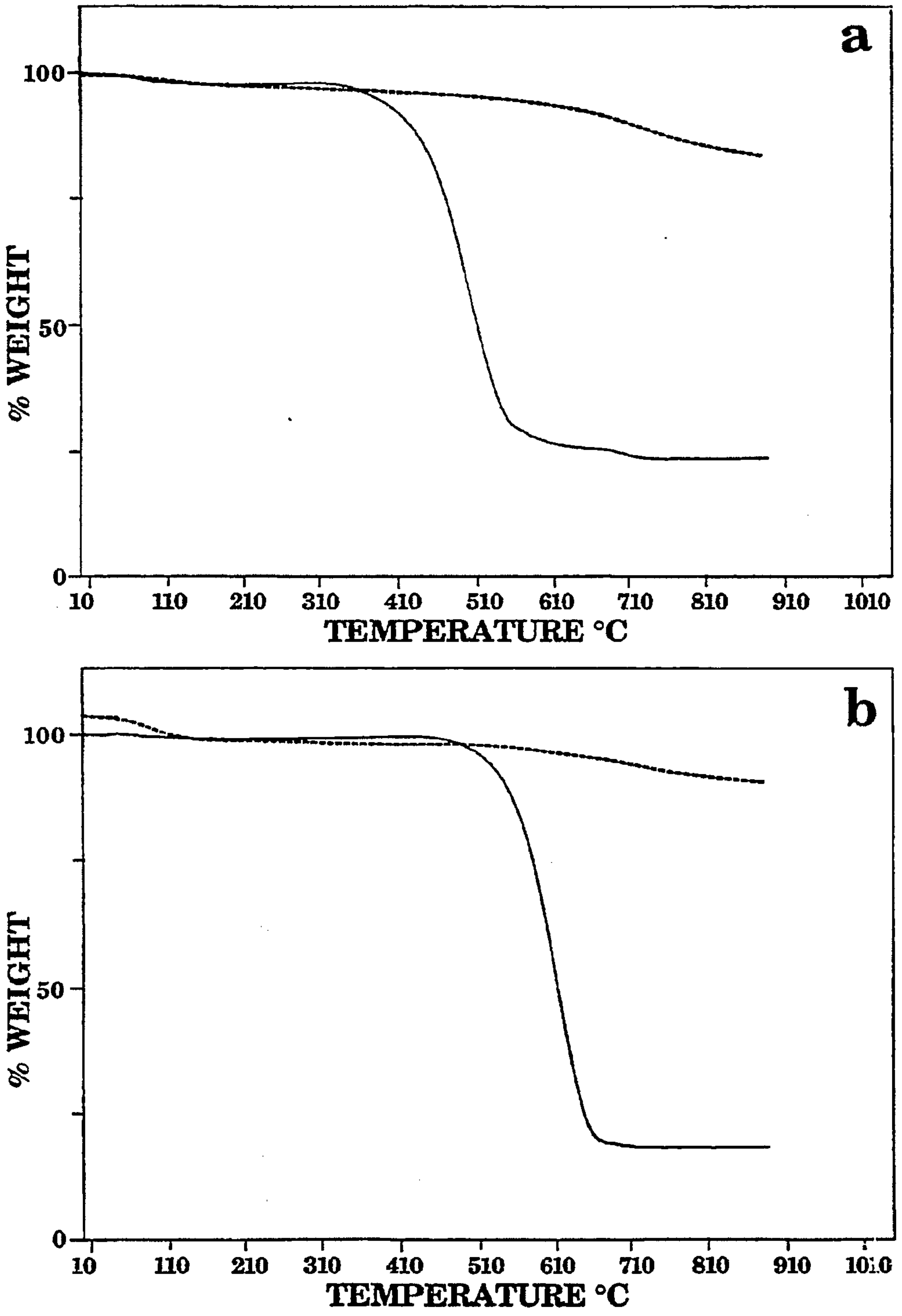

Figure II.C-13. TGA Weight Loss for a) 900°C EFR Rosebud Char and b) 1500°C Rosebud Char. Solid Lines are Weight Loss in Air, Dashed Line in N_2.

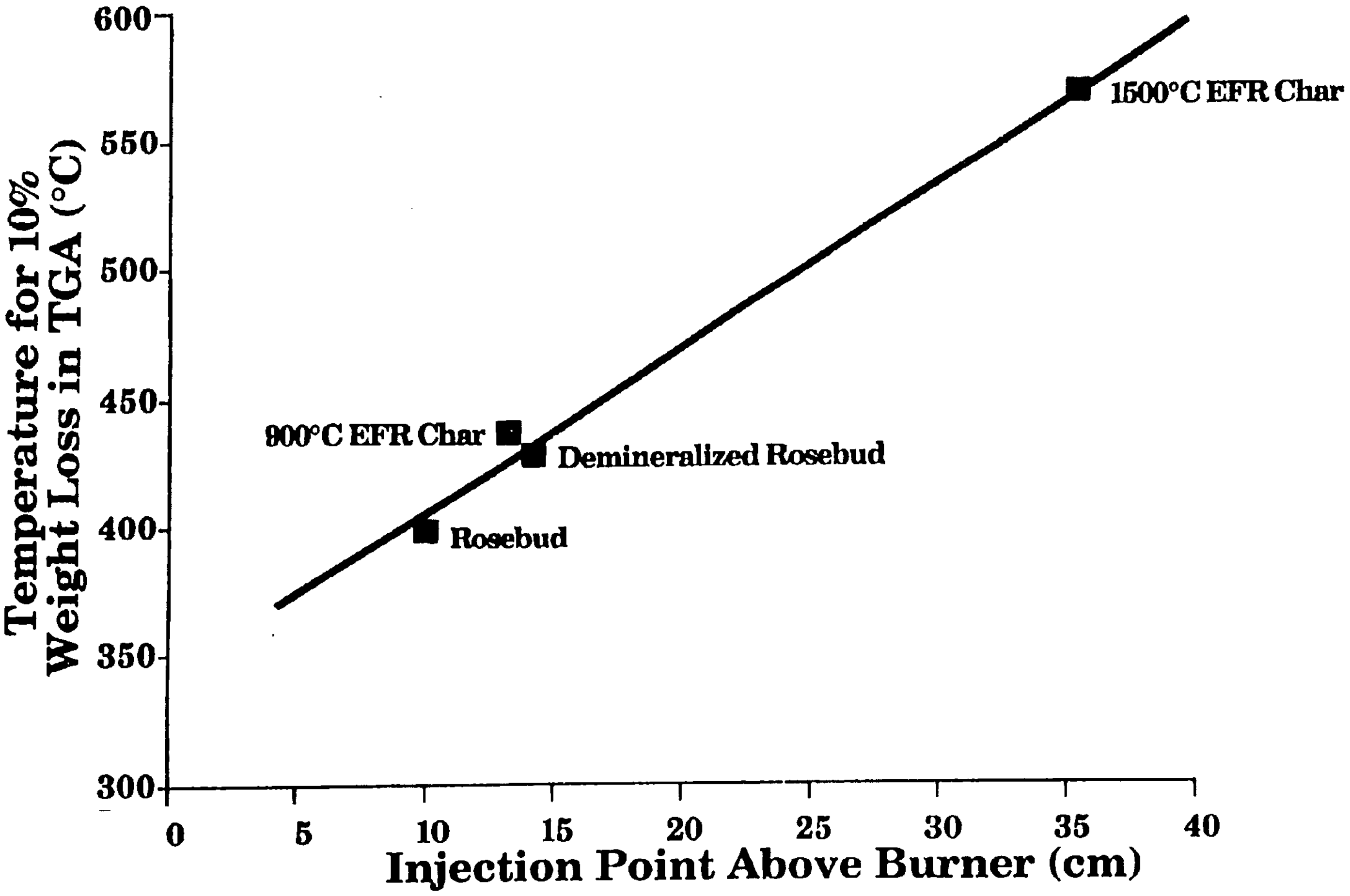

Figure II.C-14. Correlation of Ignition Point with Temperature for 10% Weight Loss Measured in TGA with Air.

TABLE II.C-6

TGA ANALYSIS OF COMBUSTION SAMPLES

Sample	Ignition Point (cm)	Temperature for 10% Weight Loss in Air (°C)	in N_2(°C)
Rosebud Subbituminous Coal	10	397	440
Demineralized Rosebud	14	430	440
900°C Char in EFR	13	437	760
1500°C Char in EFR	35	570	900

For the raw coal, there is a contribution to the weight loss from heterogeneous oxidation which shifts the weight loss curve about 30°C lower. This sample also ignites lower down. It therefore appears that the ignition may be influenced by both heterogeneous and homogeneous processes. Both processes may occur just prior to the rapid jump in temperature. At the bottom of the flame, however, the photographic record indicates homogeneous combustion processes as was observed for the demineralized coal.

New Ignition Phenomenon Observed

A new ignition phenomenon has been observed in the TWR. The phenomenon is shown in Figs. II.C-15 and II.C-16, which shows ignited particles traveling upward. The particles of interest are those at the edge of the particle stream which have contacted the hot pretreated gas stream. They ignite and appear to burn on the particle surface, as indicated by the fact that the flame width is roughly that of a particle. The particles get hotter with increasing distance.

The new ignition phenomenon occurs after the burning particles have burned for a short time. Under these conditions we often observed a secondary ignition event. This event has the following characteristics.

1. The dimension of the second flame zone increased to about 3 times the original dimension.

2. The second flame appears to be hotter than the original.

3. The second flame often ends with particle fragmentation suggesting burnout of the char.

4. The duration of the flame is on the order of a few msec.

5. The flame appears to oscillate or spiral around the particle in almost all cases.

The effect has been observed for chars as well as coals so is not associated with volatiles. The effect has been observed for demineralized coals so is not a mineral effect.

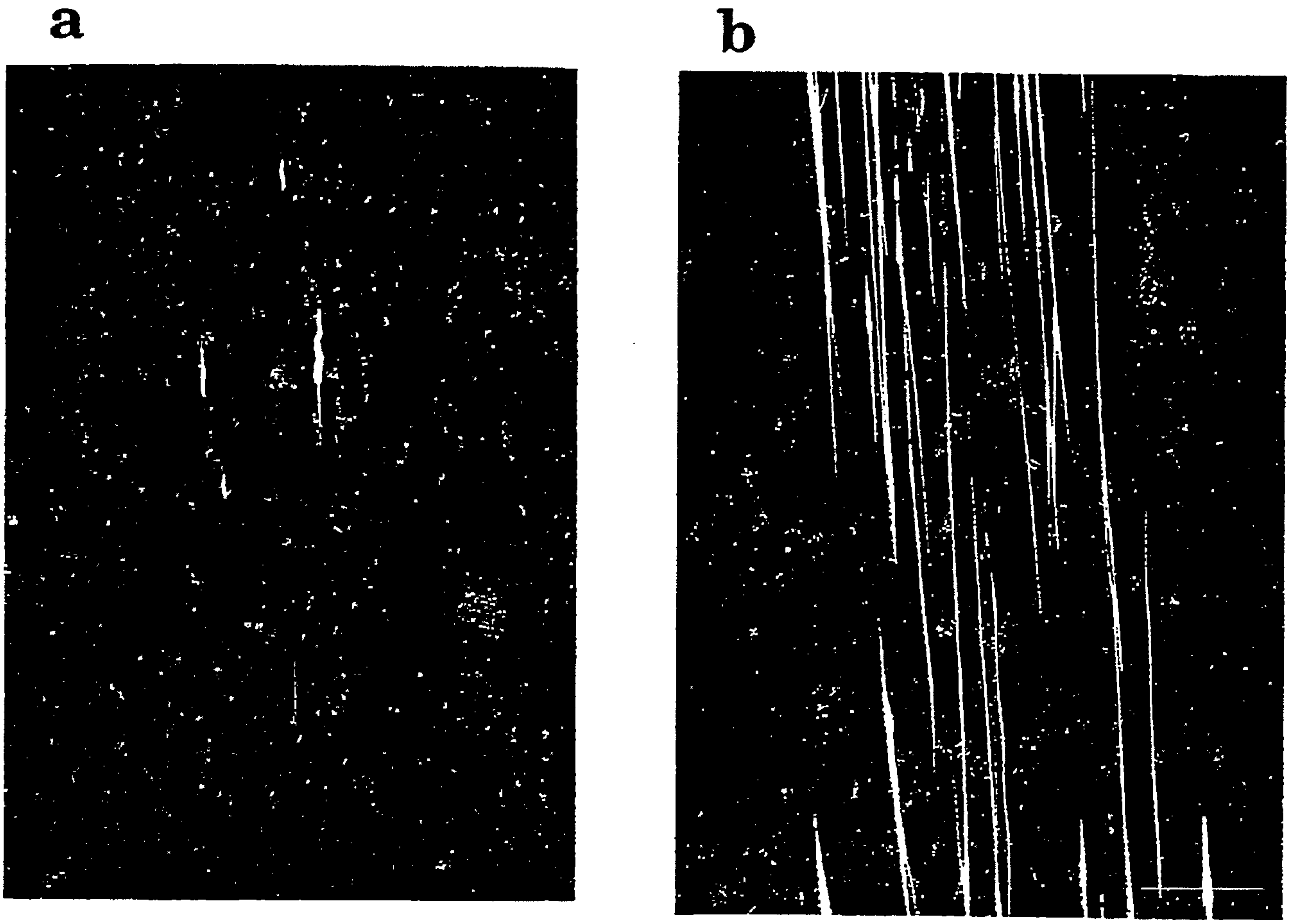

Figure II.C-15. Secondary Ignition Observed for Coal and Char.

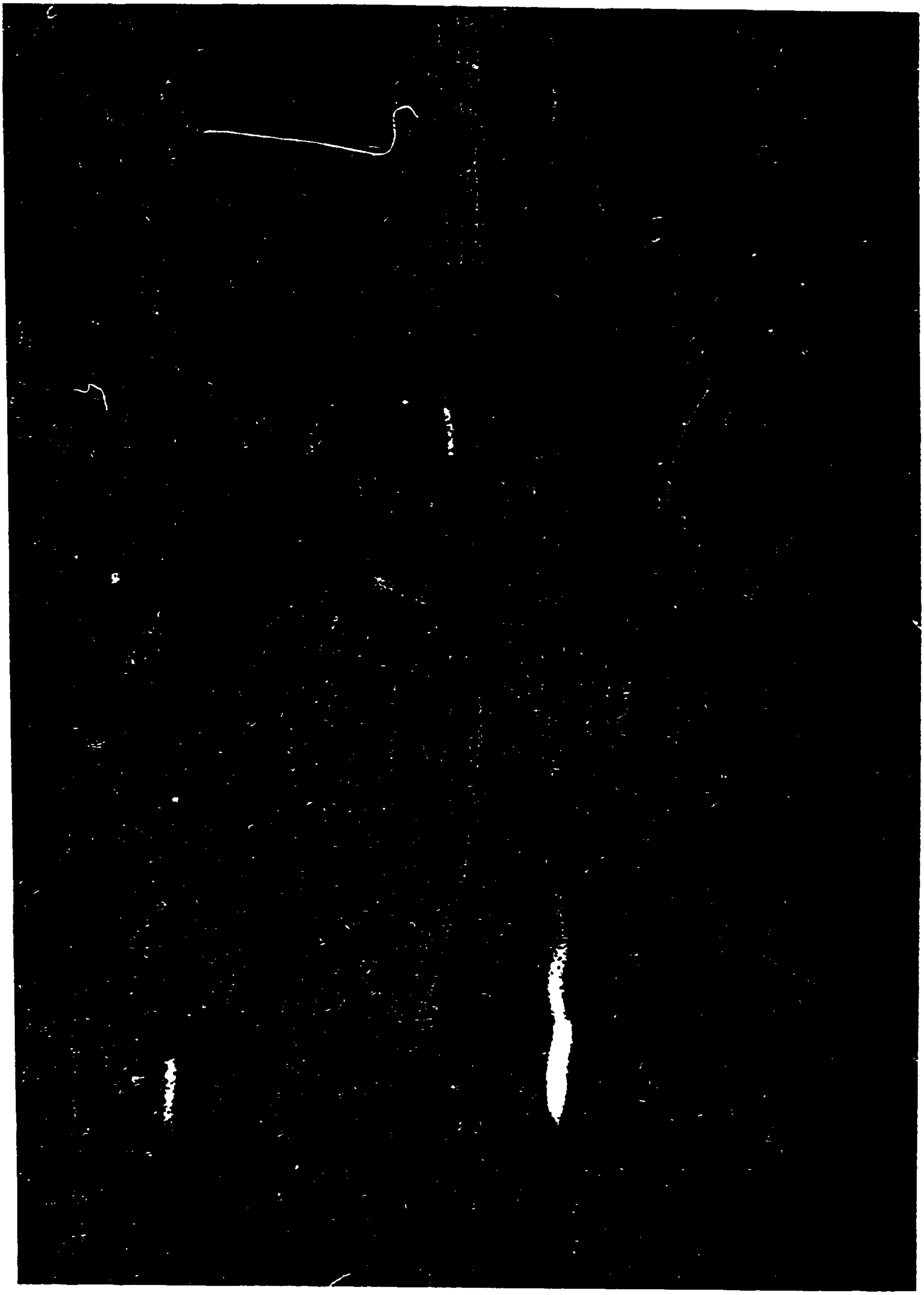

Figure II.C-16. Enlargement of Fig. II.C-15a, showing Oscillating or Spiral Flame Around the Particle Track.

One possibility is that the flame results from CO burning in a sheath surrounding the particle rather than well away from the particle. This would transfer the heat from the $CO \rightarrow CO_2$ flame back to the particle and result in a more intense flame with the possibility of more rapid burnout. However, this mechanism requires that the chief heterogeneous reaction be CO_2 gasification on the coal particles surface. The higher temperature may make this slower reaction possible.

No explanation has, however, been devised to explain the oscillations. This phenomenon will be subjected to further investigation.

Plans

A set of coals (raw and demineralized) and chars being made in the entrained flow reactor will be fed into the TWR for measurement of ignition distance and ignition temperature. In these experiments we plan to correlate our low temperature TGA measurements of reactivity with measurements made under gasification conditions in the TWR. The investigation of secondary ignition phenomenon will be continued.

II. SUBTASK 2.d. - ASH PHYSICS AND CHEMISTRY SUBMODEL

Senior Investigator - Michael A. Serio
Advanced Fuel Research, Inc.
87 Church Street, East Hartford, CT 06108
(203)528-9806

Objective

The objective of this task is to develop and validate, by comparison with laboratory experiments, an integrated and compatible submodel to describe the ash physics and chemistry during coal conversion processes. AFR will provide the submodel to BYU together with assistance for its implementation into the BYU PCGC-2 comprehensive code.

To accomplish the overall objective, the following specific objectives are : 1) to develop an understanding of the mineral matter phase transformation during ashing and slagging in coal conversion; 2) To investigate the catalytic effect of mineral matter on coal conversion processes. Emphasis during Phase I will be on the acquisition of data which will be utilized for model development in Phase II. Data acquisition will be focused on: 1) design and implementation of an ash sample collection system; 2) developing methods for mineral characterization in ash particles; 3) developing methods for studying the catalytic effect of minerals on coal gasification.

Mineral matter in coal is a source for slagging and deposits on reactor or down stream component walls, causing corrosion of equipment. Minerals can also catalyze reactions or can poison processing catalysts. The objective of this research is for the development of a model for the prediction of ash behavior and the correlation of the behavior with the original chemical composition, particle size, physical properties of the minerals and the process conditions. A model will also be developed to predict the catalytic effect of minerals on coal conversion.

Accomplishments

During the first year, a literature search was performed to identify the important effects of coal minerals in gasification. Meetings were also held with researchers at other institutions engaged in mineral matter research (Physical Sciences, Inc., IGT and University of North Dakota Energy Research Center, UNDERC). Work was also performed on designing the methods for ash collection and analysis and on analysis of the minerals in the coal sample set.

Literature Review

Literature reviews were presented in the second and third quarterly reports and will not be repeated here. The critical issues which have been presented in the literature and which will be addressed in this program are presented below.

The Physical Transformation of Minerals

Volatilization and chemical interaction of mineral matter are particularly important during coal conversion. The formation of slag and deposits of minerals depends on the particle size, its chemistry, and its physical-chemical behavior during coal conversion processes. Most of the work done in the area of predicting slagging and fouling behavior of ash of a pulverized coal has been based on the mean ash composition of the whole coal. Improvements will require predictions based on the composition as a function of the ash particle size distribution.

The literature indicates that the fly-ash derived from the transformation of the mineral matter in coal during combustion is bimodally distributed with respect to particle size. The large particle size (10 to 50 microns) correspond to the mineral residue from single coal particles. Particles within the submicron size range are formed from the vaporization and subsequent condensation of the volatile fraction of the mineral matter. Particles in the intermediate range, 0.5 to 10 microns, are generally formed from coagulation of submicron particles, from ash formed after char fragmentation or from ash particles released from the char particle surface during combustion. A methodology is required to determine the mineral composition distribution in coal from which the behavior of the ash formation in coal conversion may be predicted.

Most of the work done in this area has been carried out under a combustion environment. Very little work has been done under gasification conditions. The objective of this work is to determine the ash size distribution, ash transport ash radiative properties and the potential for slagging and for fouling in gasification reactors.

Catalytic Effects of Minerals

The presence of the inorganic minerals can either facilitate or impede coal gasification: The alkali, alkaline earth and some transition metals may have a catalytic effect on the gasification process. The organically bound metals are particularly active because they are dispersed on an atomic level. Some inorganic compounds such as sulfur can prevent gasification by poisoning the catalyst, whereas silicon oxide can convert the alkali and other metals to silicates and become inert for catalytic effects. A methodology is required which determines the mineral size and composition distribution so that the behavior of individual particles may be predicted for their catalytic effect during gasification or combustion.

The catalytic effect of minerals on both gasification and combustion have been reported. For example, a correlation between char reactivity and the amount of calcium present in the char has been established. The addition of calcium to char by ion exchange has shown an increase of the reactivity linearly with an amount of calcium added. Some studies also showed that the removal of the mineral components of the coal by acid treatment lead to a decrease in char activity. However, with coals of high rank the reverse effect was observed, probably as a result of an increase in the surface area and porosity on the demineralization. The addition of iron, by impregnation, also increases the activity of the coke in steam gasification. It is generally concluded that in the presence of mineral matter, the catalytic effect is dependent upon the concentration and dispersion of inorganic species which act as specific carbon gasification catalysts. However, the minerals in coal have also some undesirable effects. In catalytic coal gasification, the original mineral content in coal has sometimes been shown to reduce the catalyst performance when the added catalyst reacts with the minerals to form a new less catalytic phase.

Work needs to be undertaken to predict the catalyst behavior of minerals of coal and its interaction with added catalysts, based on it composition, particle size and distribution.

Ash Fouling, Slagging and Corrosion

Most of the work on ash slagging and fouling has been done under combustion conditions. This work is being considered as background for the corresponding processes in gasification.

In pulverized-coal boilers the mineral matter in the coal is released into the furnace gases as fly ash and vapors. This material may form insulating and corrosive deposits on the heat transfer surface. The process of deposit initiation and growth usually involves either liquids formed on the tube, such as condensed alkalis ('sticky tube mechanism'), or low viscosity super cooled impinging fly ash particles ('sticky particle mechanism'). It is proposed that this low viscosity material may be provided by an alkali-enriched surface layer, formed by an alkali-ash reaction in either the char or the furnace gases. The ash particles whose outer layer is enriched in sodium may readily wet the heat transfer surface, allowing rapid bond formation due to the dissolution of the surface iron oxide at the particle surface.

Some empirical correlations have been established between the slagging behavior of a coal with such properties as viscosity of the coal ash, temperature of the critical viscosity, fusion temperature and surface tension. Empirical factors such as the slagging factor, fouling factor, dolomite percentage, ferric percentage and base-to-acid ratio have been devised. These indices of slag behavior are based on tests of the mean coal ash and do not treat the effects of individual ash components which may be the "bad actors".

Experimental Study Of Mineral Matter Transformation

The objective is to determine mineral transformation in the reactor, its radiative properties, its potential for slagging and fouling of the reactor, and its catalytic effect on gasification or combustion.

Experimental Methods

1. Samples of coal will be reacted in the entrained flow reactor (EFR), transparent wall reactor (TWR), and TG-FTIR.

2. Experimental methods, similar to the procedures described in the literature (Neville and Sarofim, 1985) for ash particle collection have been designed and implemented. The ash sample collection system consists of an Andersen Model Mark III, eight stages stack sampler and a cyclonic preseparator. During the sample collection, all particulate products from the burner are continuously collected and quenched by a water-cooled collection probe. From the probe, the ash particle enter a cyclonic preseparator for separating larger particles, the remainder enter the cascade impactor for aerodynamic size classification. Depending on the gas flow velocity and temperature, eight discrete particle size cuts can be obtained. For example, in a given set of

conditions of temperatures at 300°F and flow rate at 0.6 ACFM, eight discrete size cuts with mean diameters of 13.6, 8.6, 5.6, 4.0, 2.5, 1.3, 0.8, and 0.54 μm will be obtained. The submicron particle (<0.54 μm) generated by the vaporization and subsequently condensation of ash, pass through the impactor for collection and isolation on a back-up glass fiber filter.

3. Techniques have been selected for measuring solid and vapor species concentration for inorganic constituents. For example, quartz, kaolin, calcite, and mixed clay in coal will be analyzed by transmission FT-IR. The inorganic minerals will be analyzed by a coal microanalyzer which uses an electron beam to excite characteristic x-rays from mineral components. The correlated spatial distributions for elements, Na, Mg, Al, Si, K, Ca, Ti, Fe and S, can be obtained. Methods for studying vapor phases of inorganic species by using FT-IR will be explored.

Analysis of the bulk and discrete size ash particle's chemical and physical properties will be performed. Chemical compositions will be obtained by x-ray, SEM, density, porosity, surface area, viscosity, etc.

4. Temperature measurements of the char particles in the TWR will be made using FT-IR E/T spectroscopy. This method has been demonstrated successfully by AFR.

5. The interaction of minerals with known additives during ash particle formation will be determined. The fate of added minerals, such as Na, K, Ca, will be examined by tracing their distribution in different particle size ranges.

6. The catalytic effect of minerals as compared with the demineralized coal will be determined, and their gasification rates for different coal ranks measured.

7. The effect of operation conditions, e.g. temperature, flow rate, pressure, oxygen concentration, on ash behavior and gasification performance will be measured.

8. The correlation between mineral content and fouling and slagging, combustibility and gasification rate will be developed.

Elemental Analysis of Coals by SEM/Dispersive Energy X-Ray

The elemental composition of the minerals in the ampoule coal samples was characterized by a Scanning Electron Microscope (SEM) with dispersive energy x-ray analysis. The samples are received in glass ampoules under an inert gas blanket and analyzed on an as received basis without further treatments. The particle size of coal samples are -100 mesh for 5 gm ampoules and -20 mesh for 10 gm ampoules. All the coals except for the Wyodak samples are in the -100 mesh size. All the raw coal samples were reground into very fine particles using a ball-mill for 20 minutes and then pressed into a flat pellet containing about 300 mg of coal to ensure a representative sample is obtained. The samples are coated with graphite to prevent charging problems and then the resulting pellet is mounted in the SEM. The analysis of the elemental composition is based on the measurement of the x-ray intensities of the major elements (Fe, S, Ca, Ti, Mg, Na, Sl and Si) from 121 subsamples, where a subsample is a small surface portion of the sample (typically 20 to 200 microns square). The electron beam is scanned from one subsample to another, and the x-ray intensities for all elements of interest are recorded. The data acquisition process is completely automated and takes about 10 minutes.

In order to compare the obtained elemental analysis of coal mineral impurities with the ASTM high temperature ashing sample measurements, the elemental compositions of the coals are recalculated and converted into the oxide form (MgO, Na_2O, Al_2O_3, SiO_2, K_2O, CaO, TiO_2 and Fe_2O_3). The amount of SO_3 calculated in the ash are only those portions which are scrubbed by the CaO to form $CaSO_4$. Therefore, the total number of moles of SO_3 present in the ash will not exceed the total number of moles of CaO presented in the coal. The excess amount of sulfur analyzed in raw coal samples will be assumed to be released into the gas product stream during the coal conversion process. The iron content in the elemental composition are only including the iron in oxide from. Therefore, the total iron contents have been recalculated to include the iron existing in the pyrite form, based on the relative stoichiometry ratio.

The results of the mineral impurities analysis and other characteristics of raw coals are shown in Tables II.D-1 to II.D-3. Table II.D-1 shows the ultimate, proximate and sulfur forms analysis of all raw coal samples. Most of these data are provided by Argonne, except the sulfur content and form which were analyzed at AFR. Argonne's data are also listed for comparison. The agreement is good in most cases. Table II.D-2 shows the results of mineral elemental composition

Table II.D-1. Properties of Coals to be used in Mineral Transformation Testing.

	Upper Freeport bituminous	Wyodak subbituminous	Illinois No.6 bituminous	Pittsburgh No.8 bituminous	Pocohontas No.3 bituminous	Utah Blind Canyon bituminous	Upper Knawha bituminous	North Dakota Zap lignite	Montana Rosebud subbituminous
Proximate Analysis, wt%									
Moisture	0.83	28.84	2.94	1.80	0.61	4.71	2.60	32.84	---
Volatile Matter	27.56	33.95	30.92	---	---	---	---	---	---
Fixed Carbon	58.56	30.84	42.72	---	---	---	---	---	---
Ash	13.05	6.37	23.42(16.2)++	9.27	4.87	4.68	19.81*	6.53**	---
Ultimate Analysis, wt%,maf									
C	87	74	77	83	91	79	81	73	72.1
H	5.5	5.1	5.7	5.8	4.7	6.0	5.5	5.3	4.9
S**	2.8	0.5	5.4	1.6	0.9	0.5	0.6	0.8	1.2
N	1.4	1.3	1.2	1.5	0.9	1.3	1.0	0.5	1.2
O	4	19	10	8	3	13	11	21	20.3
Forms of S, wt%*+									
Inorganic	0.65(1.96)	0.29(0.14)	2.58(2.72)	1.38(1.33)	0.06(0.18)	0.14(--)	0.25(--)	0.27(--)	1.60(--)
Organic	0.71(0.49)	0.45(0.42)	1.90(2.08)	0.70(0.81)	0.50(0.42)	0.24(--)	0.48(--)	0.45(--)	0.47(--)
Total:	1.36(2.46)	0.74(0.56)	4.48(5.03)	2.08(2.14)	0.56(0.60)	0.38(--)	0.73(--)	0.72(--)	2.07(--)

Notes:

** Moisture free basis
* Analyzed by SEM/dispersive energy x-ray technique of raw coals on a dry basis.
\+ Values in parenthesis represent Argonne's data on a dry basis.
++ Value from a second laboratory

Table II.D-2. Mineral Distribution, Elemental Composition.

Metal	Upper Freeport	Wyodak	Illinois No.6	Pittsburgh No.8	Pocahontas No.3	Utah Blind Canyon	Upper Knawha	North Dakota Lignite	Montana Rosebud
Na	0.03	0.11	0.12	0.02	0.07	0.08	0.11	0.36	0.02
Mg	0.22	0.37	0.16	0.13	0.11	0.11	0.33	0.54	0.35
Al	1.67	0.73	1.35	0.94	0.57	0.3	3.57	0.49	1.08
Si	2.92	1.12	2.88	1.72	0.69	0.49	5.47	0.82	0.49
K	0.24	0.02	0.16	0.07	0.02	0.03	0.42	0.03	0.03
Ca	0.19	1.3	0.71	0.16	0.26	0.28	0.08	1.56	1.17
Ti	0.11	0.09	0.07	0.01	0.05	0.01	0.26	0.05	0.07
S(o)	0.71	0.45	1.9	0.7	0.5	0.24	0.48	0.45	0.47
S(m)	0.65	0.22	2.58	1.38	0.06	0.14	0.25	0.27	1.6
Fe	0.47	0.29	0.6	0.3	0.28	0.14	0.47	0.4	0.32
Ash	12.49	9.02	16.14	8.51	4.4	3.41	21.48	9.6	12.33

Table II.D-3. Mineral Distribution in Raw Coal Ash (oxide form).

Metal	Upper Freeport	Argonne's Data	Wyodak	Argonne's Data	Illinois No.6	Pittsburgh No.8	Pocohontas No.3	Utah Blind Canyon	Upper Knawha	North Dakota Lignite	Montana Rosebud
Na_2O	0.32	0.44	1.67	2.15	1.01	0.32	2.19	3.28	0.69	5.35	0.22
MgO	2.93	1.07	6.90	6.11	1.66	2.53	4.24	5.54	2.55	9.86	4.67
Al_2O_3	25.33	23.97	15.50	17.26	15.98	20.88	25.05	17.23	31.48	10.20	16.43
SiO_2	50.16	42.82	26.93	32.91	38.60	43.27	34.34	31.87	54.63	19.33	25.68
K_2O	2.71	2.46	0.32	0.33	1.41	1.16	0.66	1.29	2.76	0.47	0.34
CaO	2.13	4.60	20.44	21.81	6.22	2.63	8.46	11.91	0.52	24.04	13.18
TiO_2	1.47	1.02	1.69	1.29	0.73	0.20	1.94	0.51	2.02	0.92	0.94
SO_3	3.04	1.32	18.82	10.69	8.88	3.75	12.07	16.99	0.75	19.83	18.81
Fe_2O_3	11.89	21.35	7.74	6.77	25.50	25.25	11.05	11.38	4.59	10.00	19.73
Total:	100.00	99.05	100.00	99.32	100.00	100.00	100.00	100.00	100.00	100.00	100.00
Ash	12.46	13.03	8.9	8.83	15.97	8.51	4.30	3.29	21.43	9.08	12.42

analyses by SEM/dispersive energy x-ray analyses of nine raw coals. Table II.D-3 shows the similar results of Table II.D-2 but expressed in the oxide form in the ash and a comparison of the results of HTA samples analyses provided by Argonne. The two methods show reasonable agreement.

When comparing the ash composition data obtained from AFR with Argonne's data, good agreement is found for the total ash content. For example, our data for the ash content of Upper Freeport bituminous and Wyodak subbituminous coals were 12.46 and 8.9 wt%, respectively, as compared with 13.03 and 8.83 wt% obtained from Argonne for these two coals. However, some discrepancies were observed for the sulfur and iron content. This may be due to our assumption that the CaO will scrub equivalent stoichiometric amounts of SO_3. In the real ashing procedure, this may not be the case.

Ash Collection

The ash produced during combustion in the Transparent Wall Reactor (TWR) has been collected using a cascade impactor for Montana Rosebud subbituminous coal. All gaseous and particulate products of combustion are continuously collected and quenched by a water cooled collector probe (which was set 72 inches above the head of the heated furnace). The gas flow rate used for the impactor was about 21 l/min which represents the flow rate of the vacuum pump applied on the exit end of the impactor. Initially, a home made cyclone was used as a preseparator to collect the particles larger than 10 μm. However, this cyclone was found to be too powerful to use because it will collect more than 95% of all the ash. Therefore, no preseparator was used in the first few experiments for ash collection. From the water cooled probe, the products enter directly into a cascade impactor for aerodynamic size classification of ash particles. The submicron size particles, generated by the vaporization and subsequent condensation of ash, pass through the impactor for collection and isolation on a backup glass fiber filter. The coal feed rate was 1.8 gm/min. The coal particle size was 200 x 375 mesh. A typical collection time was 10 minutes.

Portions of the fractionated ash particles of the combusted Montana Rosebud coal have been analyzed by SEM/dispersive x-ray analysis. The microscope image examination of the particulates collected on first stage is shown in Fig. II.D-1. In this figure, the cenosphere particles and the aggregates of small particles are present. The aggregates contain several primary particles agglomerated together. The primary particles contain 10 or so 10-50 μm units. The size of

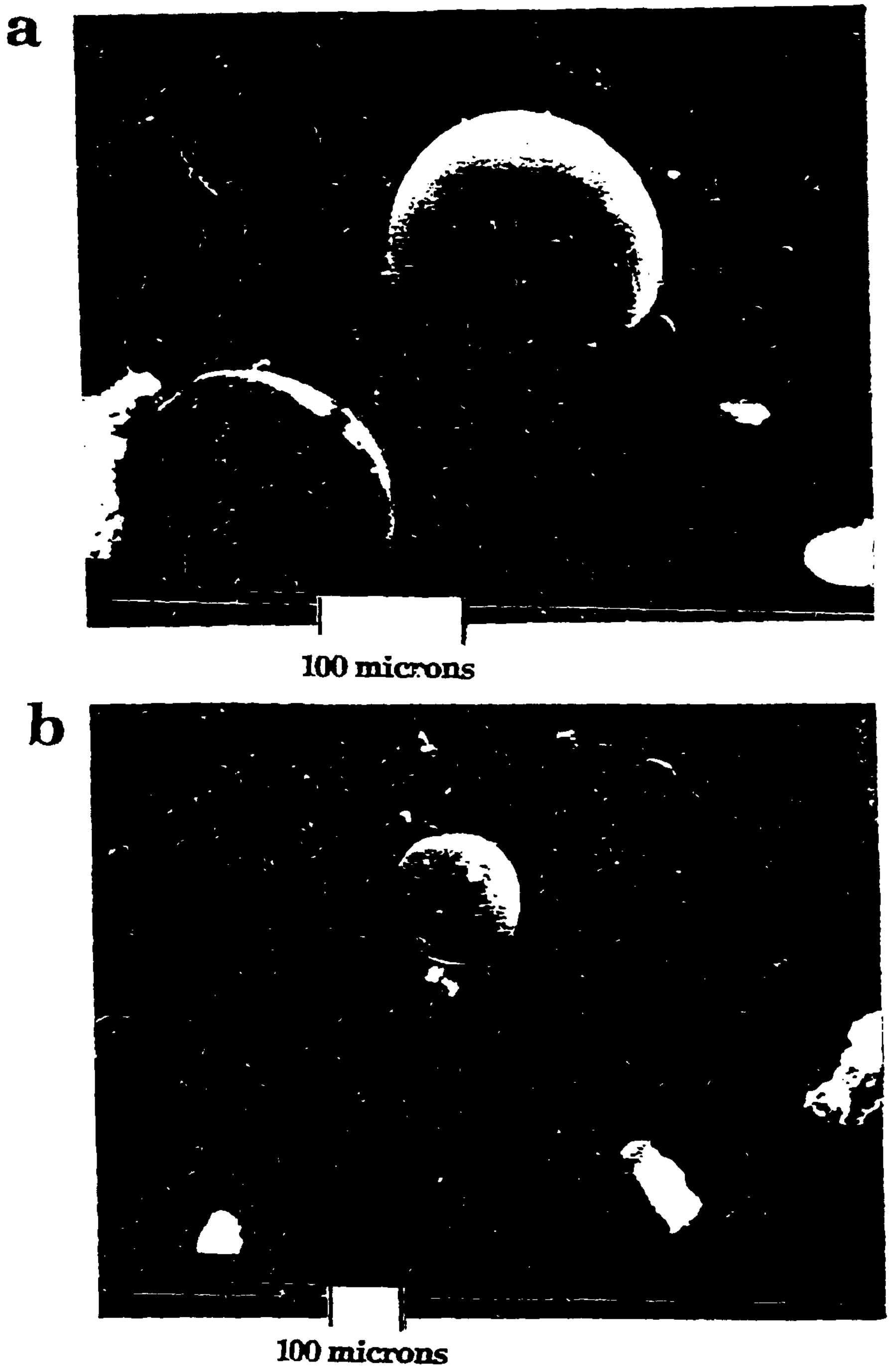

Figure II.D-1. SEM Photograph of Combustion Ash of Montana Rosebud Coal. a) 200X Magnification and b) 100X Magnification.

the cenosphere particles was about 40-80 μm O.D. Under the microscope, these cenospheres are shown as a red transparent glassy ball indicating that iron oxides are incorporating into the fused glassy silicates.

Based on the SEM/dispersive energy x-ray analysis, these cenospheres contain a very high content of SiO_2 and CaO, (43.14 and 37.57 wt%, respectively) (Table II.D-4). The decrease of silicon oxide content from 41.2 wt% in first stage particles to 31.4 wt% in third stage particles indicate that the large particles are basically formed by fused silicated glassy material which coagulated with the other fused materials at the combustion temperature. The iron content in these particles also followed a similar trend as for silicon. However, the sulfur content appeared to increase as the ash particle size decreased. These results are consistent with the observations made by Desrosiers et al. (1978). The formation of cenosphere particles are probably due to the expansion of the encaptured gas in the fused ashes during the combustion process. The results of a detailed analysis of the ash particles collected in each stages will be presented in subsequent quarterly reports.

Char Reactivity vs Mineral Content

As discussed earlier, the presence of certain minerals in char will enhance the char reactivity. The degree of the enhancement of the char activity will depend upon the mineral concentration and size distribution. The reactivity of char can be measured in a TGA by its critical temperature (T_{cr}) in the non-isothermal test. The critical temperature varies inversely with char reactivity. Thus a plot of critical temperature of char vs the mineral content will give an indication of the direct involvement of the minerals in the char gasification process. In Fig. II.D-2, the Ca and K content of the coals is plotted vs the critical temperature of chars produced from the nine coal samples. All of the nine chars were prepared by heating the raw coal in a nitrogen flow to 900°C with a 30°C/min heating rate. The reactivity measurements were carried out in a TGA in air with a heating rate of 30°C/min up to 900°C. A good correlation of the Ca concentration vs T_{cr} is demonstrated in this plot (open squares). The numbers shown on this plot indicate the sample number listed on Table II.A-1. These data demonstrate that the high rank coals, which have lower calcium contents, all show a low char reactivity. When potassium is added to the calcium (closed squares) the correlation is slightly improved. Coal No. 7 now falls on the correlation. This suggests that both alkali metals are important although Ca is usually more abundant.

Table II.D-4. Ash Analysis of Combustion Ash[*] of Montana Rosebud Coal

Oxide	Raw Coal	1st Stage[+]	Cenosphere[**]	3rd Stage[+]
Na_2O	0.22	0.243	0.070	0.040
MgO	4.67	0.681	0.073	5.215
Al_2O_3	16.43	13.585	7.360	18.444
SiO_2	25.68	41.160	43.142	24.538
K_2O	0.34	0.346	0.443	0.648
CaO	13.18	24.101	37.577	31.425
TiO_2	0.94	1.991	1.137	1.881
SO_3	18.31	3.066	2.883	5.639
Fe_2O_3	19.73	14.828	7.316	12.168
Ash	12.42	100.00	100.00	100.00

[*] Ash collected from a cascade impactor containing nine jet plates.

[**] These data represent the x-ray analysis which focused the x-ray beam on a cenosphere particle of the ashes collected from the first stage collection plate of a cascade impactor. The ash particle was not reground.

[+] Ash particles collected from first and third collection plates of a cascade impactor. The ash samples were reground before mounted on the sample stub for SEM/x-ray analysis. The first and third stage particle samples represent a particle size range of > 10 and ~ 4.6 μm, respectively.

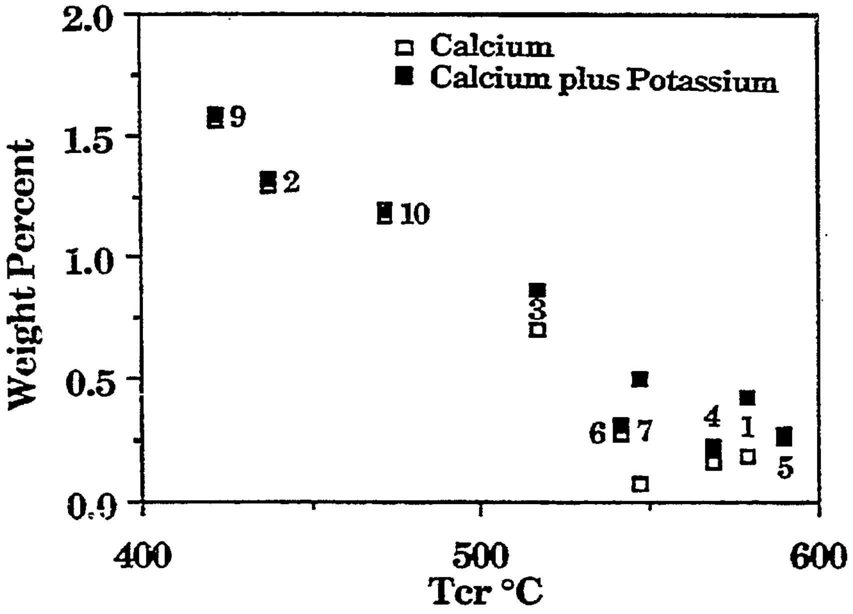

Figure II.D-2. Reactivity vs. Calcium and Potassium Content in Raw Coal.

Plans

Continue the combustion and collection of ash particle for all coals in the TWR reactor for aerodynamic particle size classification using a cascade impactor. Characterize the ash particles of different size ranges. The mineral content analysis will be performed by using SEM/dispersive energy x-ray technique. The mineral size distribution analysis will be performed by using the SEM. The mineral forms will be identified by correlation of the subsamples. These data on mineral size distribution and composition will be correlated with the initial mineral distribution within the particle. A device for measuring the ash sticking behavior will be designed and implemented in the TWR reactor for monitoring the fouling and slagging behavior of ashes of different ranks of coal.

II.E. SUBTASK 2.e. - LARGE PARTICLE SUBMODELS

Senior Investigator - Michael A. Serio
Advanced Fuel Research, Inc.
87 Church Street
East Hartford, CT 06108
(203) 528-9806

Objective

The objectives of this task are to develop or adapt advanced physics and chemistry submodels for the reactions of large coal particles (> 0.5 mm) and to validate the submodels by comparison with laboratory scale experiments. The result will be coal chemistry and physics submodels which can be integrated into the fixed-bed (or moving-bed) gasifier code to be developed by BYU in Subtask 3.b. Consequently, this task will be closely coordinated with Subtask 3.b.

Accomplishments

A literature review of heat and mass transport effects in coal pyrolysis continued as part of the work being done for this subtask. A critical evaluation was made of models that have been used to describe intraparticle heat transfer during pyrolysis. Since mass transfer effects are well covered in the review by Eric Suuberg (see Appendix A in the Second Quarterly Report), this review has focused primarily on heat transport processes. In addition, calculations were done to define regimes of internal and external heat and mass transport control for conditions of interest. This was to determine the boundary regions where such considerations become important. Finally, a review was made of previous work on fixed-bed pyrolysis experiments in preparation for our own experimental effort.

Heat and Mass Transport Effects in Coal Pyrolysis

Introduction - Given the large particles used in fixed-bed gasifiers, it is likely that transport effects nearly always play a role. However, it is also true that at the very high heat fluxes encountered in some gasification and combustion processes, gradients may be important for particles in the pulverized fuel range. Consequently, the review was not strictly limited to large (> 0.5 mm) particles since what constitutes a "large" particle will depend on the experimental conditions.

The first objective was to examine previous experimental and modeling studies of heat transport. A close examination of this work indicated widely different assumptions about the values of coal physical properties and how these change with temperature and the extent of pyrolysis. Consequently, it was decided that a review of the literature on coal physical properties would also be necessary.

Review of Modeling Studies - Since much of the work on devolatilization in the last several years has included rapid pyrolysis of fine (pulverized) particles or slow pyrolysis of large particles, most pyrolysis studies and models have not been concerned with internal transport effects. However, with the relatively recent interest in pyrolysis under fluidized-bed or moving-bed conditions, where large (> 1mm) particles are pyrolyzed at relatively high heating rates (10 to 1000 K/s), the interest in internal transport has increased.

Models for simultaneous heat and mass transport for devolatilization have been developed by Mills et al. (1976) and James and Mills (1976) for plastic coals and by Devanathan and Saxena (1985, 1987) and Bliek et al. (1985) for non-plastic coals. Freihaut et al. (1977) and Agarwal et al. (1984a, 1984b) have developed coupled reaction and heat transport models for nonplastic coals.

Heat Transfer/Reaction Models - A model by Freihaut et al. (1977) considered the combined influence of heat transfer, heats of reaction and chemical kinetics on intraparticle temperature gradients during pyrolysis. Not many details of the model have been published in the open literature. Mass transfer effects were neglected.

Agarwal et al. (1984a) have developed a general devolatilization model for large non-plastic particles under fluidized bed conditions which includes coupled reaction and heat transfer. Good agreement was obtained for devolatilization times measured for Mississippi lignite. A simpler version was developed for the pure heat transfer control regime (Agarwal et al., 1984b). Neither version includes a treatment of mass transfer or secondary cracking effects.

Heat Transfer/Mass Transfer Reaction and Models - Workers at UCLA (Mills et al., 1976) developed a model for particles undergoing rapid pyrolysis which included a fundamental description of heat transport starting with the conservation equations. A consecutive reaction scheme, similar to that of Chermin and van Krevelen (1957) was used. The porosity of the particle was assumed to be governed by a foaming law and the particle was allowed to swell and shrink, accordingly.

The thermal conductivity was assumed to decrease linearly with the decrease in particle density. The model was primarily concerned with the variation in thermal response of a particle with the variation in parameters such as particle diameter, ambient temperature, heating rate, heats of reaction and activation energies. The equations were solved numerically by a finite-difference method. The model was successful in qualitatively describing many important features of coal pyrolysis, as shown in Figs. II.E-1 and II.E-2 for the effect of particle size on the instantaneous and cumulative gas evolution with time. Figure II.E-3 shows the effect of particle size on the average gas evolution rate. The kinetic control limit (no diameter dependence) is evident for the lowest ambient temperature (T_e = 972 K). For higher temperatures, the kinetic limit would only occur for particles smaller than 30 μm. The curves in Fig. II.E-3 approach the 45° slope for heat transfer control for the large particle sizes.

Mills et al. (1976) also evaluated the work of Peters and Berlting (1965), who injected 1000 - 1500 μm particles into a fluidized bed at temperatures ranging from 600 to 1100°C. They noted that the relatively weak diameter dependence observed by Peters and Berlting ($d_0^{-0.26}$) is evidence that the experiments were primarily controlled by chemical reactions and not dominated by heat transfer, as was suggested by Peters and Berlting.

The model of Mills et al. was improved in a later paper by James et al. (1976). In order to account for pressure and particle size effects, models were included to describe (1) the porous structure of a coal particle; (2) the flow of gases through voids and pores, and the resultant pressure distribution, (3) evaporation of tar species and (4) cracking of gaseous species as they percolate through the pores. Again, the qualitative predictions of the model were in good agreement with expectations, but this version of the model was never rigorously validated against experimental data.

Devanathan and Saxena (1985,1987) have developed a model which considers both heat and mass transfer effects for large nonplastic coal particles. The later version of this model was improved to include secondary cracking reactions of tar so that particle size effects could be predicted. The authors also included a sensitivity analysis which indicated that results were very sensitive to the assumed internal diffusivities for the volatiles species. The Thiele modulus (ratio of reaction rate/diffusion rate), the Lewis number (ratio of thermal diffusivity/mass diffusivity) and the heat transfer Biot number (ratio of internal to external heat transfer resistance) were identified as crucial parameters in

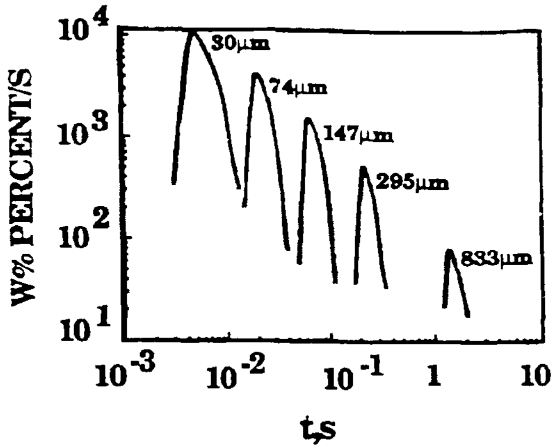

Figure II.E-1. Effect of Particle Size on Instantaneous Gas Evolution Rate. T_o = 303K, T_e = 1250K, Nu = 2.0, % V.M. = 40, ϕ = 45 from Mills et al. (1976).

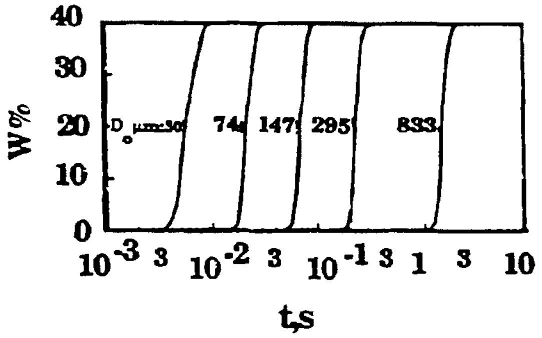

Figure II.E-2. Effect of Particle Size on Cumulative Gas Evolution. T_e = 1250K, Nu = 2.0, % V.M. = 40, ϕ = 45 from Mills et al. (1976).

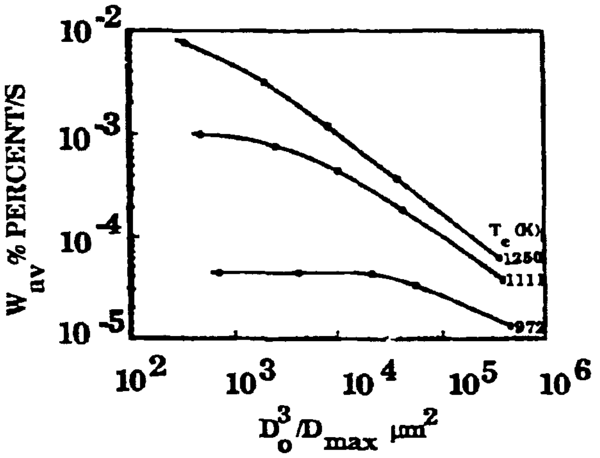

Figure II.E-3. Effect of Particle Size on Average Gas Evolution Rate. T_o = 303K, Nu = 2.0, % V.M. = 40, ϕ = 45 from Mills et al. (1976).

determining devolatilization times. One problem with analyses such as the one done by Devanathan and Saxena is that not much attention was paid to the choice of devolatilization parameters or the temperature dependence of physical properties like the heat capacity and thermal conductivity. They chose the kinetic parameters of Kobayashi et al. (1977) which have recently been shown by Jamaladdin et al. (1987) to severely underestimate devolatilization times.

A model which is as comprehensive as the one by Devanathan and Saxena has recently been developed by Bliek et al. (1985), also for non-plastic coals. This model includes transient devolatilization kinetics, intraparticle heat and mass transport, and secondary deposition of volatiles. Model predictions were made for variations in particle size, ambient pressure, and heating rate on the tar, gas and total volatile yield during devolatilization. The authors made comparisons to their own data and data from the literature and usually obtained at least qualitative agreement. However, the model has so many adjustable parameters that this agreement does not necessarily validate their assumptions about the controlling mechanisms. The authors did do a good job in attempting to account for the variations in physical parameters with temperature.

The models of Devanathan and Saxena (1985, 1987) and Bliek et al. (1985) appear to be the best starting point for developing a model for use in the current program since they include all of the relevant phenomena (heat transfer, mass transfer, kinetics). These models will be subjected to closer scrutiny during the next quarter.

Physical Properties - It was expected that there would be variations in the pyrolysis kinetic parameters chosen in different modeling studies. However, significant variations in assumed physical properties were also observed and variations in these properties with temperature and extent of pyrolysis are often neglected. A detailed evaluation of literature on the key physical parameters important in a heat transfer analysis was done.

This included consideration of data on specific heat, thermal conductivity, emissivity, density, and transpiration cooling. A wide variety of values was found, as shown in Table II.E-1. A summary of what is believed to be the best available data is being developed.

Heat Transfer Calculations - Calculations of the characteristic times for internal and external heat transfer were made for a 60 micron particle. A

Table II.E-1. Summary of Data Used in Some Pyrolysis / Heat Transfer Models.

Reference	Physical properties				Chemical Properties		
	Cp cal/gk	ρ g/cm^3	kp cal/s cmK	α cm^2/s	ΔHr cal/g	$k_{400°C}$ s^{-1}	$k_{800°C}$ s^{-1}
Mills et al. (1976)	0.35	0.67	$1.6x10^{-5}$		27.8	$6.67x10^{-5}$	37
Bliek et al. (1985)	0.2 ↑	0.9-1.2	$4.5x10^{-5}$ ↑		0	$4.6x10^{-1}$	$1.65x10^{4}$
Hajaligol et al. (1987)	0.4	1.3	$6x10^{-4}$		0	$4.2x10^{-4}$	533
Gavalas (1982)	?	1.0	10^{-3}		30	0.04	1.7
Devanathan and Saxena (1985)			$5.5x10^{-4}$	$4x10^{-4}$		$4.2x10^{-4}$	0.4

simplified case is considered where the particle is assumed to be dropped into a stagnant gas at an elevated temperature where radiation and convective heat transfer can be neglected. The characteristic time for internal conduction heat transfer is given as follows:

$$t_{c,i} = \frac{\rho_p C_p d_p^2}{20 k_p} \tag{II.E-1}$$

where ρ_p is the density, C_p the heat capacity, d_p the diameter, and k_p the thermal conductivity of the particle. The characteristic time for external gas phase conduction is:

$$t_{c,e} = \frac{\rho_p C_p d_p^2}{6 Nu\, k_g} \tag{II.E-2}$$

The definitions are the same as for Eq. II.E-1 except that k_g is the gas thermal conductivity and Nu is the Nusselt number for heat transfer which equals 2 for a spherical particle in an infinite stagnant medium.

The reciprocal of the characteristic time is, by definition, the rate constant for a first order process. This can be compared to the first order rate constant for pyrolysis mass loss which we have determined based on data for a number of coals. The results of these calculations are shown in Fig. II.E-4. This plot indicates three distinct regions of behavior. At low temperatures (< 600°C), $k_{chem} << k_{hext}$, k_{hint} and pyrolysis of the particle occurs isothermally at the maximum temperature of the gas without any internal temperature gradient. As the gas temperature increases above 600°C, but is lower than 1000°C, the particle pyrolyzes while heating to the final temperature but has a relatively small internal temperature gradient. At temperatures near 1000°C, there is not adequate time to collapse the internal temperature gradients before significant pyrolysis can occur.

Of course, these calculations can be done for many different conditions to include variations in particle size, external pressure, and the addition of other modes of heat transfer, such as radiation. The variation with temperature of the particle and gas thermal properties has been included. A computer program is being developed so that these calculations can be easily done for a specified set of conditions. This will allow an assessment of conditions where an internal heat transfer model will be required.

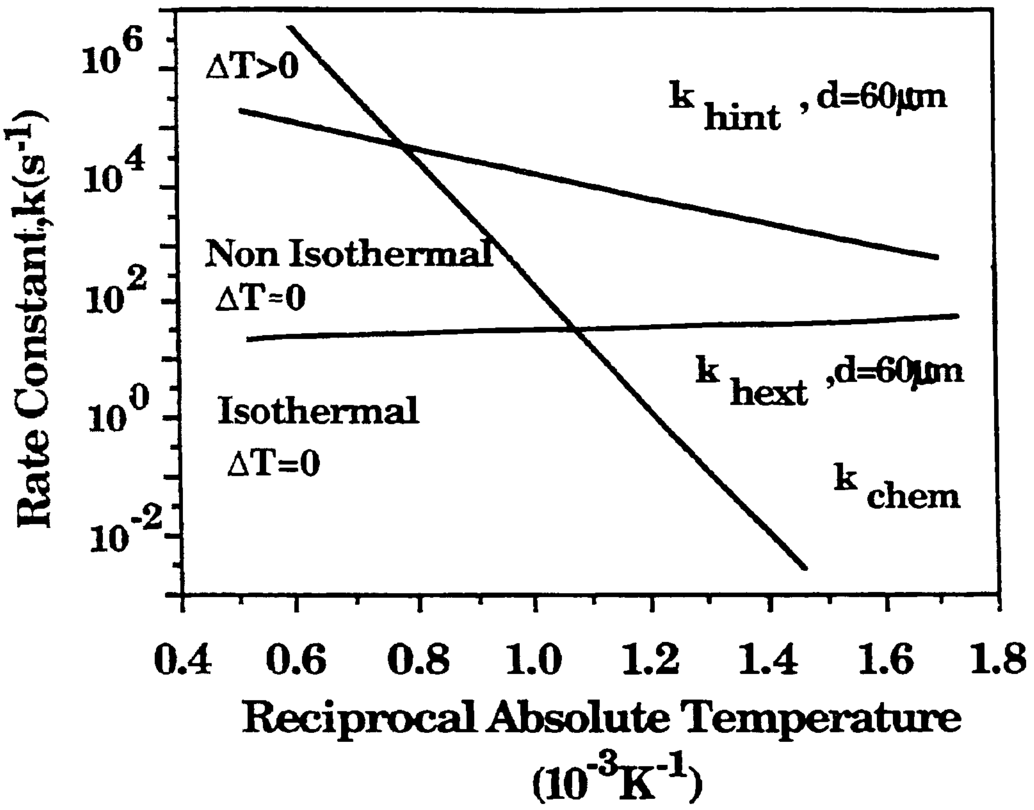

Figure II.E-4. Comparison of Chemical Kinetic Rate for Pyrolysis Mass Loss with Reciprocal Characteristic Times for External (k_{hext}) and Internal (k_{hint}) Heat Transfer.

Mass Transfer Calculations - The analogous calculations have been done for mass transfer (in the case of a bituminous coal), as shown in Fig. II.E-5. The situation is more complex because of the molecular weight dependence of the transport rates and the fact that the values of the species liquid phase and gas phase diffusivities are not well known. The calculation of the characteristic times requires the assumption of a model for internal and external mass transport. Generally, it is assumed that there are no mass transport limitations for light gas species (< 100 mw) for particles in the pulverized fuel size range (< 200 mesh). Consequently, the problem becomes one of defining the transport of the tar species.

As discussed in Section II.A, we have recently had success in describing tar transport with a simple model which assumes that tars are carried out of a particle at their equilibrium vapor pressure in the light devolatilization products (Solomon et al., 1987). The equations for tar transport (Eqs. II.A-1 to II.A-3) are discussed in Section II.A.

Because the assumed internal mass transport model depends to a large extent on heating rate, the calculations were done for high (20,000 K/s) and low (0.5 K/s) heating rates. In the former case, the pyrolysis chemical rate would reach a maximum at 948 K, while in the latter case it would maximize at 748 K. The internal and external mass transport rates were calculated for two molecular weights (314 and 1042) at these temperatures and plotted in Fig. II.E-5.

The calculations indicate that species close to 1000 in molecular weight are subject to significant internal and external transport limitations at all conditions of practical interest. Species which are close to 300 in molecular weight are limited by internal mass transport at low temperature (low heating rate) due to the low generation rate of the light species. At high temperature (high heating rates) the transport of 300 mw species is limited by the relatively slow vaporization rate from the surface.

As in the case of heat transfer, a program is being developed to make routine evaluation of mass transport rates for an arbitrary set of conditions.

Plans

Develop programs for routine calculations of boundary regions for internal and external heat and mass transfer. Summarize assessment of large particles heat/mass transport models. Consider how the AFR large particle model will interface with

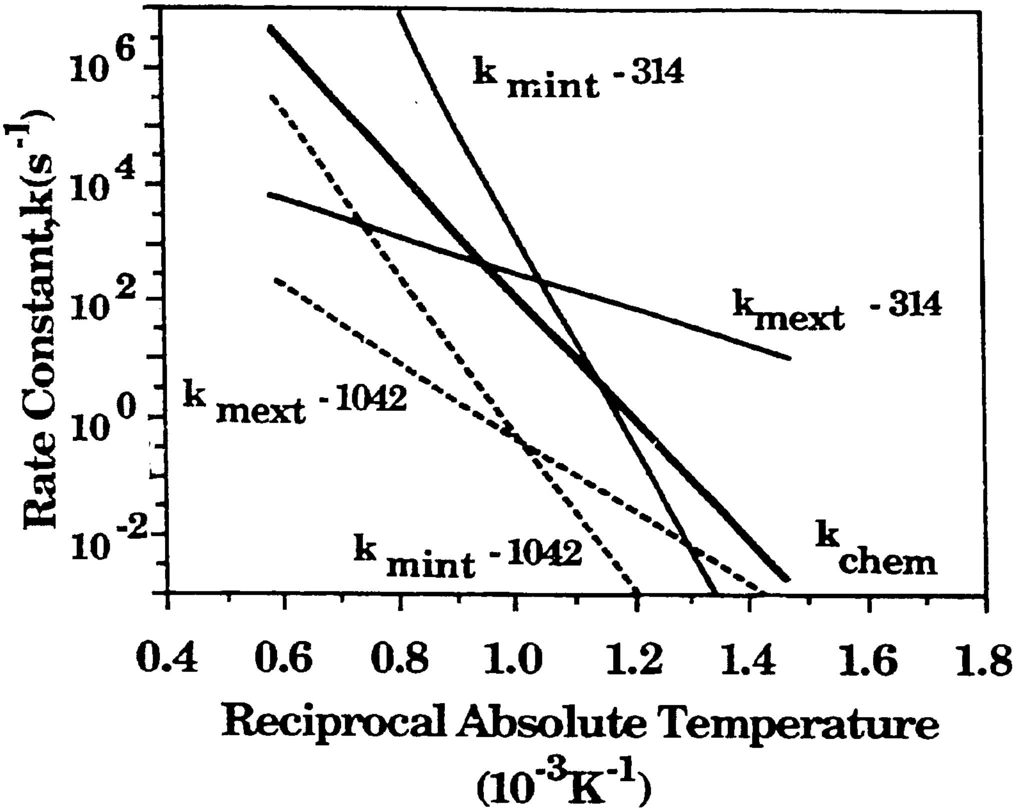

Figure II.E-5. Comparison of Chemical Kinetic Rate for Pyrolysis Mass Loss with Reciprocal Characteristic Times for External (k_{mext}) and Internal (k_{mint}) Mass Transfer. The Calculations were done for a 60 micron Bituminous Coal Particle.

the BYU fixed-bed model. Finish design and begin construction of fixed-bed pyrolysis reactor. Develop experimental plan.

II.F. SUBTASK 2.f. - LARGE CHAR PARTICLE OXIDATION AT HIGH PRESSURES

Senior Investigator - Angus U. Blackham
Combustion Laboratory
Brigham Young University
Provo, Utah 84602
(801) 378-2355

Objective

Provide data for the reaction rates of large char particles of interest to fixed-bed coal gasification systems operating at pressure.

Accomplishments

No work planned.

Plans

No work planned.

II.G. SUBTASK 2.g. -- SO_x/NO_x SUBMODEL DEVELOPMENT

Senior Investigators: L. Douglas Smoot and B. Scott Brewster

Brigham Young University
Provo, Utah 84602
(801) 378-4326 and (801) 378-6240

Objectives

The objectives of this subtask are 1) to extend an existing pollutant submodel in PCGC-2 for predicting NO_x formation and destruction to include thermal NO, 2) to extend the submodel to include SO_x reactions and SO_x-sorbent reactions (effects of SO_3 nonequilibrium in the gas phase will be considered), and 3) to consider the effects of fuel-rich conditions and high-pressure on sulfur and nitrogen chemistry in pulverized-fuel systems.

Accomplishments

The components of this subtask are 1) extension of an existing pollutant submodel to high pressure and fuel-rich conditions (including thermal NO formation), 2) modification of the current comprehensive code to include sorbent particle injection and reactions (including sulfur capture), and 3) extension of the pollutant submodel to include SO_x formation. Significant progress has been made during the first year on the first component. Work relating to the second component is ongoing at the University of Utah and will be used as a basis for Component 2 of this subtask. First-year progress is described below for each subtask component. During the firt year, financial support for this subtask was also obtained from an independent contract (Smith and Smoot, 1987). In subsequent years, all support is to come from this study.

Component 1 -- NO_x at High-Pressure/Fuel-Rich Conditions

The goal of this subtask is to extend the current pollutant submodel in the comprehensive code to be applicable to high-pressure, fuel-rich conditions such as are common in gasification processes. An important part of this extension is the inclusion of thermal NO formation which may be significant at the higher temperatures typical of gasification in oxygen.

The current model for NO formation and decay is illustrated in Figure II.G-1. Only fuel NO is considered. Nitrogen is assumed to evolve from the coal at a rate which is proportional to the rate of total weight loss and to instantaneously convert to HCN in the gas phase. The formation of NO occurs when HCN reacts with O_2. Homogeneous destruction of NO occurs when HCN reacts with NO, and heterogeneous destruction occurs when NO reacts with char (Smith et al., 1987).

<u>Thermal NO</u> -- Kinetic rate equations for thermal NO formation in both fuel-lean and fuel-rich systems were developed from the literature (Zeldovich, 1947; Baulch, et al., 1969; Sawyer, 1981; and Pohl and Dusatko, 1987). In fuel-lean systems, the following rate expression applies:

$$\frac{\partial X_{NO}}{\partial t} = \frac{9.91 \times 10^{15}\ \mathrm{K \cdot sec^{-1}}}{T} \exp\left(\frac{-68{,}500}{T}\right) X_{N_2} X_{O_2}^{\frac{1}{2}} P^{\frac{1}{2}} \qquad \text{(II.G-1)}$$

Eq. (II.G-1) is based on the well-accepted Zeldovich mechanism and assumes oxygen radicals in equilibrium concentration. For fuel-rich conditions, the measured rates are often much greater than predicted by Eq. (II.G-1). Allowing for oxygen radicals in excess of equilibrium (Sarofim and Pohl, 1973), the following expression results:

$$\frac{\partial X_{NO}}{\partial t} = \frac{4.09 \times 10^{11}\ \mathrm{K \cdot sec^{-1}}}{T} \exp\left(\frac{-34{,}900}{T}\right) X_{N_2} X_{O_2} X_{CO} X_{CO_2}^{-1} \qquad \text{(II.G-2)}$$

Under highly fuel-rich circumstances, the additional elementary reaction

$$N\cdot + OH \rightarrow NO + H\cdot$$

must be added to the Zeldovich mechanism, resulting in the following expression (Engleman et al., 1973):

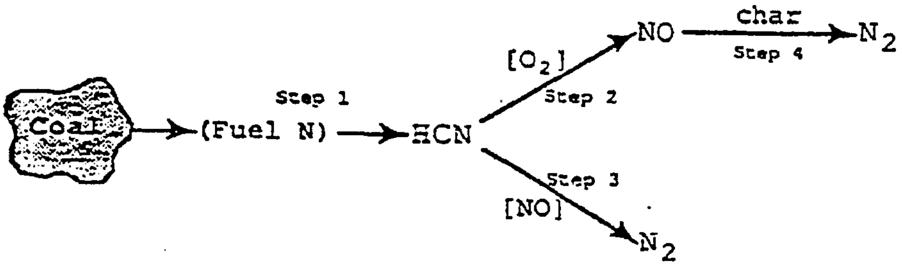

Figure II.G-1 Submodel mechanism for the formation and destruction of fuel NO during pulverized coal combustion.

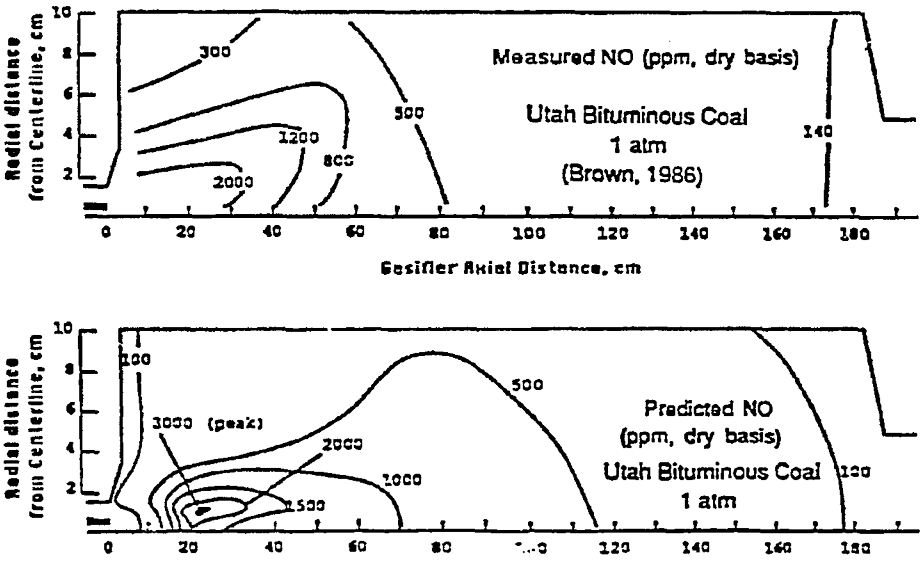

Figure II.G-2 Comparison of measured and predicted NO concentrations during atmospheric gasification of bituminous coal.

$$\frac{\partial Y}{\partial t} = \frac{M}{2}\left(\frac{1 - Y^2}{1 + CY}\right) \qquad \text{(II.G-3)}$$

where

$$Y = \frac{[NO]}{[NO]_{eq}} \qquad \text{(II.G-4)}$$

$$M = \frac{5.4 \times 10^{15}\ \mathrm{K \cdot sec}^{-1}}{T} \exp\left(\frac{-34{,}900}{T}\right) X_{N_2}^{\frac{1}{2}} P^{\frac{1}{2}} \qquad \text{(II.G-5)}$$

and

$$C = \frac{k_{-2} K_{NO} [N_2]^{\frac{1}{2}}}{k_3 [O_2]_{eq}^{\frac{1}{2}} \left[\frac{1 + k_4 [OH]_{eq}}{k_3 [O_2]_{eq}}\right]} \qquad \text{(II.G-6)}$$

Several researchers have attempted to predict thermal NO in turbulent gas flames (Bowman, 1973; Kent and Bilger, 1977; Peters and Donnerhack, 1981; Sadakata et al., 1981; and Drake et al., 1984), but the effects of turbulence-chemistry interactions have not been included except by Drake. Turbulence interactions are accounted for by convolving the instantaneous reaction rates over the probability density functions of the mixture fractions. By this method, time-mean reaction rates are obtained and used to solve the continuity equation for NO. With the addition of thermal NO into the model, a system of equations must be solved for each iteration. This requires that some major changes to the current NO submodel be made.

<u>Evaluation at Fuel-Rich and High Pressure Conditions</u> -- The application of the existing submodel to fuel-rich conditions and high pressure was evaluated by comparing predicted pollutant concentrations with experimental data for atmospheric gasification, high-pressure gasification, and air-staged combustion of bituminous coal and lignite. Reasonably good

agreement was obtained for the high-rank coals, but further extension of the model may be necessary for lignite.

Reactor maps of measured and predicted NO concentration for Utah bituminous coal at atmospheric and elevated pressure (5 atm) are shown in Figures II.G-2 and 3, respectively. Experimental data were taken from Brown (1986) and Nichols et al. (1987), respectively. As shown, the the maximum NO concentration is approximately 3000 ppm in both cases, and the peak occurs slightly earlier at elevated pressure. Both the magnitude and the location of the peak are predicted accurately by the model, including the slight shift in location. The exit NO concentration is lower for elevated pressure. Assuming equal peak concentrations, the lower exit value is due to an increased rate of decay and to a lesser extent, increased residence time. The increased rate of decay is due to the increased concentration of the reacting gas species. The increased residence time is due principally to the lower velocity for a fixed feed rate (Nichols et al., 1987). A similar comparison between predicted and measured NO concentration for an Illinois bituminous coal at atmospheric pressure (not shown) also gave reasonable agreement.

Results for the lignite are shown in Figure II.G-4. The predicted values are similar to the high rank coals while the measured values are significantly different. The measured NO concentration peak for lignite is much lower in magnitude and located farther downstream from the inlet. Major species and flame structure (not shown) were predicted reasonably well. One reason for the discrepancy between measured and predicted NO concentration for lignite results from the assumption that nitrogen is evolved at a rate proportional to the total coal weight loss and is instantaneously converted to HCN. The evolution of nitrogen is known to be delayed during the early stages of burnout, especially for lignites. Delayed evolution of nitrogen in gasification would result in less NO being formed because less of the nitrogen would be evolved in the presence of oxygen. In addition, Freihaut et al. (1987) have observed that lignites produce larger quantities of NH_3 during gasification than do high-rank coals. Indeed, in the studies referenced in Figures II.G-2,3, and 4, measured NH_3 concentration was 200-300 percent higher for lignite than for

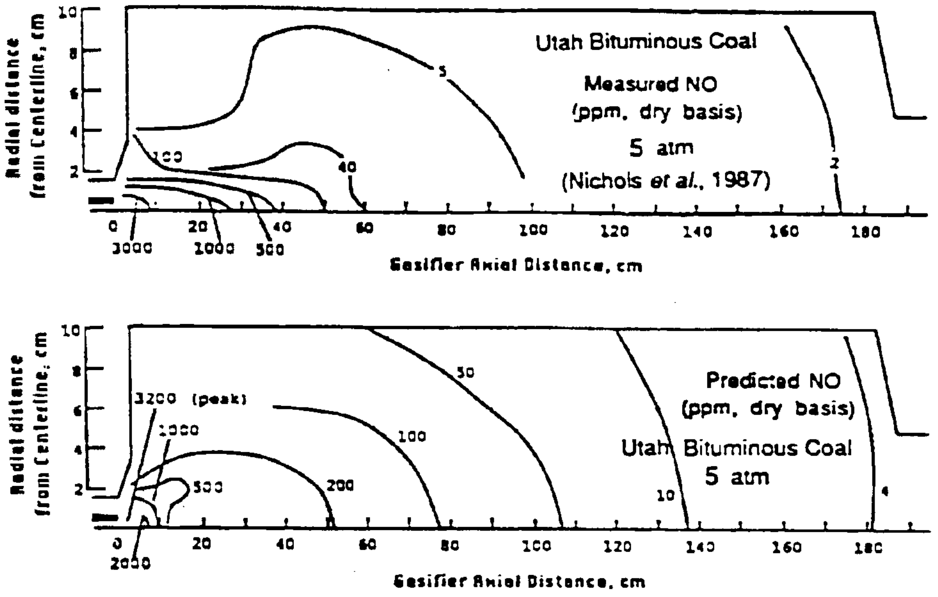

Figure II.G-3 Comparison of measured and predicted NO concentrations gasification of bituminous coal at elevated pressure.

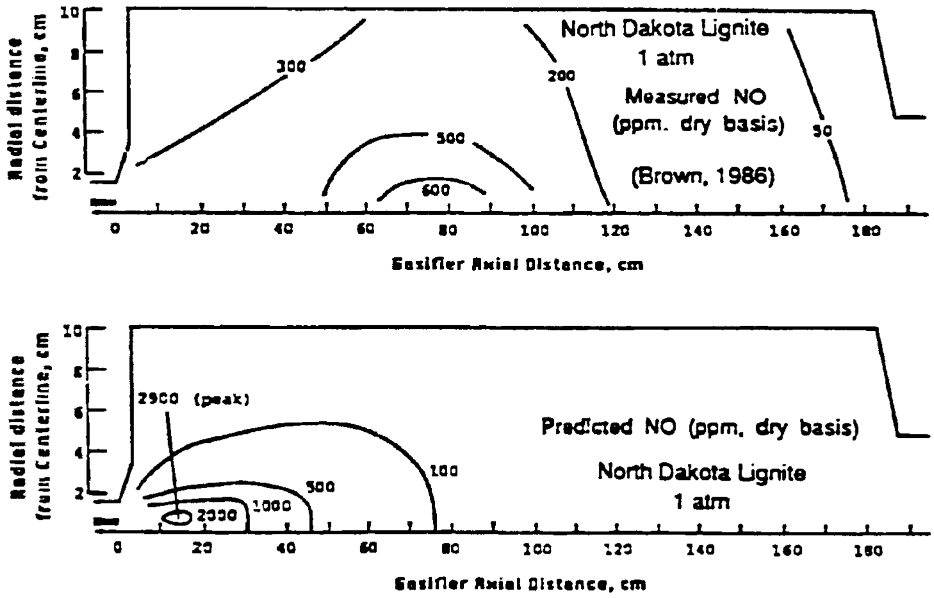

Figure II.G-4 Comparison of measured and predicted NO concentrations during atmospheric gasification of lignite.

the bituminous coal. Increased NH_3 concentration results in increased rate of NO decay (Kramlich, 1987). Thus, the observed slow buildup of NO concentration may be due to the relatively high concentration of fuel-rich nitrogen species and subsequent reduction of early NO. For such significantly higher concentrations of NH_3 and HCN (and presumably other fuel-rich nitrogen species), the rate constants for the NO model may not be appropriate.

Model performance for fuel-rich conditions was further investigated by simulating first-stage air/fuel ratios of 1.20, 0.95 and 0.80 of an air-staged combustor. Predictions and measurements are shown in Figures II.G-5, 6, and 7 for radially-averaged CO_2, O_2 and NO concentrations and for temperature. The temperature data, which are consistently 200-400 degrees K lower than the predicted temperature, are uncorrected for convective and radiative heat losses. The heat loss correction would raise the measured data and could easily account for the discrepancy. The major species, CO_2 and O_2, are predicted accurately in all cases.

For the fuel-lean case (Figure II.G-5), a high peak NO concentration is predicted initially but the profile rapidly decays to approximately 8 percent above the experimental profile. A similar trend is predicted for the S.R. = 0.95 case (Figure II.G-6) except that the NO decays to a level 10-15 percent below the measured data. The predicted NO concentration also follows this trend for the S.R. = 0.80 case (Figure II.G-7) but is consistently lower by 15 to 30 percent along the entire profile. The discrepancies between the measured and predicted NO concentrations in the early region of the reactor may be due to non-isokinetic sampling. The reactor was designed to establish one-dimensional flow (Wendt, et al., 1978). However, it is likely that radial gradients existed in the vicinity of the burner. The model predictions showed steep radial gradients in the early section of the reactor to the extent that when predicted NO near the wall was compared with the measurements in Figure II.G-5, the profile matched the experimental data throughout the entire reactor, including the early reactor region. Another explanation for the discrepancy in NO concentration in the early region of the reactor could be the delayed nitrogen evolution compared to that currently assumed. Wendt (1980) found

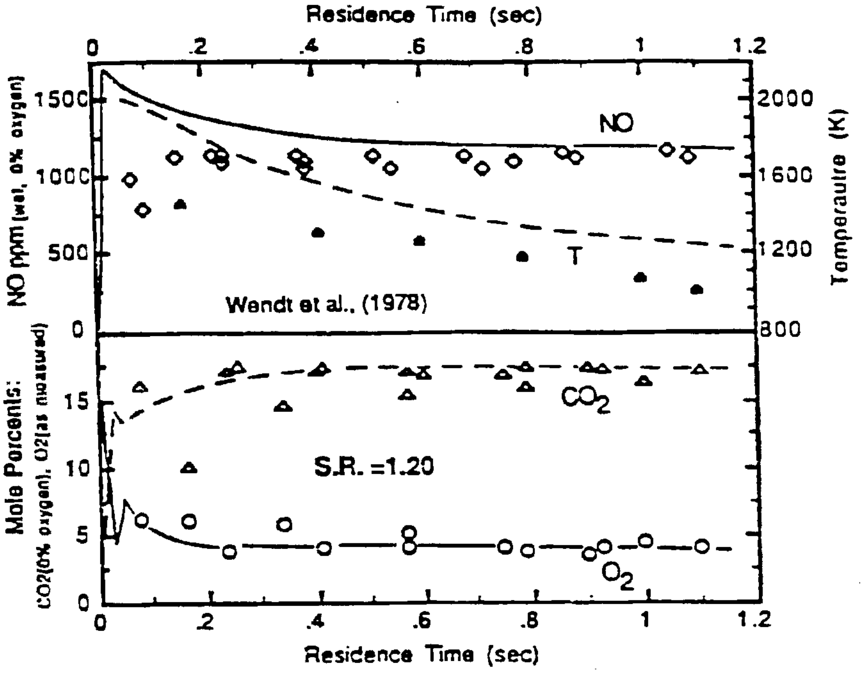

Figure II.G-5 Comparison of measured and predicted data for fuel-lean combustion of Kentucky bituminous coal.

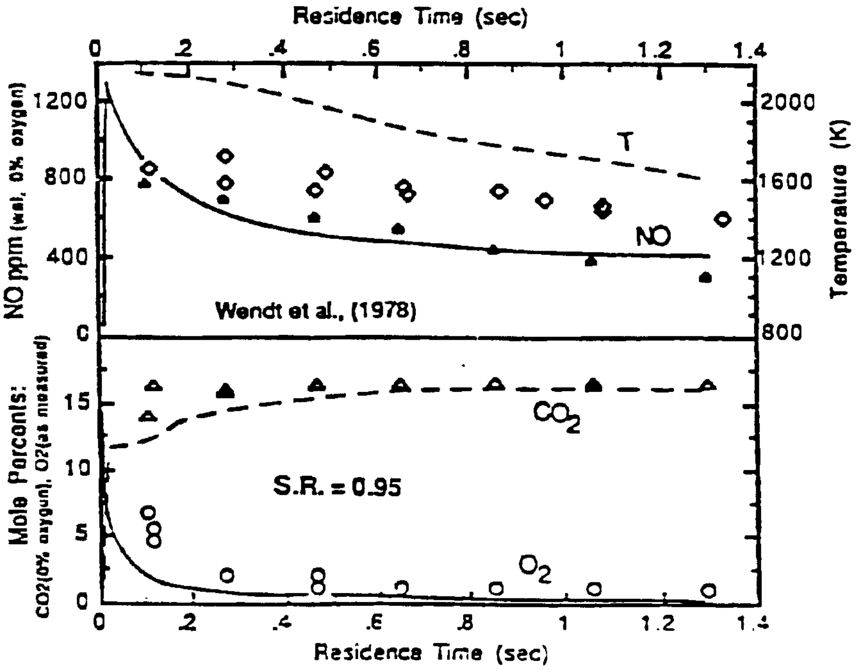

Figure II.G-6 Comparison of measuredand predicted data for slightly fuel-rich combustion of Kentucky bituminous coal.

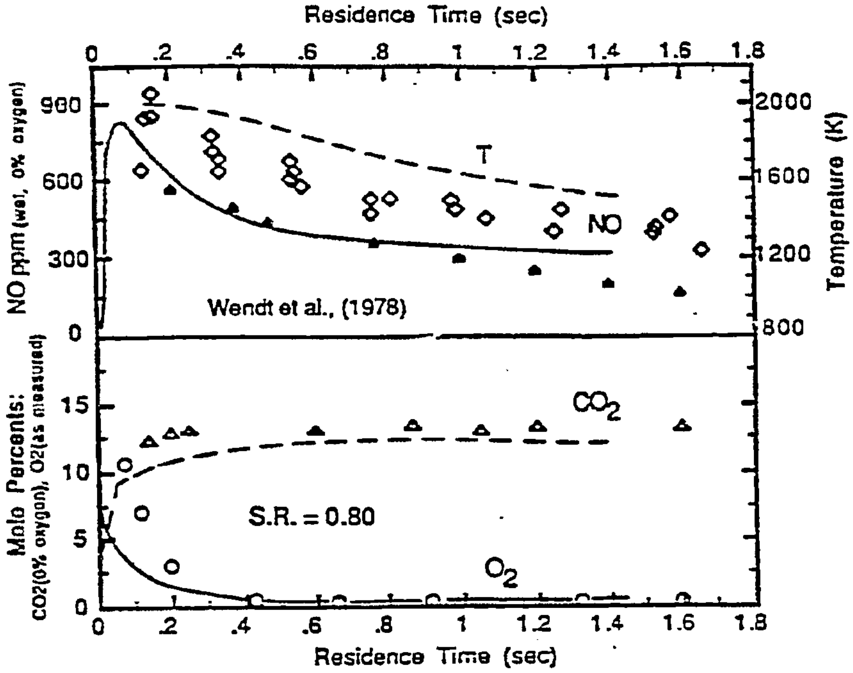

Figure II.G-7 Comparison of measured and predicted data for fuel-rich combustion of Kentucky bituminous coal.

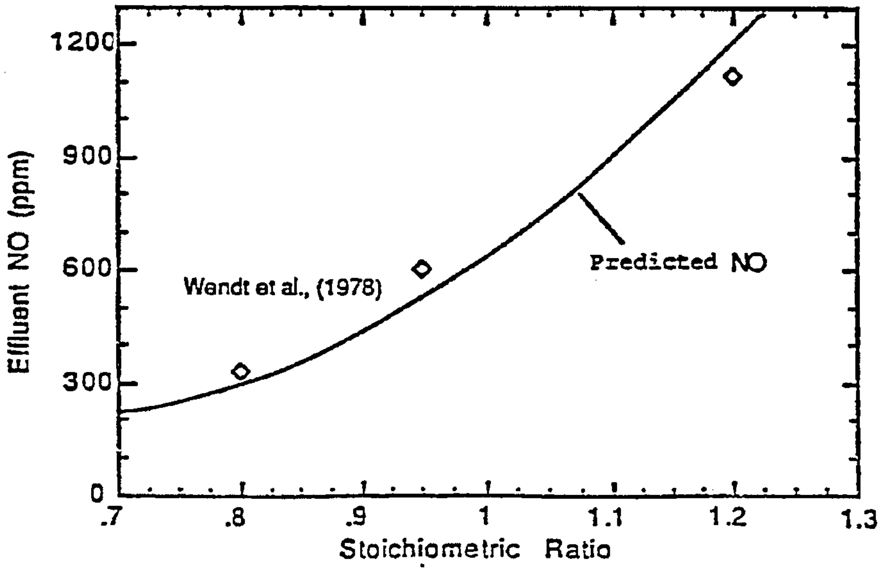

Figure II.G-8 Comparison of measured and predicted effluent NO concentrations for various of reactor stoichiometric ratios.

that at low temperature, the early volatiles are nitrogen-free. If the actual rate of nitrogen release is lower than the total coal mass loss, then the model could potentially overpredict the formation of NO in the near-burner region. The issue of predicting the rate of nitrogen release correctly would be aided by incorporation of a more detailed devolatilization model such as is being accomplished under Subtask 3a. Correctly predicting the rate of nitrogen evolution will likely improve the near-burner prediction of fuel-NO formation.

Figure II.G-8 illustrates the agreement that was achieved by the NO model for effluent NO concentrations over the range of stoichiometric ratios shown. At all S.R. values, the model closely predicts the measured values. Experimentally, it was also determined that thermal NO was negligible for this system from tests made with Ar substituted for N_2 in the combustion air (Wendt, et al., 1978).

Fuel NO is more dependent on temperature in fuel-rich environments than in fuel-lean. NO decay by char/NO and fuel-rich species interactions is accelerated by temperature (Song et al., 1981; Song and Bartok, 1982). The model predictions were consistent with this trend for the gasification cases and fuel-rich, primary zone of the staged combustion cases. By varying the reactor heat loss and thus the temperature profile throughout the reactor, the effluent NO concentration was altered by almost two orders of magnitude as shown in Table II.G-1 for one set of gasifier simulations. As heat loss was increased and temperature decreased, the effluent NO concentration increased, even though the peak NO concentration decreased. Consequently, accurate prediction of the reactor temperature is imperative for the NO model predictions, particularly in fuel-rich regions.

Table II.G-1

EFFECT OF TEMPERATURE ON NO DECLINE FOR FUEL-RICH GASIFICATION OF COAL AT CONSTANT FEED RATE

Heat Loss Factor	Peak Temperature (K)	Effluent Temperature(K)	Peak NO Conc. (ppm)	Effluent NO Conc. (ppm)
0.00	3150	2130	3450	0.01*
0.30	2740	1780	3400	0.1
0.45	2500	1615	3000	24

* Computer round-off error possible

Predictions were examined to determine the relative difference between homogeneous and heterogeneous NO reduction. In most fuel- rich locations, where concentrations of HCN were appreciable, the heterogeneous decay was found to be insignificant compared to the magnitude of homogeneous NO decay. This result is consistent with the experimental observation (Dannecker and Wendt, 1984) that gas-phase destruction of NO is the dominant NO reduction path in fuel-rich coal combustion. Homogeneous decay was far more significant the gasifier predictions because of the high concentration of fuel-rich species. However, for the combustion cases, homogeneous decay was only initially more significant but became relatively less important as the fuel-rich species were consumed. Thus, in the aft section of the combustor, heterogeneous NO decay also became important. These results imply that the NO model adequately describes the governing NO decay process for these cases.

Component 2 -- Sorbent Particle Chemistry

This subtask component is aimed at modifying the comprehensive code to include downstream injection of sorbent particles and their subsequent reactions with the gas phase. The work will be based on current work at the University of Utah, where a sorbent chemistry submodel is being developed for fuel-lean conditions. This subtask component has not yet been initiated.

Component 3 -- SO_x Formation

This subtask component will model the gas-phase reactions that generate the sulfur species for input to the sorbent capture model developed under Component 2 of this subtask. A literature search of work related to measurement and prediction of SO_x chemistry in combustion flames has been initiated.

Plans

Efforts will continue during the next quarter to extend the current NO submodel to be applicable to fuel-rich systems at high pressure. Investigation will continue into the necessary modifications to adequately predict NO concentration for lignite gasification. Code modifications will also be continued for thermal NO formation. In addition, consideration of revising the current fuel-NO mechanism for low rank coals will be made after investigating the development of a simplified global mechanism for the formation of fuel-NO in coal flames (Wendt, 1987). A literature search of sulfur chemistry in combustion flames will continue. Coordination will also be made with the University of Utah to facilitate the transfer of information on the development of their sorbent reaction model.

II.H. SUBTASK 2.h. -- SO_x/NO_x SUBMODEL EVALUATION

Senior Investigator -- Paul O. Hedman

Brigham Young University
Provo, UT 84602
(801) 378-6238

Objectives

The objectives of this subtask are 1) to obtain detailed mixing rate and turbulence measurements for radial crossjet injection of sorbent particles in a cold flow facility designed to replicate the geometry of a 2-dimensional, axisymmetric entrained flow coal gasifier, 2) to obtain concentration profile data for sulfur and nitrogen pollutant species from laboratory-scale, coal reaction tests at atmospheric and elevated pressure with and without sorbents, and 3) to investigate the effect of pressure on the effectiveness of sorbent injection in capturing sulfur pollutants.

Accomplishments

This subtask is being carried out under three subtask components: 1) A cold-flow investigation of sorbent mixing fluid mechanics, 2) modifications of the laboratory-scale reactor to accommodate sorbent particle injection, and 2) space-resolved sulfur and nitrogen pollutant measurements in the laboratory-scale reactor.

Component 1 -- Sorbent Mixing Fluid Mechanics

During the first year, a literature review of laser doppler anemometry (LDA), mixing in confined, turbulent jets, and isothermal modeling of fluid flows in a nonreactive system was conducted. Additionally, Robert Hendricks (Environmental Protection Agency) and David Pershing (University of Utah) provided engineering design and performance information on the Limestone Injection in Multistage Burners (LIMB) program (Categen, et al., 1987). Previous investigators in the BYU Combustion Laboratory (see Webb, 1982; Jones, 1984; and Lindsay, 1986) have used the BYU cold-flow facility to study the fluid mechanics of one of the BYU pulverized coal combustors and the BYU entrained-flow coal gasifier. Design modifications for including crossflow jets for sorbent injection in this cold flow facility were developed. Also, the existing flow chamber will be replaced with one constructed of transparent plastic to enable qualitative flow visualization.

The large diameter transparent tube for the reactor is currently on order. Initially, it was planned to convert the LDA system to forward-scatter mode in order to get an enhanced signal, but this was determined infeasible due to time and cost constraints. Smoke and/or 1-micron sorbent particles will be used for flow visualization and as seed material for the LDA measurements. The smoke will be generated by dripping mineral oil onto a heated plate that is contained in a flow channel that is feeding gas to the sorbent injection ports. The smoke generator is currently being fabricated. An existing Accrison, Inc. particle feeder will be used to feed the sorbent to the flow chamber.

The modified cold-flow facility will be geometrically and dynamically similar to the gasifier. The gasifier effluent will be simulated by the injection of an air flow at the inlet to the flow chamber. Micron-sized sorbent particles and/or smoke from the smoke generator will be injected about halfway downstream through crossflow jets. The axial location of sorbent injection will be variable in order to study the effect of different locations. Figure II.H-1 presents a schematic drawing of the transparent section of the flow facility. The duct is of modular construction so that the instrument collar shown can be located at various axial positions downstream of the sorbent injection ports.

The transparent walls will provide optical access to determine local velocity and turbulence profiles by LDA. Carbon dioxide will be injected with the sorbent, collected at each of the sample locations shown in Figure II.H-1 with gas sample probes, and analyzed with an on-line IR CO_2 analyzer. The measured concentration of CO_2 will be used to give a direct measurement of the rate of gas mixing in the duct. Several sample probes will be used, but only one probe will be in the flow at a time to minimize the flow disturbance. Probes are being located in the sample collection collar so

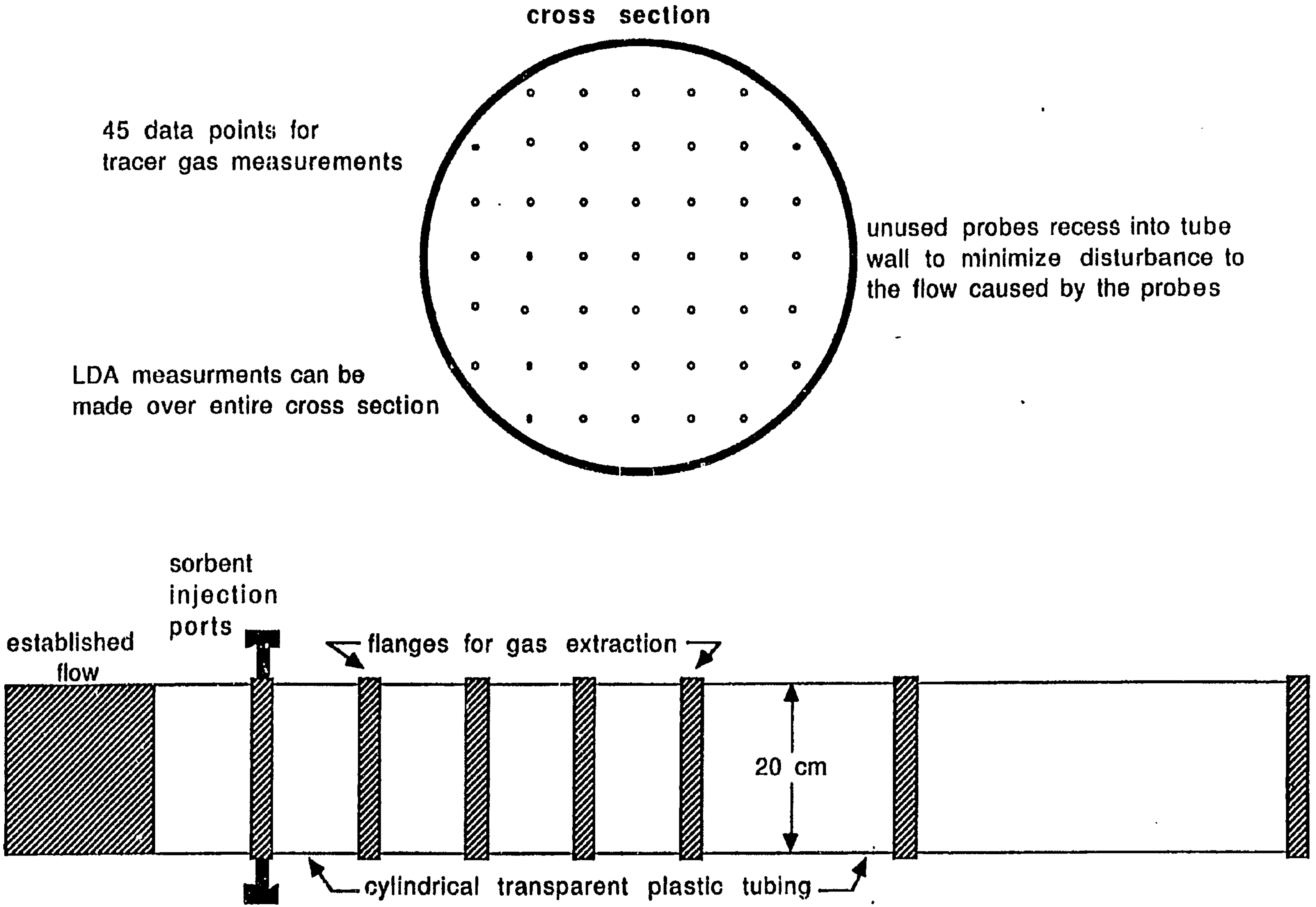

Figure II.H-1 Schematic of the Transparent Cold-Flow Sorbent Injection Flow Chamber that concentration data will be obtained from a two-dimensional grid pattern, as indicated in Figure II.H-1.

Component 2 -- Laboratory-Scale Reactor Modifications

This subtask component is aimed at modifying the laboratory-scale reactor to accommodate sorbent particle injection. Previous research has shown (see Categen, 1987; and Kamotani,1974) that the two most important criteria in the mixing of crossflow jets are the diameter and momentum flux ratios of the jet to the main flow. The effect of both criteria will be studied in these experiments. The lower limit of each ratio will be determined by the amount of sorbent which can be entrained in a given amount of gas while maintaining an adequate sorbent sulfur ratio, and the upper limit will be determined by the amount of gas and sorbent flow which would overly dilute the gasifier effluent. Researchers have varied the sorbent-to-sulfur ratio between 1.0 and 4.0 (Lindgren and Pershing, 1987; Categen et. al., 1987), and it is planned that sorbent-to-sulfur ratios representing this range will be used in these experiments.

Component 3 -- Space-Resolved Sulfur and Nitrogen Pollutant Measurements

This subtask component is aimed at making detailed measurements of sulfur and nitrogen pollutants and char in the laboratory-scale reactor. Work on this subtask will follow the completion of Component 2.

Plans

Modifications to the cold flow facility will be completed early in the next year of the study. Initial tests will be performed to check out and calibrate facility operation including operation of the smoke generator, the LDA, and the CO_2 gas collection and analysis systems. Once the facility has been demonstrated to work properly, mixing tests of the simulated gasifier flows with sorbent injection will begin.